5-8-2023

Measuring Diffusion Through Carbon Nanotube Arrays with Fluorescent Spectroscopy

Michael Machold
mdm7910@rit.edu

ROCHESTER INSTITUTE OF TECHNOLOGY

Measuring Diffusion Through Carbon Nanotube Arrays with Fluorescent Spectroscopy

by

Michael Machold

A Thesis Submitted in Partial Fulfillment of the Requirements for the Degree of Master of Science in Mechanical Engineering

Department of Mechanical Engineering
Kate Gleason College of Engineering

Rochester Institute of Technology
Rochester, NY
May 8, 2023

Committee Approval

Dr. Michael G. Schrlau, Associate Professor

Thesis Advisor, Department of Mechanical Engineering

Dr. Michael Schertzer, Associate Professor

Committee Member, Department of Mechanical Engineering

Dr. Patricia Taboada-Serrano, Associate Professor

Committee Member, Department of Chemical Engineering

Dr. Sarilyn Ivancic, Graduate Director

Department Representative, Department of Mechanical Engineering

Abstract

Carbon nanotube (CNT) arrays are emerging as versatile nanostructures that can be used in many applications including gene transfection technology. To understand the transport of molecules through an array of CNTs, diffusion of molecules was studied experimentally and analytically. A procedure using fluorescent spectroscopy was developed to measure the concentration change of fluorescein salt in a two-reservoir system separated by a CNT array. Experiments were conducted to measure how changing the initial concentration gradient and reservoir volume size impacted the diffusivity of the system. For 2 mL reservoirs, diffusivities were measured between $2.56 * 10^{-11}\ \frac{m^2}{s}$ and $3.51 * 10^{-1}\ \ \frac{m^2}{s}$. Diffusivities were measured between $2.5 * 10^{-11}\ \frac{m^2}{s}$ and $7.91 * 10^{-11}\ \frac{m^2}{s}$ for reservoirs of 5 mL volume. Changing the starting concentration in the range of 4.29 to 100.1 μM did not significantly affect the value of diffusivity for a given reservoir size. Using the Stokes-Einstein equation and Fick's laws of diffusion, an analytical model was developed to estimate the diffusivity of fluorescein salt to be $5.17 * 10^{-11}\ \frac{m^2}{s}$. The results of experimentation and modeling provide a method to predict the time needed for concentrations of molecules to diffuse through the CNT array. The use of a fluorescent spectroscopy device can be applied to study diffusion of other molecules and properties of carbon nanotubes.

Acknowledgments

Thank you to RIT for providing the Construct and other materials necessary for the development of the experimental devices.

Thank you to Dr. Michael Schrlau for the mentorship and guidance throughout the last two years of graduate research. Our weekly conversations and your insight into academia have guided me through this project as well as in graduate school.

Thank you to Dr. Patricia Taboada-Serrano, your expertise in chemistry was instrumental in overcoming many challenges throughout this research. It is always a pleasure to attend your office hours and share with you my latest results.

Thank you, Dr. Michael Schertzer, for guidance in understanding Micro-Fluidics and serving on my committee despite the short notice.

Thank you to Dr. Ke Du for allowing access to the spectrofluorometer used in initial experimentation. Additional thanks to Mengdi Bao, Grant Korensky, and Chad Tenpas for insight into the equipment and software used to operate the device.

Thank you to Mr. Rick Wurzer for fabricating the polypropylene and aluminum reservoirs. Your artisanship produced robust devices that led to great results. Thank you to Mr. Mujtaba Siddiqui and other members of the NBIL for assistance with CNT array manufacturing.

Thank you to my mother, Mrs. Cynthia Machold, for inspiring me to follow my dreams and persevere through life with a smile on my face. Due to your sacrifices, I lead a fulfilling life.

Thank you, Ms. Kaylee Cappuccio, for helping me grow into the person I am today and always being my biggest supporter.

Contents

List of Figures

List of Tables

Nomenclature

CNT	=	Carbon Nanotubes
CVD	=	Chemical Vapor Deposition
NBIL	=	Nano-Bio Interface Laboratory
RIT	=	Rochester Institute of Technology
SWNT	=	Single-Walled Nanotube
MWNT	=	Multi-Walled Nanotube
MD	=	Molecular Dynamics
CFD	=	Computational Fluid Dynamics
Qdots	=	Quantum Dots
SEM	=	Scanning Electron Microscope
DI	=	De-ionized
PI	=	Propidium Iodide
AAO	=	Anodized Aluminum Oxide

1.0 Introduction

The emerging world of nanotechnology is a dynamic environment that offers a unique intersection of materials science, biology, and chemistry. As the academic understanding of chemistry develops, new methods of manufacturing and studying nano and microstructures have been produced. The utilization of nanostructures can be seen in many applications, such as chemical detection, fluid transport, and filtration.

The discovery and development of graphene specifically has led to a surge of technologies centered around this material. Carbon nanostructures have many beneficial chemical properties that when combined with the abundance of carbon, lead to many potential applications. Advancements in manufacturing processes have given way to carbon nanotubes (CNTs) ranging from 1 nm to 200+ nm in diameter. This versatility in size and chemical usage has been applied in many types of devices.

CNT arrays can be used as a platform technology for efficient transport of molecules into cells. The device incorporates arrays of carbon nanotubes embedded in a sacrificial template to create a surface of exposed CNT tips on which cells can be cultured. Initial research into this device has shown improved transfection efficiency with low cytotoxicity compared to standard transfection techniques [1].

The use of an array of CNTs for transfection of cells has created a need for understanding the passive transport of organic molecules, proteins, and DNA through the array. The elucidation of this cellular absorption unlocks the optimization of CNTs and would substantiate the use of nanostructures in drug delivery on a wider scale. Initial research into the transfection of molecules using this device have shown the cultured cells take up the molecules more efficiently when in contact with the CNT tips as compared to traditional gene transfection technology [1].

Currently, confirmation of transfection is conducted using fluorescence microscopy to visualize the presence of fluorescent molecules in cells that are cultured on top of the CNTs. As the molecules are allowed to diffuse and are taken up by the cells, the fluorescence of the cell increases. Current experiments cannot accurately measure the concentration of fluorescent particles in cells. However, by measuring the effective diffusivity of various molecules, the mechanism for cellular transfection can more clearly be understood.

In this thesis, a methodology for quantifying diffusion through CNT arrays was developed using fluorescent spectroscopy. It was hypothesized that the diffusivity of a molecule can be determined by placing two reservoirs of differing fluorescent molecule concentration on either side of a CNT array and monitoring changes in fluorescent intensity as a function of time. By correlating the fluorescent intensity of a solution to the concentration of that solution, the passive transport of a fluorescent molecule can be measured. Using Fick's laws of passive transport, the exponential time constant of the data can be used to calculate the diffusivity.

Parameters such as reservoir volume, active surface area for diffusion, and concentration gradient can be studied using this setup to understand the effect on passive transport. The two-reservoir setup allows for the investigation of CNT interaction with solution. Such an approach was aimed at answering the following research questions.

How can fluorescent spectroscopy be employed to measure diffusion through porous media?

1. What is the best device configuration to study the change in concentrations for two reservoirs separated by a porous membrane?
2. What method of sealing can be used to limit the flow of fluid to a desired area of the CNT array surface?

How can the measurements collected by a fluorescent spectrometer be correlated to the time of diffusion across a porous media?

1. What is the best way to mathematically model the rate of diffusion across a CNT array?
2. As the reservoir volume on either side of a CNT array increases, how does the diffusivity of the system change?
3. What are the benefits and limitations of fluorescent spectroscopy when compared to fluorescence microscopy for quantifying diffusion through CNT arrays?

An analytical model based on the Stokes-Einstein equation and modified Fick's Laws of diffusion was developed to compare theoretical estimations of diffusivity to experimental results. This model provides an easy way to estimate how diffusion changes in response to changing solution type and system dimensions. A diffusivity value of $5.71 * 10^{-11}\ \frac{m}{s^2}$ was estimated using the model.

The experimental procedure was used to measure diffusivities ranging from $2.50 * 10^{-11}\ \frac{m}{s^2}$ to $7.91 * 10^{-11}\ \frac{m}{s^2}$ for 2 mL and 5 mL reservoir volume. By decreasing the volume

from 5 mL to 2 mL the diffusivity of the system did not change, but the time to equilibrium was reduced. There was no apparent effect of changing the concentration gradient on the diffusivity. The results of the experimental procedure agree reasonably well with the analytical model developed.

Measuring rate of diffusion in CNT arrays is the first step in the process of characterizing molecule uptake in cells plated on the array surface. By quantifying the effectiveness and speed of transfection, future research can compare CNT arrays to other commonly used transfection technologies. By varying certain parameters such as CNT diameter, active surface area, and CNT length research into the properties of CNTs can be conducted. Further, the methodology developed can be used in applications outside of cellular transfection. CNT properties are interesting for applications such as desalination, cellular probes, and electrochemistry.

2.0 Background

The discovery of carbon nanotubes has led to their emergence as candidates for various technological developments. In this section, the discovery of carbon nanotubes and the many applications they have been used in are introduced. One major area of application has been biology. Biosensors and biocompatible nano-probes are a promising use case for graphene. Such applications led to the use of arrays of amorphous CNTs in drug delivery to cells. These devices use passive molecular transport, which unlike pressure driven flow, has not been well characterized in the literature. The history of graphene and the many uses of carbon nanotubes have informed the need to measure the diffusivity of biomolecules in a system with aligned carbon nanotubes.

2.1 Carbon Nanotubes

Carbon nanotubes were first characterized in 1991 by Sumio Iijima [2]. Iijima used an arc-discharge evaporation method to produce needle-like tubes made of sheets of graphitic carbon. Pictures of these structures were taken using Electron Microscopy, and analysis showed tubes made up of sheets of graphitic carbon arranged in helical fashion. These tubes were measured to have diameters ranging from few to tens of nanometers and had a length of up to 1 micrometer. These tubes were recognized as being constructed of hexagonally bonded carbon.

In a follow up publication Sumio Iijima focused on isolating single walled carbon nanotubes (SWCNT) for use in characterization [3]. Electron structure and mechanical strength proved to be measurements of interest. It was shown that single walled carbon nanotubes have a diameter of roughly 1 nanometer. When using carbon-arc synthesis, multi-walled CNTs grow on the carbon cathode whereas SWCNTs grow in the gas phase between the electrodes. Using electron diffraction, the characteristic hexagonal arrangements of the SWCNTs were observed.

Since the initial characterization of CNTs, three categories have emerged to describe the types of tubes as single walled, multi-walled, and amorphous. Carbon nanotubes are made up of either graphitic or amorphous carbon layers. SWCNTs are 1-2 nm diameter carbon tubes made with a single layer of fullerene structured carbon and MWCNTs have multiple layers of fullerene structured carbon with 2-23 nm diameter. Amorphous tubes do not have long range fullerene structure. Instead, these tubes share the structure of SWCNTs and MWCNTs in the short-range

and have no crystalline structure at long range. Amorphous tubes are made up of layers of non-crystalline carbon and tend to have relatively larger diameters (~40-200 nm).

Graphene has proven to be a versatile material with potential that has yet to be fully realized. Since the discovery of the two-dimensional sheets with a lattice structure of carbon atoms, efforts have been made to characterize the many useful properties of this material. Following the work of Iijima, carbon nanotubes and graphene are shown to have incredible chemical and physical properties that have started a revolution in nanotechnology. Two professors at Columbia University, Dr. Jeffery Kysar and Dr. Hone [4] measured graphene to be the strongest material characterized. In these experiments a monolayer of graphene was probed by nanoindentation in an atomic force microscope. By measuring the stress-strain response of the material, the tensile stiffness was found to be 340 newtons per meter and the compressive stiffness was 690 newtons per meter. These quantities give a young's modulus of 1 tera pascal. The hexagonal atomic layer is attributed to this outstanding material property. Currently, the manufacturing of 2D materials into macro structures is still an area of active development and great challenge. Much effort has been made in incorporating graphene into composite materials to exhibit added material strength to metals such as copper [4]. The properties of graphene at a macroscale would unlock many advancements in materials science, space travel, and medicine.

Apart from graphene sheets and carbon nanotubes, other form factors for this material have been shown to share mechanical properties. Dalton et al. [5] spun 100 m long composite fibers made from carbon nanotubes. Gel fibers made from SWCNTs and polyvinyl alcohol were used to form solid nanotube fibers with lengths on the order of tens of centimeters. These fibers were spun into a reel that was 100 meters in length. The material produced had a tensile strength of 1.8 gigapascals equal to the strength of spider silk. The fibers had a 60% composition of SWCNTs which yielded mechanical properties roughly 10 times less than that of isolated SWCNTs. In the paper, electronic textiles are cited as a use case due to the electrical conductance of carbon creating opportunities for fabrics connected to sensors. The ability to manufacture carbon nanotubes into larger structures is the first step in creating devices from this material.

In addition to the outstanding mechanical properties, graphene has useful thermal and electrical conductivity with uses in many electrical applications. Transistors made of aligned SWCNTs were shown to have a drive current of 120 μA/μm [6]. These transistors could be used

in applications such as thin film transistors and high-performance logic devices. SWCNT arrays were constructed using the Langmuir-Schaefer technique in which solutions of SWNT are arranged into aligned arrays to achieve high nanostructure densities. The aligned SWNTs are transferred onto a silica substrate for use as transistors. The high density of aligned nanotubes resulted in increased electrical conductance of the nanostructure. Such applications of graphene in electronics are promising but have immediate limitations due to handling of nanostructures.

The chemical composition of CNTs being of pure carbon leads to biocompatibility with cells and additional living organisms. CNTs are organic materials with the ability to interact with organic systems unlike current devices composed of metallic or inorganic materials. In a paper by Smart et al. the nanotoxicology and biocompatibility of CNTs is explored [7]. Biocompatibility is a property that allows for materials to interact with organisms without the side effect of toxicity detrimentally affecting the target. Designing devices with biocompatible materials would provide great benefit in the application of drug delivery, biosensors, and microbiology research. Many forms of carbon have shown low toxicity in devices such as heart valve protheses made of pyrolytic carbons. The interaction of CNTs with cells has shown promisingly low cytotoxicity. In larger biomedical devices, there is conflicting evidence on toxicity to larger organisms such as mice and humans. However, on the cellular level, the organic nature of CNTs makes them good candidates for biomaterials and devices.

Ultimately, the properties of graphene and CNTs lend themselves to replacing many materials that are standard in countless industries. The mechanical strength of graphene is useful in materials science, aerospace, and construction. Electrical conductance and biocompatibility are useful in medicine and energy applications where expensive, inorganic materials dominate.

2.2 Carbon Nanotube Synthesis

Synthesis of graphene and carbon nanotubes involves the controlled growth of crystalline carbon latices [2]. Tubes are produced by methods that include electric arc technique, laser ablation, carbon disproportionation, and chemical vapor deposition. Each method has different use cases with resulting chemical properties and physical structures. Early research into synthesis was focused on isolating single walled tubes as the presence of defects in multi walled tubes hampered the physical properties of graphene.

The technique used to create early tubes by Iijima was derived from similar techniques for creating graphene sheets. Carbon-arc synthesis consists of using 2 carbon electrodes in a methane-argon environment [2,3]. A small piece of iron was placed in a dimple on the carbon cathode. A DC current of 200 A and 20 V was passed between the two electrodes creating a high energy and carbon-rich environment. The iron melted to form an iron droplet and iron vapor that created iron carbide. The iron acted as a deposition center for the carbon nanotubes to grow from. The resulting soot contained the MWCNTs and SWCNTs amongst clumps of amorphous carbon. Acetone suspension was used to isolate CNTs for observation and remove unwanted soot. By manufacturing large amounts of single walled tubes, the true potential of these structures was elucidated. In this publication, the longest observed SWCNT was 700 nm, and the diameters were measured between 0.7 and 1.6 nm.

Electric arc technique has been used dating back to the discovery of graphene and carbon nanotubes [2]. The production of SWCNTs in mass was popularized by Journet using the electric-arc technique derived from the technique used by Iijima [8]. Single walled CNTs had not been produced with high yield up to that point. Electric arc had been used to make graphene sheets and MWCNTs. The electric arc was generated by two electrodes composed of graphite in the presence of a metal catalyst for the tubes to grow on. A current of 100 A and 30 V was employed to stimulate the growth of CNTs. The controlled parameters resulted in distinct areas of SWNTs in bundles that could be distinguished from the MWCNTs and amorphous carbon. The difficulty of generating SWCNTs compared to MWCNTs is attributed to the condensation of carbon resulting in bundles rather than singular tubes. A high SWCNT yield was obtained by altering the composition of the metal catalysts leading to high concentrations of SWCNTs.

An additional method of generating CNTs is laser vaporization of transition metal/graphite composite rods [9]. Like Journet, laser vaporization led to high yields of SWCNTs but cut down on the presence of amorphous carbon. In this method, carbon and a transition metal are vaporized with a laser. Direct vaporization as opposed to the arc method allows for control on growth. Multi walled carbon nanotubes were not observed in the resulting nanostructures created. In addition, the amount of amorphous carbon surrounding the tubes was reduced making the tubes “cleaner” or of higher quality. The high yield of SWCNTs is attributed to the condition and composition of metals. The formation of the fullerene structure is affected

by the size of the metal particle that the carbon grows on. By altering the metal catalyst composition, it was shown that the presence of two metals is essential for higher yield of single walled nanotubes.

CO disproportionation additionally expands on the high yield rate of single walled carbon nanotubes. Bronikowski et al. [10] produced SWNT of 97 mol% purity by decomposing $Fe(CO)_5$ in an atmosphere of CO. The decomposition results in clusters of iron on which the carbon nucleates into nanotubes. The scale of production was drastically improved by outputting CNTs at 450 mg/h. The resulting material is SWNT ropes amid carbon coated iron particles. There was minimal amorphous carbon present on the SWNTs produced. Control of iron cluster growth is cited as vital to the production of high concentration of SWCNTs.

2.3 Template-Based CVD of Carbon Nanostructures

Carbon nanostructures can be grown using sacrificial templates through chemical vapor deposition. Chemical vapor deposition (CVD) is a process of manufacturing CNTs by forming solid carbon structures from the thermal decompositions of a carbon-carrying gas. This process typically utilizes a sacrificial template to which the carbon nucleates onto. There are many types of CVD including thermally activated, plasma-enhanced, and fluidized-bed CVD [11]. The high temperature and carbon rich environment stimulate the growth of carbon. This method can produce SWCNT, MWCNT, and amorphous carbon tubes.

CVD has been used to generate MWCNTs of 3-10 nm on a silicon substrate and in the form of a CNT sponge [12]. The goal of Chen et al. was to measure the frictional properties of these CVD generated samples. The templates used resulted in samples with high static friction and desirable properties such as light weight and high compressibility. Sacrificial templates remove the need for complex nano assembly of CNTs as seen when using processes like arc discharge and laser ablation. The versatility in substrate design allows for the employment of CNTs in a variety of applications.

Template-based thermally activated CVD manufacturing offers dimensional control over length, diameter, and thickness [11]. By changing deposition time, temperature, and gas flow rate, dimensional control can be realized. Golshadi completed a parametric study to understand the growth of amorphous carbon tubes in sacrificial anodized alumina templates. SEM and TEM

were used to inspect the growth parameters and optimize the dimensions of tubes grown. Raman Spectroscopy was employed to investigate the carbon structure. The AAO membranes were purchased from Whatman (Cat. No. 6809-7023) with pore diameters of 200 nm. A tube furnace was used to flow a mixture of ethylene and helium gas at high temperature. From the study, guidelines on the values to choose for gas flow, temperature, and time were developed.

The NBIL has additionally explored alternative form factors for template-based CVD. Shapes such as multi-barrel, photonic crystal fiber, and diatom have all been produced [13]. Scheibel used silica-based templates to create high throughput manufacturing of amorphous carbon tube devices. Quartz capillaries were of primary interest as the resulting carbon nanotubes could be used to form nanopipettes. Such devices could be employed in electrochemical, fluid transport, and biology interfacing applications. Quartz was an ideal candidate due to the softening temperature that was far above the process temperature needed for CVD. Wet or dry etching was employed to expose the carbon tubes and selectively remove the silica templates. Exposing the tips provides clean cylindrical tubes with biocompatible material that can interface with organic environments. The long nanopipette templates were formed from drawing quartz capillaries. To deposit the carbon, argon was used to create an inert environment before deposition. Methane and argon mixture was introduced to begin growth in the quartz tubes. Hydrofluoric acid was employed to remove the quartz tips enclosing the CNT tips. The resulting structure has amorphous carbon tubes of roughly 45 nm in a bundle with a diameter of 350 nm.

Photonic crystal fiber templates provide templates of large diameter. The pore size of 1250 nm is significantly larger than the pore size of the quartz capillaries. By attaching the ends of the template to acrylic slides and etching away the silica, exposed tubes of wall thickness 95 nm were created. Diatoms are small organisms with silica support structures. Upon the death of this organism, the silica structure is left behind with cell walls of 2-2000 μm and pores on the order of 10 nm. After the CVD process was applied, CNTs embedded in silica and surrounded by carbon resulted. The variation in diatom species can be employed to create wide ranging microstructures of varying CNT size and hierarchical shape.

Due to significant use of CVD and the tube furnace, effort was directed toward the numerical modeling of the CVD process used by the NBIL. Such models informed the technique parameters used in growing carbon [14,15]. CFD simulations were developed to estimate the 2D

and 3D flow of carbon within the tube furnace used for CVD. Velocity and temperature of the carbon rich gas inside the tube furnace were developed and compared to experimental results collected from the system. Four numerical models of varying complexities were applied to numerical methods for a 3D model of flow. The studies were able to accommodate various tube furnace geometries that affect the Reynolds number of flow. The model could be used to predict the environment in any CVD system resulting in growth of carbon on templates.

Carbon vapor deposition is a versatile technique capable of producing SWCNTs, MWCNTs, and amorphous CNTs. Template based synthesis provides ordered growth of graphene without complex processing techniques seen in techniques such as arc discharge and laser ablation.

2.4 CNT Based Nanopipettes

Carbon nanotubes are an emerging technology with new devices being created. Such devices are applied in microbiology, electrochemistry, fluid dynamics, and more. In the NBIL, chemical detection probes and CNT array devices have specifically been developed.

The NBIL was founded on the practice of creating carbon-based devices that can interact with cells and other microenvironments. Schrlau et al. [16] created carbon nanotube-based pipettes to inject reagents into cells. By attaching these micropipettes to atomic force microscopes, the precise penetration of cell membranes can be carried out. The electrical resistance of these carbon pipes with wall thickness of 80 nm was shown to be 15 kΩ. The compressibility of graphene contrasts with the brittleness of glass nanostructures which easily shatter. After piercing the cell walls, the injection of fluorescent rhodamine was used to demonstrate drug transport using these probes. In additional studies, neurons have been shown to survive and fluoresce for many days following the injection of dye, leading to the lack of toxicity in carbon probes. The biocompatibility of CNTs allowed cell growth unlike other forms of injection with glass or metallic pipettes that have higher cytotoxicity. Conductivity of carbon allows for the measurement of environments on top of the injection of material.

The development of such pipettes was expanded upon by studies in the NBIL. Fabrication of theta carbon nanopipettes consists of two carbon pipes aligned in parallel with each other grown inside of quartz capillary tubes [17]. The formation of the quartz capillaries

was governed by the heat, filament, velocity, and pull force of the puller device. Arowosola conducted a study to determine the effects of varying these parameters on the dimensions of the capillary tips. Methane and argon were then used to grow graphene on the quartz templates. Using hydrofluoric acid, the tips of the carbon structures were exposed. The tapered geometry of the capillary tubes created ideal interactions with fluids to be injected using the nanopipettes. Fluorescent microscopy was used to observe the ejection of dextran from the tip for the theta carbon nanopipette.

CNTs have been used in many biosensors [18] based on MWCNTs and nanoparticles. Such sensors have detected dopamine, amino acids, lead, and cadmium. The mechanisms for such detection rely on graphene's electrical conductivity. The emergence of carbon-based electrodes has allowed for low-cost probes with desirable mechanical and chemical properties.

In the NBIL, a self-contained two electrode nano-sensor was developed that featured two carbon nanotubes encased in a quartz capillary [19]. Pipettes were drawn using carbon dioxide laser-based pulling and then used as CVD templates. Electrical connections to both carbon structures were accomplished by inserting tin-coated copper wire into the distal end of each. One of the CNT tips was coated in silver and chlorinated to form a pseudo-Ag/AgCl reference electrode. The coating of a singular tip was accomplished by applying a current to one tip during the coating process. The uncoated tip served as the working electrode for electrochemical experiments. SEM was used to confirm the proper formation and dimensions of the electrodes.

These carbon nanotubes acted as the electrodes needed to detect small concentrations of redox-active analytes. Para-aminophenol (PAP) in aqueous microenvironments was used in proof-of-concept experimentation. The sensor was able to detect concentrations of PAP in bulk and microenvironments. Solutions of known PAP concentrations were prepared and measured by manipulating the nanopipettes on a micromanipulator in a custom faraday cage. The performance of the two nanoelectrodes was compared to commercially available electrodes of differing form factors. By effectively showing the ability for the device to detect small concentrations of redox-active analytes, this sensor eliminates the use of larger external reference electrodes, paving the way for this technology to be widely used in the future. The resulting nanoprobe had a working and reference electrode in a footprint of 50 nm. The fabrication and material selection makes the system cost competitive with other electrodes that do not have the same size advantage.

2.5 Aligned CNT Arrays

The implementation of carbon nanotube technology into gene transfection technology was developed in the NBIL. The device is composed of millions of vertically aligned carbon nanotubes grown in an anodized aluminum oxide template allowing for many cells to be cultured in parallel [1]. This device was shown to be capable of transfecting nucleic acids into mammalian cells. Other transfection technologies (lipofection, electroporation, viral vectors, biolistic) are more time consuming and limited by the size of cargo, population, and cytotoxicity.

The device is an array of closely packed, hollow, and open-ended CNTs embedded in a thin, 13 mm sacrificial template made using template-based CVD. These CNTs have exposed tips that form a bed for the cells to be cultured on top. To expose the tips, one side of the device is reactive ion etched using boron trichloride plasma [20].

To transport molecules of interest into the cultured cells, solution is placed on the bottom surface of the CNT array and allowed to diffuse through the device and into the cells. This device is capable of culturing tens of thousands of cells simultaneously with each cell interfacing with ~900 CNTs. The act of molecule transfer into cells in parallel offers a distinct benefit over the injection of singular cells conducted with the CNT based nanopipettes.

Initial research used HEK293 and rat L6 myocyte cells and has shown the device to transfect Qdots, Dextran (16 mins, 3 kDa, 99% transfection), Plasmid DNA (3900 kDa, 84% transfection), and propidium iodide (20 min, .66 kDa) [1]. The proliferation of cells on the CNT surface was comparable to standard culture plates. The low toxicity of CNTs was confirmed by 97% cell viability measured after cell culturing up to 96 hrs. Additional research is attempting to validate more cell types and different cargo (drugs, proteins, etc.). Fluorescent microscopy was used to demonstrate the transfer of fluorescent dextran into cells within 16 minutes of interaction. This result contrasts with control experiments in which dextran did not permeate cells incubated with dye infused growth media. In an additional experiment, 40000 L6 cells were transfected with propidium iodide simultaneously. Such rapid drug delivery is promising in biological and pharmaceutical research.

These amorphous CNTs are roughly 200 nm in diameter (200 nm OD and 140 nm ID spaced 200 nm, protruding ~180 nm from membrane) and can range between 60 to 100 μm long.

One device consists of millions of CNTs embedded in an AAO disc of 13 mm in diameter. To achieve these CNTs the NBIL uses a specific version of this CVD process to manufacture the gene transfection devices of interest; this begins by annealing the template at 730 ºC between two quartz plates for 4 hrs. Templates made of anodized aluminum oxide (AAO) have been employed due to their high softening temperature and dimensions of 60μm thickness and nominal pore diameter of 200nm. The template is then placed in a CVD furnace filled with argon gas flowing at 100 sccm at a temperature of 705 ºC. Next, a 30% Ethylene/Helium mixture flowing at 60 sccm is injected into the furnace for ~5 hrs. After the carbon is deposited, the membrane is cooled to 100ºC. This process produces CNTs with a diameter of roughly 200 nm and a thickness of roughly 25 nm. To expose certain parts of the newly formed CNT arrays, the device is wet etched to desired form. These amorphous tubes are ideal candidates for use in molecular transport applications [1].

2.6 Flow Through CNT Arrays

Fluid transport through nano structures is a widely studied topic. The prospect of micro laboratories and implantable chemical sensors has created a demand for the characterization of molecular transport through nano structures. The unique characteristics of carbon nanotubes make them good candidates for flow experiments. The dimensions of nanostructures have prompted much study of the breakdown of continuum mechanics and the usefulness of Navier-Stokes equations. The presence of slip lengths due to the size of CNTs in relation to molecules like water has been investigated [21]. Various methods for measuring flow through nano conduits include pressure driven flow, capillary action, and electrically induced flow.

Pressure driven flow specifically has been thoroughly characterized due to the prospects of enhanced flow. SWNT and MWNT arrays have been investigated as candidates for fast fluid transport under pressure driven flow. To quantify the transport of molecules in multi walled carbon nanotubes (1.6-7 nm diameter), Majumder et al. observed flow velocities much higher than anticipated [22]. The velocities observed were 4 to 5 orders of magnitude higher than predicted by the Hagen-Poiseuille equation. This factor of 4 to 5 magnitudes was termed flow enhancements. The results were assumed to be due to extremely low friction between the solutions and the graphitic walls. The hydrophobic nature of the carbon walls creates a layer of ordered hydrogen bonds that allow other water molecules to slip past more quickly. Slip lengths

are used to quantify the lack of friction between fluids and the carbon walls. Slip lengths were found to be 39 μm to 54 μm. The large fluid transport provides a good mimic of biological protein channels, leading to many uses in pharmacology, biology, and chemistry.

The experiments of Majumdar spawned many additional studies to verify or expand upon the findings. Whitby et al. [23] set out to apply the methods of Majumder et al. [22] to amorphous carbon nanotubes. Pressure driven flow had not yet been explored in carbon tubes of ~50 nm. Such enhanced flow is related to a hydrogen bonding layer between the walls of the tubes and the fluid flowing through causing extremely low friction. The nanotube arrays of this study are very similar to the arrays produced in the NBIL. Membranes to be used in experiments were made using AAO template-based CVD. The sealing mechanism of this study was a brass adapter that is compatible with stainless steel 13 mm filter holders. Chemically resistant epoxy cement was used to obtain a fluid tight seal. A metal grid was placed behind the array to mitigate micro cracking. End results were reported with and without the resistance correction of the metal support grid. Flow rate was correlated to syringe pressure and plotted to establish a measurement for flow. When compared to the magnitude of enhancement from Majumder et al. [22], the enhancement found by Whitby et al. was not as large. Additionally, results do not agree with the observation that more hydrophilic materials travel faster through the arrays. It is speculated that discrepancy in results could be linked to diameter difference between the MWNTs used.

Thomas et al. [24,25] published literature contesting the findings of Majumder et al. [22]. By using molecular dynamics simulations, the enhancement values found in previous studies were shown to be over calculated. The MD simulations found that transport through CNTs can in fact be described by the slip-modified Hagen-Poiseuille equation. Thomas et al. created a mathematical model that was within 10% agreement with MD simulations for CNTs of diameter 2.11-4.99 nm and 25% agreement for 1.66nm diameter. The flow enhancement found was 433 which is significantly below the enhancement found by Majumdar et al. It is suggested that a miscalculation of available flow area could have caused the excessive enhancement values found in previous studies. Whitby et al. [23] also found slip lengths larger than predicted for 44 nm CNTs, but various characteristics of amorphous tubes could contribute to the slip lengths. Additional studies have been conducted using MD simulations. Xu et al. [26] studied the effect

of cross-sectional shape on fluid transport in CNTs. It was found that more circular shapes have lower friction coefficients. Friction stabilizes when the effective radius reaches 1 nm.

In a study by Bau et al, microfluidic properties were studied in amorphous carbon nanotubes [21]. The goal of the study was to review and expand upon knowledge of how liquid travels through nanostructures. CNTs were chosen specifically for the wide range of tube diameters that could be used. The CNTs used had diameters of roughly 250 nm and were produced using CVD. Individual tubes were isolated by manipulating them in isopropanol solution with di-electrophoresis. Using scanning electron microscopy, the temperature of the microscope stage was varied to observe condensation and evaporation within the tube. The transparency of amorphous CNTs allowed for the expansion of this study to the evaporation and capillary action of many substances using an inverted microscope. These observations lead to the conclusion that the tubes are hydrophilic due to the specific synthesis of the tubes.

The aligned CNT membranes developed by the NBIL have been used in pressure driven flow characterization [27]. The CNT array was mounted to a stainless-steel filter holder and attached to a syringe pump. The variation in pressure was compared to the volumetric flow rate. The fluid passing through the array was weighed to measure the volumetric flow rate. A modified Hagen-Poiseuille equation was used to compare experimental data to theory. The experimental data aligned well with the analytical model with an error of 6%.

The flow of fluid in CNTs has been characterized in many ways in the literature. However, the measurement of passive transport through amorphous carbon nanotubes is a gap within the knowledge. The application of passive transfection in the NBIL devices necessitates further study of the microfluidics of carbon nanotubes.

2.7 Passive Transport Through CNT Arrays

As shown, the study of fluid transport has been widely studied. However, the study of diffusion through carbon nanotube arrays has yet to be properly investigated. The gene transfection devices created by Golshadi et al. utilize diffusion for molecular transport [1].

In a study by Jensen et al. [28], diffusion flow through the arrays of CNTs developed by the NBIL was characterized. A novel method to measure the changing concentration of two reservoirs separated by a CNT array was produced. The luminous intensity of a solution containing fluorescent molecules was correlated to changing concentration. It was hypothesized that by increasing the active surface area of the CNT arrays the rate of diffusion would increase. To measure the rate of diffusion a monochrome camera (AxioCam MRm) was attached to an upright microscope and captured images of the surface of a CNT array every 0.5 seconds. Using ImageJ software to analyze a region of interest (ROI) from the captured images, the luminous intensity of each pixel was averaged for each time interval.

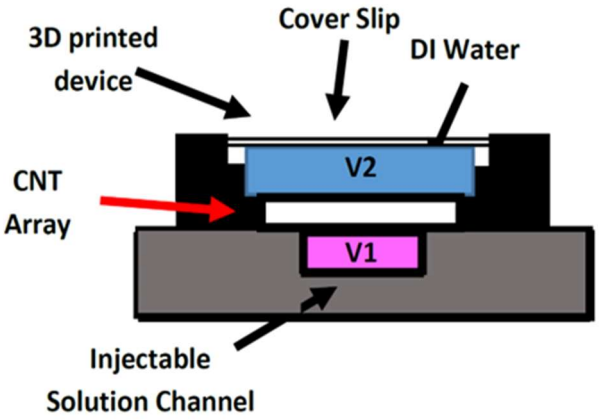

Figure 1: Schematic of device created by Jensen et al. Apparatus features two reservoirs separated by a CNT membrane. This device interfaces with a microscope to detect changes in fluorescent molecule concentration.

The device displayed in Figure 1 was made using 3D printing techniques that embedded the membrane in the PLA structure [29]. The 3D printing approach provided a method of isolating desired active areas of the AAO membrane for fluorescent dye to diffuse through. SEM imaging was conducted to observe the interface of the PLA with the exposed CNT tips and ensure unintended clogging did not occur. A two-step printing process led to a bottom trough of a desired geometry. The AAO or CNT array was placed on top of the print and encased with the second layer. The second print had a reservoir open to the atmosphere to interface with the fluorescent microscope. These devices were designed to be single use for the fear of contamination associated with multi-use devices. The advantage of clean devices was limited by the high material cost and low throughput process of reprinting of devices. Advances in 3D printing and diminishing costs associated with additive manufacturing are thought to add to the appeal of single use devices. Micro cracking proved to be a major obstacle to overcome. Using SEM imaging, it was found that membrane holders with exposed surface areas greater than 6mm led to cracking of the membranes. The residual stresses of thermal expansion of 3D printing and possible mishandling of test devices led to observed micro cracks.

After experimentation with CNT arrays, an unexpected lack of diffusion occurred. When deionized water mixed with dextran was used as the test solution, there was a blockage preventing dextran from moving through the CNTs. Various solutes (Dextran, quantum dots, Propidium Iodide (PI)) and solvents (DI water, PBS, ethanol) were used to ensure that DI water and dextran did not have atypical interactions with the amorphous walls. Flow through CNTs only occurred when ethanol was used. Various attempts at producing arrays with CNTs that permitted diffusion with DI water yielded no promising results.

To continue with the experiment, the study was adjusted to look at solely Anodized Aluminum Oxide Membranes without CNTs. Despite the various challenges with experimentation, it was found that the total time for diffusion increased as active surface area of the CNT array decreased. The experimental curves produced from data were curve fit to estimate the settling time of diffusion. By comparing the settling time of different active surface areas, it was found that as active surface area increased, the diffusion time decreased [28].

The discovery of graphene and carbon nanostructures has created many tools for a wide range of applications. The use of amorphous carbon nanotube arrays for gene transfection of cells provides a more efficient and less toxic method of drug delivery. Current understanding of passive transport through carbon and other microstructures is limited. By studying and measuring the diffusion of molecules in these nanostructures, the interactions between biological systems and this biocompatible material can be understood.

3.0 Experimental Approach and Methods

To measure the diffusivity of a system with a carbon nanotube array, a procedure for measuring changes in concentration was needed. A device was designed to seal the carbon nanotube array in between two reservoirs of specific volume. This device had the ability to alter the reservoir volume, active area of the array, and the solution concentrations to understand how these parameters affect diffusion. A method using fluorescent spectroscopy was developed in which the fluorescent intensity of samples was monitored at specified time intervals. The diffusivity was calculated from these data points and compared to an analytical model.

3.1 AAO Templates and CNT Manufacturing

The carbon nanotube array devices designed by the NBIL start with a sacrificial template of anodized aluminum oxide. These templates are porous with a pattern of holes that have relatively even spacing and consistent pore diameter. These anodized aluminum oxide discs are commercially available with many pore diameters and pore densities. For this study AAO membranes with holes of a 200 nm diameter and thickness of 60 micrometers were used (Whatman Anodisc 13, Cat. No.: 6809-7023).

Carbon nanotube arrays were added to the AAO membranes using carbon vapor deposition. These CNT arrays were manufactured using the methodology outlined by Golshadi et al. [28]. In this method a tube furnace (Carbolite, TZF17/600, inner tube diameter: 7 cm, tube length: 152 cm) was used for the deposition process. A line of AAO membranes was placed with the pore axis aligned with the tube axis. The temperature of the tube furnace was increased to 700 ºC and argon gas flowed into the chamber at 100sccm. To begin the deposition process, a mixture of 30 percent ethylene and 70 percent helium gas was added to the chamber with a flow of 60 sccm. The deposition process lasted for a total of 5 hours and was followed by a cool down period where the argon gas flow was reintroduced. The CVD process results in layers of amorphous graphitic carbon on the inner pores and surface of the AAO membrane. These carbon nanotube arrays were manufactured by M. Schrlau and members of the NBIL for use in this diffusivity study.

3.2 Sealing of the CNT Array

The sealing of the AAO/CNT membrane is crucial to isolating an active area of interest and overcoming occurrences of cracks along the AAO template (micro cracks). Such a method of sealing must also interact with the experimental device to provide a watertight seal. Initial research heavily focused on identifying mechanisms of sealing.

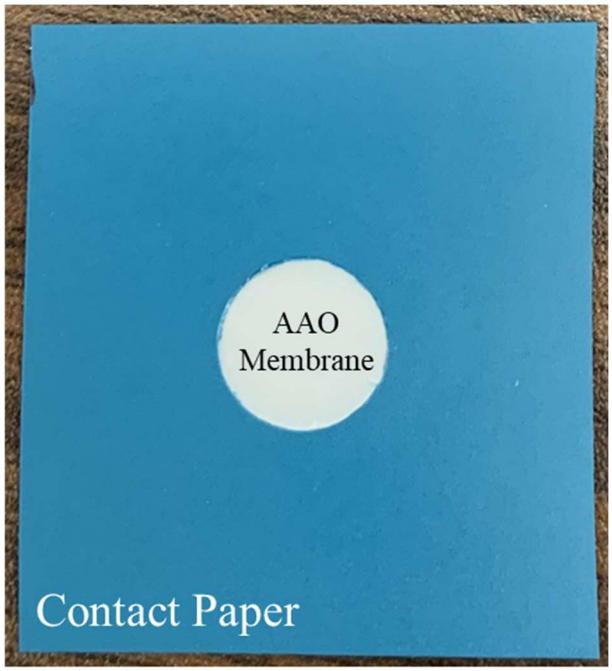

Figure 2: AAO membrane embedded in two pieces of contact paper. Both pieces of contact paper have a 13mm hole that is lined up with the 15mm AAO membrane.

Previously, 3D printing of a device around the CNT/AAO membrane was explored by Jensen et al. [28]. In this work, a base with a reservoir of 20 µL was manufactured out of Polylactic Acid (PLA). The membrane to be used was placed within the design and a second round of 3D printing was conducted on top of the membrane to create a seal with a second reservoir of 80 µL on top of the device. The dimensions of the 3D print were designed to interface with a fluorescent microscopy device. Due to thermal fluctuations, the membranes were prone to micro cracking since the dimensions of the device would change as the 3D print cooled. Additionally, 3D printing a device around the membrane required single use devices which limited throughput and increase waste associated with experimentation.

Various methods for sealing the AAO/CNT membrane in the device were considered. Specific constraints led to the final methodology for sealing. The method developed had to isolate the desired active surface area while avoiding chemical degradation of CNT walls due to wet chemistry processes. In addition, avoidance of micro cracks due to the brittleness of the arrays was the main objective of the new method.

To seal the AAO/CNT arrays the method of surrounding the membrane with vinyl contact paper was developed, as shown in Figure 2. A template was used to trace the desired dimensions into the vinyl and mark out the placement of a 10 mm hole in the center of the contact paper. A punch and hammer were used to cut a hole of 7.94 mm in the footprint of the 10 mm hole.

To create the contact paper and membrane pairing, a procedure was developed to handle and place the CNT array within a specified acceptable area. A vacuum pen was used to pick up the membrane. Using the vacuum pen, the array was placed on the center of the hole. All the reservoir systems designed had diameters of 15 or 17 mm leaving reasonable clearance for misalignment of the CNT membrane of 13 mm with the contact paper hole. The hole and edges of the second contact paper were aligned with the first contact paper. Any particulate was cleaned off the contact paper and exposed surface of the CNT array before placing the sealed array into the two-reservoir device.

The membrane/contact paper unit greatly reduced the number of array failures caused by handling of the arrays and experimental procedure. When clamped in the reservoir device, the active surface area of the membrane was easy to align due to the size of the vinyl sheets. The largest benefit of the contact paper attached to the arrays was the introduction of a clamping surface not directly in contact with the array. This clamping surface removes any unwanted pressure from the membrane surface that causes micro cracks.

A fluid tight seal was additionally required between the reservoir device and the contact paper. Initially, vacuum grease was chosen as it had been used in similar applications in the NBIL. The vacuum grease was painted on both sides of the contact paper and pressed between both sections of the reservoir device. A C-clamp was used to force the two reservoirs together and create a fluid tight seal around the AAO membrane. After initial experimentation the fluorescent dye aggregated to any vacuum grease that was squeezed into the reservoirs. For later

reservoir designs, the clamping mechanism was changed to bolts allowing for a higher clamping force compared to the C-clamp.

The contact paper slips encasing the carbon nanotube array and the bolt clamping apparatus proved to be robust ways of isolating an active surface of carbon nanotube. For future work, the contact paper can be easily altered to change the area through which the fluorescent dye can diffuse. As shown in the analytical model, this parameter can be studied to understand its effect on the rate of diffusion across the CNT array.

3.3 Commercial Fluorescent Spectrometer

Spectroscopy involves the collection and interpretation of light after it interacts with a solution of interest. Fluorescent spectroscopy is a type of spectroscopy in which the light of a specific wavelength is directed at a solution containing fluorescent molecules. These molecules absorb and re-emit the light in a spectrum of lower energy. As the concentration of the fluorescent molecules in solution increases, the peak of the emission spectrum predictably increases. The intensity of the emission spectrum will change linearly with changes in fluorescent molecule concentration within a certain band. The robustness of the spectrofluorometer, in conjunction with a well-designed apparatus able to monitor diffusion on both sides of the CNT array, will allow for accurate measurement of concentration change in both reservoirs as a function of time.

A spectrofluorometer is a device that bombards a solution with a laser of specific wavelength and detects the emission spectrum of the reflected light. The intensity of the emission spectrum will change proportionally with changes in fluorescent molecule concentration. This device is a Jasco FP-8500 fluorescent spectrometer. The wavelength of the emission laser can be set to a desired wavelength. The solution interacts with the laser and the reflected light is collected and analyzed. By increasing the concentration of the solution, the peak of the emission spectrum increases linearly with concentration.

Spectroscopy requires the collection of samples from the reservoir device. These samples are placed in cuvettes requiring 70 μL of solution. This volume must be factored into analysis of the data and the experimental procedure used. The collection of part of the volume will limit either the usable samples collected from an experiment or will increase the number of

experiments needed. The concentration cannot be measured continuously but must instead be measured at discrete time points. For a molecule like fluorescein salt this sampling procedure is beneficial, as photo bleaching can occur when the molecule degrades from over exposure to the laser light leading to lower concentration readings.

Initial experimentation was conducted using an optical table fluorescent spectrometer. Work with this tool is discussed in Appendix C. The availability of this setup was altered after a few experiments resulting in the switch to the Jasco FP-8500.

3.5 Fluorescein Salt

The molecule chosen for the study utilizing fluorescent spectroscopy was fluorescein disodium salt (Cas No.: 518-47-8). The wide use of fluorescein salt as protein labels makes this molecule important for the long-term study of cellular transfection using carbon nanotube arrays. This molecule is widely utilized in the fields of biology and chemistry in applications such as protein labeling, immuno-histological staining, and immunofluorescent labeling [30].

The relatively small size of fluorescein salt allows for quick diffusion in the carbon nanotubes which ensures debugging of procedure and device unlike large proteins that may interact with the CNT array. Fluorescein salt has molecular radii approximated as 9.51 and 5.71 nm. The molecular size of fluorescein salt allows for the estimation of diffusion for similar organic compounds that are of interest in cell work. Ultimately, this study will expand to that of proteins and genetic material which can be tagged by fluorescein salt and other fluorescent molecules.

The excitation spectrum is the range of light that will cause a fluorescent molecule to fluoresce. The emission spectrum is the range of light emitted by an excited fluorophore. For fluorescein salt the peak of the excitation spectrum occurs at 494 nm and the peak of the emission spectrum occurs at 517 nm [31]. Figure 3 shows the excitation and emission spectra obtained from the SpectraVeiwer tool by ThermoFisher Scientific.

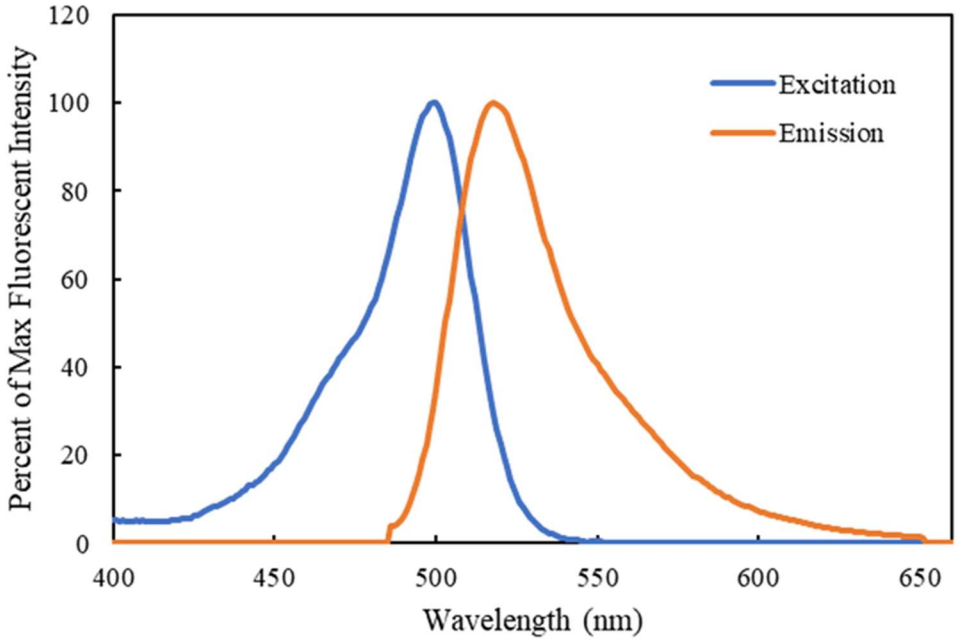

Figure 3: Excitation and emission spectra of fluorescein disodium salt (Cas. No.: 518-47-8). The excitation spectra has a peak at 494 nm and the emission spectra has a peak at 517 nm.

When using fluorescein salt, this molecule has a dependence on pH and photobleaching that will impact the fluorescent intensity of a sample. Photobleaching occurs when a fluorophore is exposed to a high intensity light source for an extended period. This excitement causes the molecule to break down and lose its fluorescence. The dependence of fluorescent intensity on pH was studied by Sjöback et al. [32]. For low pH values, the intensity peak of fluorescein salt is severely quenched. As the pH of the solution is increased to a more basic solution, the peak of the emission spectra increases.

3.6 Procedure for Calibration Curve

To measure the concentration of the samples taken from solution, the relationship between fluorescent intensity measured by a spectrofluorometer must be calibrated to the molecule of interest.

The relationship between concentration and fluorescent intensity can be approximated by equation 3.6.1, in which the fluorescent intensity measured (Γ) is dependent on the intensity of absorbed light (I_a), path length of the cuvette used (L_c), molecular extinction coefficient (a), fluorescence efficiency of the fluorescent particle (Q), and the concentration of the solution (φ).

From this equation it can be shown that a linear calibration curve can be obtained relating the concentration of the solution to the fluorescent intensity measured.

$$\Gamma = Q * I_a * a * \varphi * L_c \tag{3.6.1}$$

However, there exists a phenomenon labeled “internal filtering effect” [33] in which the linear relationship between concentration and fluorescent intensity breaks down. This effect is caused when emitted electrons become reabsorbed by neighboring particles forming a cycle of emission and absorption that causes the fluorescent intensity spectrum to be quenched. An analytical solution is highly dependent on the spectroscopy tool and cuvette type used. Thus, an experimental method of creating a calibration curve from a known series of concentrations provides a robust and easily attainable calibration curve.

To construct the curve experimentally for fluorescein salt, a solution of known concentration was created. By using fluorescein salt powder purchased from Sigma Aldrich (Cas No.: 518-47-8). The mass (m_{powder}) was added to a specified volume (V_{DI}) of deionized water. The concentration of the solution is dependent on the molecular weight (W_{mol}) of the molecule and was calculated from the following equation:

$$\varphi = \frac{m_{powder}}{W_{mol} * V_{DI}} \tag{3.6.2}$$

A dilution series was created to find the change in fluorescent intensity throughout the range of 1.43 μM to 1.43 mM. Samples were inserted into the fluorescent spectroscopy device and the emission spectrum was recorded.

3.7 Control of pH of Solution

After initial experimentation, the chemical interactions between the fluorescein solution and the aluminum reservoirs resulted in an increase in pH and rise in fluorescent intensity for a given concentration. To combat the effect of pH change on the measurement of diffusion, the pH of the DI water used to make the solution was increased to a pH in the range of 7.5-8 pH. In this range the increase of fluorescent intensity as a function of pH begins to asymptote. A 0.2 N solution of Sodium Hydroxide (CAS No.: 1310-73-2) was chosen to alter the pH of solutions.

A digital pH tester pen was calibrated using buffers for pH 6.86 when added to a known volume. Three measurements of pH of the fluorescein solution were recorded for the initial pH. By adding 0.2N sodium hydroxide solution to volumes of 40 mL DI water, the rise in pH was recorded. For diffusion experiments, a pH of 7.7 was targeted due to the pH curve in section 5.1.

3.8 Experimental Device Design

Studying the diffusion of molecules across the CNT array required an experimental device to determine the concentration of fluorescein salt. A device capable of housing a CNT array and interfacing with the spectrofluorometer was developed. The device was made up of two reservoirs separated by an AAO/CNT membrane. By taking measurements from both reservoirs, the passive transport of the molecule of interest was studied. This capability of monitoring both reservoirs facilitated the investigation of events like absorption by the CNTs.

Device designs 1, 2, and 3 are discussed in Appendix D. The iteration of designs was driven by improvements in manufacturing and changes in material selection. Early occurrences of array cracking during experimentation led to an interlocking design for the two reservoirs. bolts were used to clamp the reservoirs together to remove the use of vacuum grease.

Version 4 of the reservoir system is shown in Figure 4. In this model, the two reservoirs interlock to avoid micro cracking of the CNT array during setup and tear down of an experiment. This feature is important for explaining any blatant occurrences of fast diffusion attributed to large cracks. The reservoir volume ranged from 500 µL from 5000 µL to study the effect of volume of diffusivity. Device material was switched from aluminum to polypropylene from version 3 to version 4. The pKa of fluorescein salt is 6.4 [34] giving it similar acidity to carbonic and sulfuric acid [35]. Compatibility of plastics to fluorescein salt could not be found in the literature, but polypropylene was found to have apt chemical resistance to acids similar to fluorescein salt and stronger acids like hydrofluoric and acetic acid [36]. By switching to a more inert material, the change of pH was not seen in experiments with version 4.

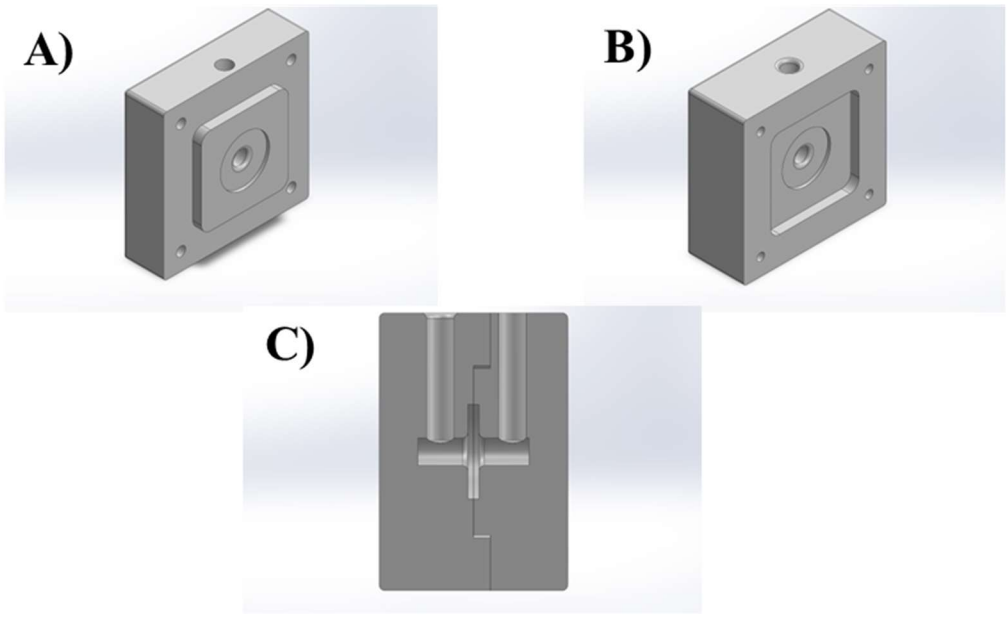

Figure 4: A) Version 4 of the reservoirs used to measure diffusion. The two reservoirs are interlocking pieces preventing twisting from occurring. **B)** The second interlocking piece has threaded holes to use bolts as a clamping apparatus. **C)** The volume of the fourth version of the reservoirs totals 1 mL. The goal of this design is to speed up time of diffusion from the 10 mL reservoir systems.

A 3D printed cap was created for design version 4 to mitigate the effects of evaporation on the experiment. These caps were placed on the top surface of the reservoirs and closed the access holes utilized to collect samples. Silicon was placed around the plugs as gaskets creating sealing from the ambient environment. Figure 5 shows the 3D printed caps with plugs.

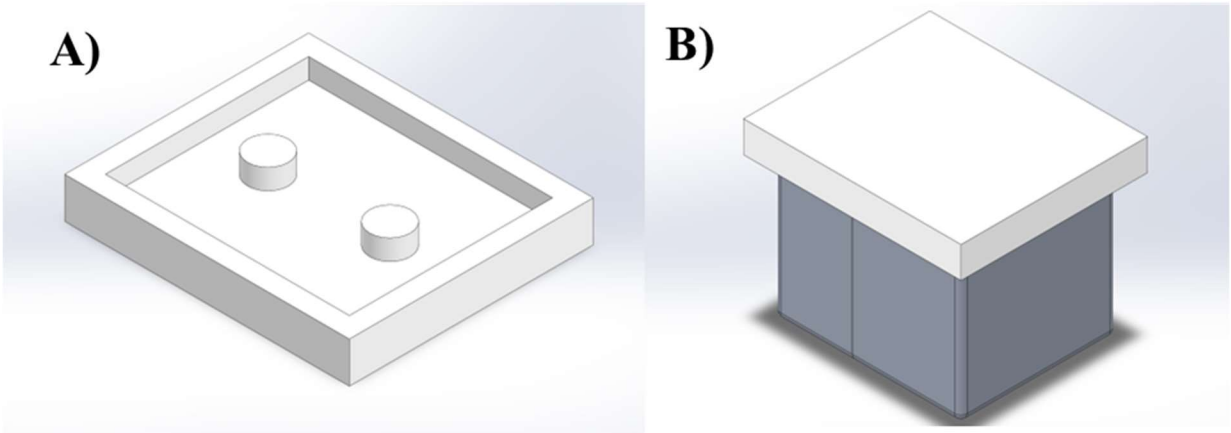

Figure 5: A) 3D model of cap printed to close the access holes of the two-reservoir experimental device. The cap is lined with silicon to act as a gasket that mitigates the evaporation of solution. **B)** The 3D printed cap fits over the two reservoirs.

3.9 Measurement of Concentration

Using the experimental devices developed, an experimental procedure was performed to measure the concentration of each reservoir. The procedure started by preparing a high concentration solution of fluorescein salt in DI water. Fluorescein disodium salt powder of roughly 5 mg was weighed out using scale with precision of ±0.01 mg. The five mg was added to 15 mL of DI water resulting in a solution of molarity 1.43 mM calculated using equation 3.9.1. Molecular weight of fluorescein salt is 376.3 g/mol [30].

$$\varphi_{Solution} = \frac{m_{actual}}{MW * V_{DI}} \tag{3.9.1}$$

A solution was prepared from the high concentration to achieve a solution within the linear range. For an experiment with reservoir version 4, a solution volume of 600 µL was needed. From this solution, 100 µL was taken for reference of fluorescent intensity at 0 hours.

After preparation of the solution, the CNT array was prepared by placing the array between two pieces of vinyl contact paper. The reference code for that array was documented and the array was placed into the reservoir system. The experiment began by placing 500 µL of the fluorescein salt solution of known concentration in one reservoir and 500 µL of DI water in the other reservoir.

For reservoirs with volume greater than 2 mL, a 100 µL sample was taken from each reservoir every 24 hours until 10% of the reservoir volume was sampled out of the experiment. For reservoirs with volume less than 2 mL a single sample was taken from the reservoir system in each experiment. The frequency and timing of sampling was dependent on the experimental purpose and reservoir size. The Jasco FP-8500 fluorescent spectroscopy machine is used to measure samples taken from reservoirs. The full fluorescent spectroscopy procedure is detailed in Appendix A. Plots were generated at a specific time interval, as shown in Figure 6.

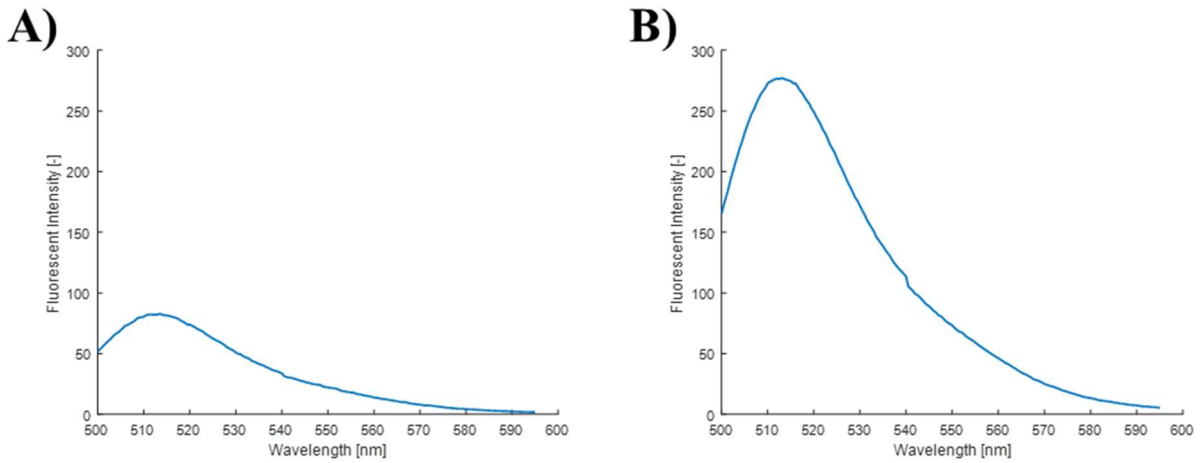

Figure 6: Graphs collected during experimentation in which fluorescein salt was allowed to diffuse through a CNT array. A plot was generated at different times of the fluorescent intensity of reflected light. **A)** Measurement at time of 24 hours for reservoir will initial concentration of approximately 10.01 µM. **B)** Measurement at time of 48 hours for reservoir will initial concentration of approximately 10.01 µM. Features slight oversaturation of fluorescent intensity.

3.10 Summary of Experimental Approach

To achieve measurements of concentration, change across a carbon nanotube array, a two-reservoir system was designed. These CNTs were placed into a vinyl contact paper substrate for improved handling and mitigation of array cracking. The combination of reservoir and contact paper allowed for the altering of volume and active radius for the study of diffusion sensitivity to system dimensions.

Following the design and fabrication of the two-reservoir device, a procedure was developed utilizing fluorescence spectroscopy. A Jasco FP-8500 was used to sample the reservoirs at 24-hour time intervals. The samples were correlated to a calibration curve to generate a plot of the change in concentration of both reservoirs over time. These concentration values were then used to calculate diffusivity in section 5. Figure 7 depicts the procedure using the reservoirs to measure diffusivity of the system.

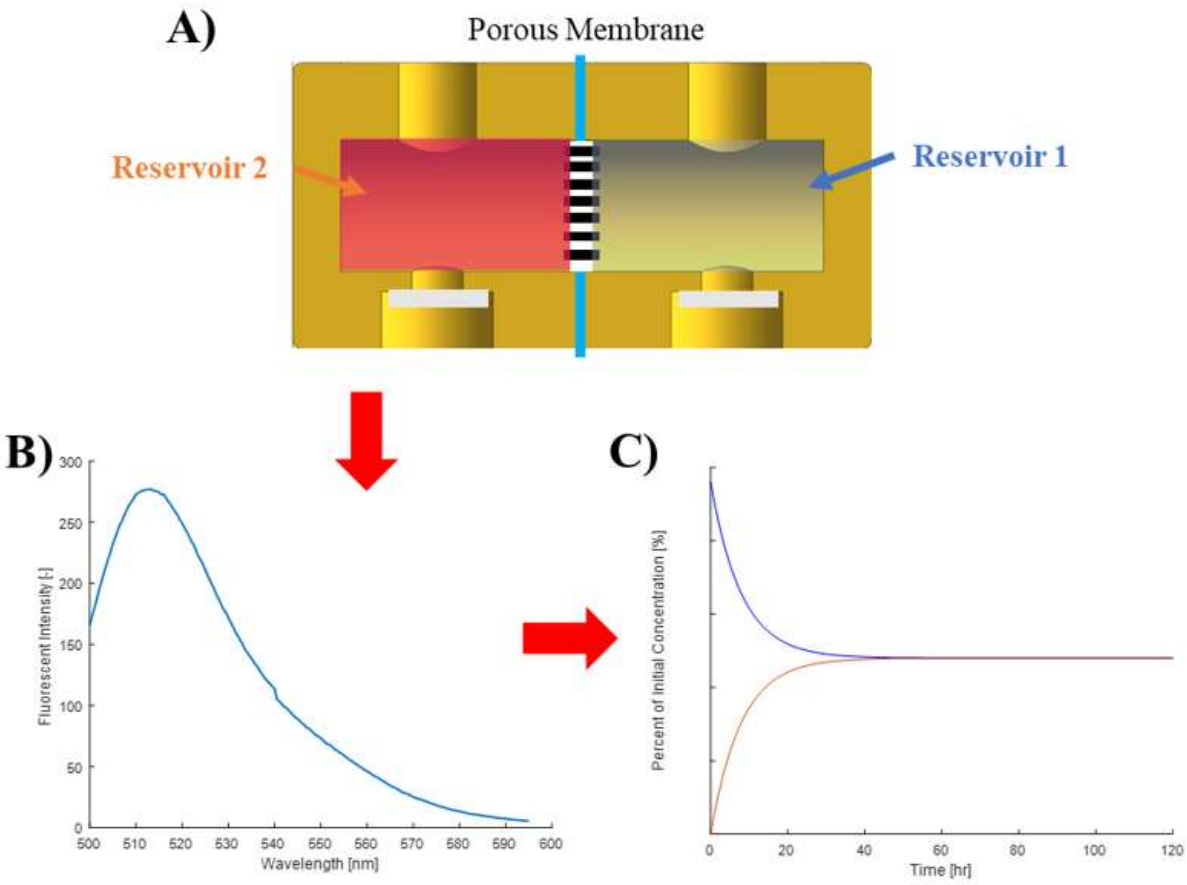

Figure 7: Concept for experimentation and characterization of diffusion. **A)** Proposed device with concentration gradient. **B)** Data collected by photo sensor. The fluorescent intensity of the specific wavelengths reflected from the fluorophores. **C)** Graph relating the change in fluorescent intensity (proportional to concentration) to time. This graph is made from a fluorescent intensity measurement for each reservoir taken at a specified time interval.

4.0 Analytical Model of Diffusivity

The development of a mathematical model to predict the behavior of molecular transport is essential for the study of particles of varying size through carbon nanotube arrays. An easy way to estimate diffusivity is crucial in employing carbon nanotube arrays for widespread use. Such a model would ideally be suited to handle parameters such as molecular size, type of solution, and system dimensions. The following section details efforts to develop such a model using derivations of the Stokes-Einstein equation and Fick's laws of diffusion. Fick's second law is used to first predict the gradient of fluorescein salt in a singular carbon nanotube to establish penetration timescale. A simplified version of Fick's first law is then derived for the prediction of changing concentration in the larger reservoir system. Figure 8 depicts the system modeled.

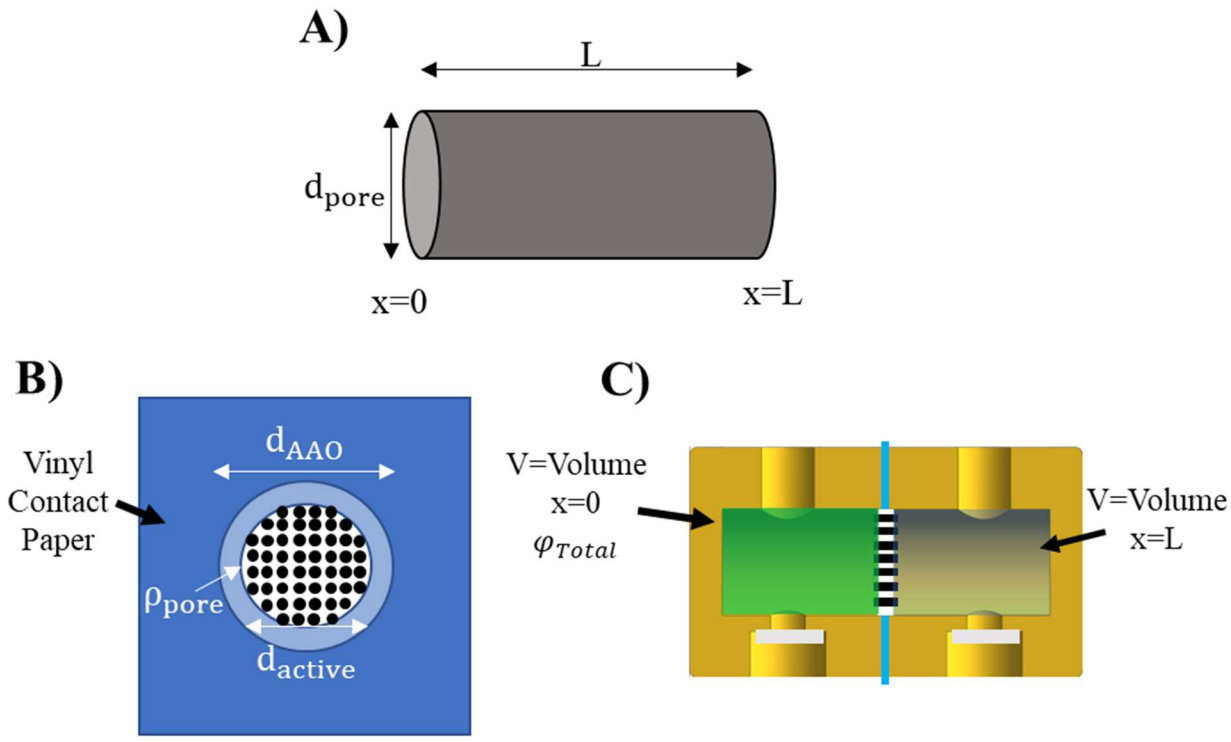

Figure 8: Schematic of system characterized by the analytical model. **A)** Singular carbon nanotube with dimensions for length (L) and diameter (d_{pore}). **B)** Carbon nanotube array encased in vinyl contact paper. The active diameter (d_{active}) is smaller than the full diameter of the CNT array (d_{AAO}). The pore density (ρ_{pore}) describes how closely packed the CNTs are in the AAO membrane. **C)** The CNT array is enclosed in a two-reservoir system. At position x=0 a concentration of fluorescein salt is added at time 0 hours. DI water is added to the reservoir at position x=L. Each reservoir has a volume (V) of either 5, 2, or 0.4 mL.

4.1 Stokes-Einstein Equation

The diffusivity of a molecule in solution is an important parameter to understand when modeling diffusion. For the comparison of experimental results to an analytical model, diffusivity must be found through theory. To estimate the diffusivity of the solution of interest, the Stokes-Einstein Equation can be used.

The Stokes-Einstein equation states that the diffusivity of a molecule in solution is equal to the temperature (T) times the Boltzmann constant (k) divided by the frictional coefficient (f).

$$D = \frac{k * T}{f} \tag{4.1.1}$$

The frictional coefficient of a particle as it moves through a solution is related to the viscosity (η) of the liquid through which the particle of interest is moving, as well as the shape of that particle. G. Stokes [37] was able to show that this frictional coefficient can be estimated by equation 4.1.2 in the case of spherical particles where the radius (r) is introduced.

$$f = 6\pi * \eta * r \tag{4.1.2}$$

After substituting equation 4.1.2 into equation 4.1.1, the Stokes-Einstein equation is found to be expressed in equation 4.1.3 which is valid only in the case of perfectly spherical particles. A quick approximation can be made for any molecule with the understanding that non-spherical molecules require a correction factor for true estimation of diffusivity. To build on the estimations of G. Stokes, Perrin [37] completed a derivation for particles of ellipsoidal shape. A correction factor was mapped depending on the ratio between radii of the different axes.

$$D = \frac{k * T}{6\pi * \eta * r} \tag{4.1.3}$$

The radii of the ellipsoid can be used to find the equivalent spherical radius. Equation 4.1.4 details the conversion of the major (a) and minor (b) ellipsoidal radii to spherical radii by equating the volumes of such shapes.

$$r = \left(\frac{3}{4\pi} * \left(\frac{4}{3}\pi * a * b^2\right)\right)^{\frac{1}{3}} \tag{4.1.4}$$

After adding this correction factor ($\frac{f}{f_0}$) to the Stokes-Einstein equation, equation 4.1.5 shows the estimated diffusivity of an ellipsoidal particle.

$$D = \frac{k * T}{6\pi * \eta * r * \frac{f}{f_0}} \tag{4.1.5}$$

The equation shown can be used with values for Boltzmann constant [38] and viscosity of water [39] found in the literature. The conditions of the experiments were assumed ambient due to temperature measurements of the NBIL.

The diffusivity described by equation 4.1.5 assumes an open volume for diffusion to occur. The carbon nanotube array is a porous medium which introduces properties such as porosity (ϕ) and tortuosity (τ) [40]. Equation 4.1.6 shows the relationship between the diffusion calculated by the Stokes-Einstein equation (D) and the properties discussed.

$$D_{eff} = D * \frac{\phi}{\tau} \tag{4.1.6}$$

Due to the flow of molecules through confined spaces amid a larger volume, these properties account for the frictional increase due to small and twisting flow paths. Porosity is the amount of void volume throughout a solid volume. Equation 4.1.7 shows the calculation of porosity.

$$\phi = \frac{L * \pi * {r_{pore}}^2 * \rho_{pore} * \pi * {r_{Array}}^2}{L * \pi * {r_{Array}}^2} = \pi * {r_{pore}}^2 * \rho_{pore} \tag{4.1.7}$$

Tortuosity accounts for the increased distance traveled for paths that are longer than the length of the structure. Since the pores of the AAO membrane and CNT array are straight and cylindrical the tortuosity is estimated to be one.

Fluorescein salt is not a spherical molecule but can be described by an ellipsoidal shape as seen in Figure 10. The chemical has a major and minor axis when the range of the electron orbitals are taken into consideration, an ellipsoid is a valid approximation of fluorescein salt's shape. The structure of fluorescein shown in Figure 9 was analyzed using the chemical structure obtained from PubChem [41].

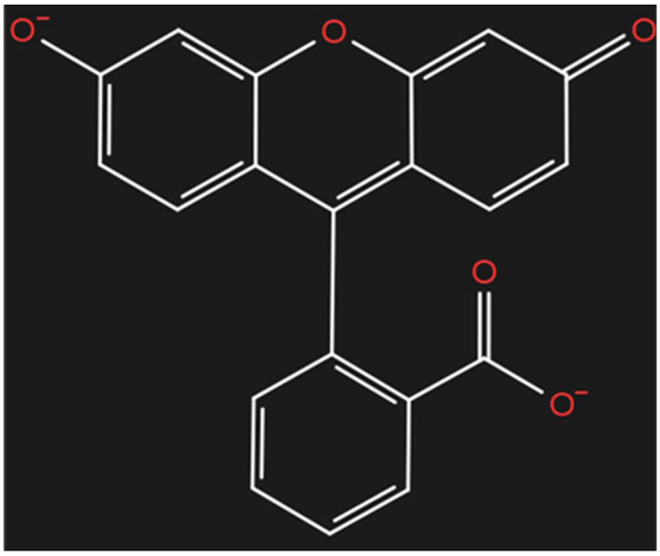

Figure 9: Chemical structure of fluorescein sodium salt without the sodium ions.

A measurement of the diameters of the molecule was conducted using a software called Schrodinger. This software utilizes the chemical structure of a molecule to construct a three-dimensional model. This model considers the Van-der Waals radii associated with the distance at which this molecule would interact with other molecules. This radius is important as diffusion of individual molecules is dominated by the frictional interactions with the solution. Fluorescein sodium salt is an ellipsoidal particle with a major radius of 9.51 Å and minor radius of 5.71 Å shown in figure 10. The ratio $\frac{a}{b}$ is calculated to be 1.6654 based on equation 4.1.8. The correction factor $\left(\frac{f}{f_0}\right)$ mapped by Perrin et al. is 1.05.

$$\frac{a}{b} = \frac{Radius\ of\ Major\ Axis}{Radius\ of\ Minor\ Axis} \tag{4.1.8}$$

Using equation 4.1.6 and 4.1.8, the diffusivity of fluorescein salt is calculated to be $2.85 * 10^{-1}\ \ \frac{m^2}{s}$. This calculation is in the same regime as acetic acid ($9.1 * 10^{-10}\ \frac{m^2}{s}$) and ethanol ($10.0 * 10^{-10}\ \frac{m^2}{s}$) in water, but results in a faster time to equilibrium [42].

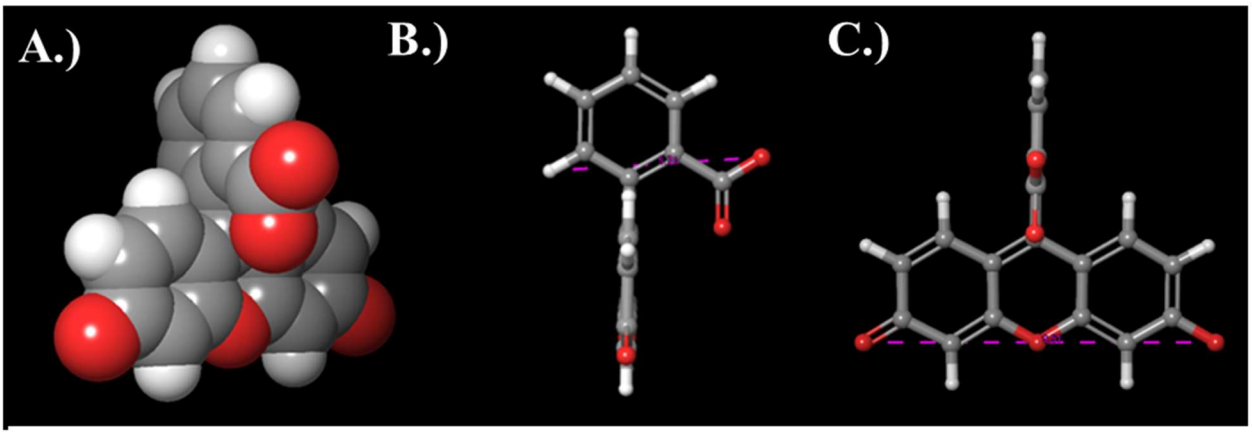

Figure 10: Models of fluorescein salt for the measurement of the major and minor Van der Waals radii. **A)** Model of fluorescein sodium salt showing the interaction space of each atom. **B)** Measurement of the minor axis (5.71 Å) using the Schrodinger software. **C)** Measurement of the major axis (9.51 Å) using the Schrodinger software.

Table 1 includes the value of diffusivity found from the analysis of the Stokes-Einstein equation. The effective diffusivity of fluorescein is calculated to be $5.17 * 10^{-11}\ \frac{m^2}{s}$.

Table 1: Values used for the calculation of effective diffusivity of fluorescein salt in a solution of DI water.

Coefficient	Units	Value
k	[J/K]	1.31E-23
T	[K]	2.93E+02
η	[mPa]	1.00E-03
a	[m]	9.51E-10
b	[m]	5.71E-10
f/f_0	[-]	1.05
D	[m^2/s]	2.86E-10
ϕ	[-]	1.79E-01
D_eff	[m^2/s]	5.10E-11

4.2 Fluorescein Salt Penetration of CNT

Diffusion is the primary mode of molecule transportation used for the transfection device of interest. Diffusion is a widely studied section of fluidics in which molecules in solution with another substance will move to regions of lower concentration from regions of higher concentration until a state of equilibrium is reached. This movement of one substance relative to another is described by Fick's first and second laws [43].

Fick's second law for one dimensional diffusion states that the second derivative of concentration (φ) with respect to space (x) is equal to the first derivative of concentration with respect to time (t) divided by the diffusivity of the molecule of interest.

$$\frac{\partial^2 \varphi}{\partial x^2} = \frac{1}{D} * \frac{\partial \varphi}{\partial t} \tag{4.2.1}$$

Concentration can be split into a steady state and transient solution. The steady state solution, $v(x)$, is a function of space while the transient solution still contains time dependency.

$$\varphi(x,t) = v(x) + w(x,t) \tag{4.2.2}$$

For the experimental setup used, Dirichlet boundary conditions represent the reservoir concentrations during the time of molecule penetration of the carbon nanotubes. Equations 4.2.3 and 4.2.4 show that the boundary conditions can be allocated to the steady state solution and the transient solution will receive boundary conditions of zero.

$$\varphi(0,t) = v(0) + w(0,t) = \varphi_0 \tag{4.2.3}$$

$$\varphi(L,t) = v(L) + w(L,t) = \varphi_L \tag{4.2.4}$$

The steady state solution is found by substituting $v(x)$ for $\varphi(x,t)$. Since $v(x)$ does not have a dependency on time, the right-hand side of equation 4.2.5 will be equal to zero.

$$\frac{\partial^2 v}{\partial x^2} = \frac{1}{D} * \frac{\partial v}{\partial t} \tag{4.2.5}$$

Solving the differential equation by integrating the second derivative of $v(x)$ with respect to space yields a linear steady state solution represented by equation 4.2.6.

$$v(x) = c_1 x + c_2 \tag{4.2.6}$$

The initial conditions shown in equations 4.2.3 and 4.2.4 can be used to find coefficients c_1 and c_2. The variable L is introduced to represent the length of an individual carbon nanotube.

$$v(x) = \frac{\varphi_l - \varphi_0}{L} * x + \varphi_0 \tag{4.2.7}$$

The transient solution has both a time and space dependency resulting in the partial differential equation shown in 4.2.8.

$$\frac{\partial^2 w}{\partial x^2} = \frac{1}{D} * \frac{\partial w}{\partial t} \tag{4.2.8}$$

The boundary conditions of the transient solution are equal to zero due to the boundary conditions of the whole solution being accounted for in the steady state solution as shown in equations 4.2.9 and 4.2.10.

$$w(0,t) = \varphi(0) - v(0,t) = 0 \tag{4.2.9}$$

$$w(L,t) = \varphi(L) - v(L,t) = 0 \tag{4.2.10}$$

To solve the partial differential equation, the transient solution will assume the product of a function with dependence on space and a function with dependence on time.

$$w(x,t) = \mathrm{X(x)} * \mathrm{T(t)} \tag{4.2.11}$$

Plugging equation 4.2.11 into equation 4.2.8 and arranging to get similar terms to each side is represented by equation 4.2.12. By setting the terms with space dependency equal to terms with time dependence, both sides must be equal to a constant $-\omega^2$. This form of constant is chosen for simplicity of solution by avoiding trivial solutions.

$$\frac{\mathrm{X}''(x)}{\mathrm{X}(x)} = \frac{1}{D} * \frac{\dot{\mathrm{T}}(\mathrm{t})}{\mathrm{T(t)}} = -\omega^2 \tag{4.2.12}$$

Solving this equation for space first leads to a homogenous ordinary differential equation. The solution to such an equation is shown by 4.2.14.

$$\mathrm{X}'' + \omega^2 \mathrm{X} = 0 \tag{4.2.13}$$

$$\mathrm{X}(x) = \alpha \cos \omega x + \beta \sin \omega x \tag{4.2.14}$$

The boundary conditions of 4.2.9 and 4.2.10 are used to solve for the coefficients α and β. In equation 4.2.16, the coefficient β cannot be solved for and leads to an eigenvalue problem.

$$\mathrm{X}(0) = \alpha \cos 0 + \beta \sin 0 = 0 \tag{4.2.15}$$

$$\mathrm{X}(L) = \beta \sin \omega L = 0 \tag{4.2.16}$$

If β is assumed to be zero, the solution is trivial. Instead, the $\sin \omega L$ must be zero in which the eigenvalue ω is represented by equation 4.2.17.

$$\omega = \frac{n\pi}{L} \tag{4.2.17}$$

The spatial component of the transient solution is left with an unsolved coefficient β and a component n.

$$\mathrm{X}(x) = \beta \sin\frac{n\pi}{L}x \tag{4.2.18}$$

The time component of the transient solution is found by expanding the left-hand side of equation 4.2.12 and solving the separable differential equation as shown in equation 4.2.20.

$$\dot{\mathrm{T}}(\mathrm{t}) = -\omega^2 D * \mathrm{T}(\mathrm{t}) \tag{4.2.19}$$

$$\mathrm{T}(\mathrm{t}) = c * e^{-\omega^2 D * t} \tag{4.2.20}$$

Combining the spatial and temporal components of the transient solution and generalizing by including the summation notation yields equation 4.2.21. The coefficients c and β are combined into coefficient c_β.

$$w(x,t) = \mathrm{X}(\mathrm{x}) * \mathrm{T}(\mathrm{t}) = \sum_{n=1}^{\infty}\left[c_\beta * e^{-\omega^2 D * t} * \sin\frac{n\pi}{L}x\right] \tag{4.2.21}$$

Using the principle of orthogonal functions, the coefficient c_β can be found using equation 4.2.22.

$$c_\beta = \frac{2}{L}\int_0^L w(x,0) * \sin(\omega x)\, dx \tag{4.2.22}$$

The initial condition of the transient solution is given by the relationship between the steady state and general solution. The function for the general solution $\varphi(x,0)$ is known to be zero initially due to the experimental procedure. Water is introduced to the reservoir before fluorescein salt solution resulting in carbon nanotubes full of deionized water. The steady state solution is provided in equation 4.2.7.

$$w(x,0) = \varphi(x,0) - v(x) = 0 - \left(\frac{\varphi_L - \varphi_0}{L} * x + \varphi_0\right) \tag{4.2.23}$$

Integration by parts is used to solve equation 4.2.22 after substitution of initial conditions.

$$c_\beta = \frac{2}{L}\int_0^L \left(\frac{\varphi_0 - \varphi_L}{L} * x - \varphi_0\right) * \sin(\omega x)\, dx = \frac{2}{n\pi}(\varphi_L * \cos(n\pi) - \varphi_0) \qquad (4.2.24)$$

After finding the coefficient c_β, the general solution is given by 4.2.25. The steady state solution is given by a linear relationship of the concentration gradient and the transient solution is the sum of an exponential sinusoidal wave.

$$\varphi(x,t) = \frac{\varphi_L - \varphi_0}{L} * x + \varphi_0 + \sum_{n=1}^{\infty}\left[\frac{2}{n\pi}(\varphi_L * \cos(n\pi) - \varphi_0) * e^{-\left(\frac{n\pi}{L}\right)^2 D*t} * \sin\frac{n\pi}{L}x\right] \quad (4.2.25)$$

Table 2: Coefficients for the estimation of pseudo-steady state diffusion in a singular carbon nanotube.

Coefficient	Units	Value
φ0	[M]	1.00E-05
φl	[M]	0
l	[m]	6.00E-05
D	[m^2/s]	2.86E-10
n	[-]	250

The equation 4.2.25 was implemented into a MATLAB script and used to identify the time needed to reach steady state. Figure 11 shows a three-dimensional plot of the concentration in a carbon nanotube as a function of time and space. The z-axis represents the concentration at a specific point in time. The y-axis shows the concentration throughout the tube length of 60 μm. The x-axis shows the evolution of the concentration profile within the tube as the transient solution dissipates leaving the steady state solution. The plot is used along with a calculation in MATLAB to identify the time to reach steady state.

The time at which the concentration within the reservoir becomes linear with space is deemed as the penetration time of fluorescein salt within the carbon nanotube array. Using MATLAB this time was determined to be 20.45 seconds. This time is sufficiently smaller than the 120-hour time for the reservoirs to reach equilibrium determined by experimentation. This result means that an assumption can be made that the concentration within the carbon nanotubes is linear and the boundary conditions change over a longer period as compared to the time of diffusion within the individual tubes. An approximation of this derivation is given by equation

4.2.26. This approximation is derived from equation 4.2.1 by assuming the concentration profile is linear in both the time and space domain. The penetration time using this calculation was shown to be 12.6 seconds which supports the value identified by the MATLAB solution.

$$t_{penetration} = \frac{l^2}{D} \tag{4.2.26}$$

The simplified calculation can be utilized for a quick solution as needed in section 4.3. However, for detailed analysis of the carbon nanotube system, a better understanding of the penetration behavior of fluorescein may be needed in future studies. As the reservoir volume on either side of the CNT decreases, as in the case of a cell cultured on a bed of CNTs, the penetration time may be in the same range as the total diffusion of the system, rendering the solution of section 4.3 invalid.

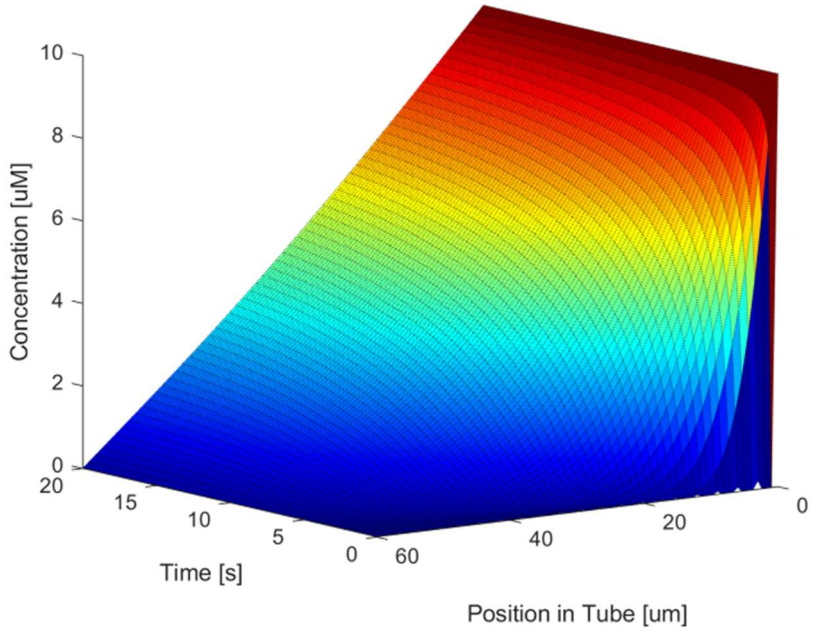

Figure 11: Plot of concentration vs. time vs. position within the length of a singular carbon nanotube. Plot shows the tube reaching pseudo-steady state diffusion at a time of 20.45 seconds.

4.3 Two Large Reservoir Approximation

After finding that the time for fluorescein salt to penetrate the carbon nanotube is sufficiently small, as shown in section 4.2. An estimation of the changing concentration gradient in a "large" reservoir system is of interest to the experimental procedure of this study. The

reservoir volumes (0.4-5 mL) used ranged from $6.25 * 10^{19}$ to $2.65 * 10^{21}$ times the volume of a singular carbon nanotube ($1.54 * 10^{-11}$ mL) analyzed in section 4.2. Such a difference in volume size enables the simplification of Fick's first law for the analysis of the system.

The one-dimensional version of Fick's first law can be described by equation 1. The flux, rate of moving mass per unit area, is represented by J. The flux is related to the diffusivity (D) and the gradient of concentration throughout the tube ($\frac{\partial \varphi}{\partial x}$).

$$J = -D * \frac{\partial \varphi}{\partial x} \tag{4.3.1}$$

By analyzing the membrane as the surface through which the mass is traveling, a relationship between the flow of mass as a function of time and the flux is seen. This molar flux can be alternatively described by equation 4.3.2.

$$J = \frac{1}{A_{CNT}} * \frac{dm_0}{dt} \tag{4.3.2}$$

In equation 4.3.2, m_0 is equivalent to the amount of molecule that crosses the area (A_{CNT}) of interest. The active area of the carbon nanotube array is related to the open pore area throughout the membrane. This area is calculated by finding the average open area of an individual pore and multiplying it by the number of pores estimated from the active area of the reservoir device and the pore density reported by Golshadi et al. [44].

By setting equation 4.3.1 and equation 4.3.2 equal, a dependency between the concentration gradient across the volume of interest and the amount of mass passing through a particular area can be found. Equation 4.3.3 now becomes a partial differential equation with dependencies on x and t.

$$\frac{1}{A_{CNT}} * \frac{dm_0}{dt} = -D * \frac{\partial \varphi}{\partial x} \tag{4.3.3}$$

The mass of reservoir one is equal to the volume of that reservoir times the concentration. Equation 4.3.4 shows how this relationship between mass and concentration puts equation 3 in terms of only concentration. This statement describes how the changing concentration of reservoir 1 relates to the concentration gradient within the carbon nanotubes.

$$\frac{1}{A_{CNT}} * \frac{dm_0}{dt} = \frac{V}{A_{CNT}} * \frac{d\varphi_0}{dt} = -D * \frac{\partial \varphi}{\partial x} \tag{4.3.4}$$

This partial differential equation can be simplified by applying assumptions. In section 4.2, it was shown that the transient solution of the fluorescein penetration of the carbon nanotube resolves in 20.45 seconds. Due to the size of the reservoirs, this transient time is much less than the total time for the two-reservoir system to reach equilibrium. The concentration profile of the carbon nanotube remains in a pseudo-steady state, where the profile is linear, but the boundary conditions change very slowly with time. For systems with reservoir volumes of a similar magnitude to the volume of a singular carbon nanotube, this assumption is not valid.

From these conclusions, it is assumed that the gradient within the carbon nanotube array can be approximated by equation 4.3.5. If the reservoirs are consistently mixed throughout experimentation, the concentrations of each reservoir can be assumed uniform throughout the reservoir. These assumptions lead to the simplification outlined in equation 4.3.5 where the concentration gradient within the carbon nanotube arrays is linear and the reservoir concentrations are assumed uniform throughout the volume.

$$\frac{\partial \varphi}{\partial x} = \frac{\varphi_0 - \varphi_L}{L} \tag{4.3.5}$$

By plugging equation 4.3.5 into equation 4.3.4, the partial differential equation becomes a separable differential equation.

$$\frac{V}{A_{CNT}} * \frac{d\varphi_0}{dt} = D * \frac{\varphi_L - \varphi_0}{L} \tag{4.3.6}$$

Similarly, due to conservation of mass, an expression can be written for the rate of concentration change on the opposite side of the carbon nanotube array. This expression is shown in equation 4.3.7.

$$\frac{V}{A_{CNT}} * \frac{d\varphi_L}{dt} = -D * \frac{\varphi_L - \varphi_0}{L} \tag{4.3.7}$$

Since both φ_0 and φ_L are dependent on time, these two expressions must be subtracted from each other before integration.

$$\frac{V}{A_{CNT}} * \left(\frac{d\varphi_L}{dt} - \frac{d\varphi_0}{dt}\right) = -2 * D * \frac{\varphi_L - \varphi_0}{L} \tag{4.3.8}$$

The separation of variables method begins by moving the variables indicating reservoir concentration to one side and moving the time differential to the opposite side. The left- and right-hand side of equation 4.3.8 can be integrated.

$$\int \frac{1}{\varphi_L - \varphi_0} d(\varphi_L - \varphi_0) = -\int \frac{2 * D * A_{CNT}}{L * V} dt \tag{4.3.9}$$

Equation 4.3.9 can be used to find the diffusivity of the molecule of interest given experimental data for concentration of both reservoirs and properties of the system. Alternatively, if an analytical solution for diffusivity is known (as in section 4.1) equation 4.3.10 can be used to model the changing concentration gradient of the system.

$$-\ln(\varphi_L - \varphi_0) = \frac{2 * D * A_{CNT}}{L * V} * t + C \tag{4.3.10}$$

$$\varphi_L(t) - \varphi_0(t) = e^{\frac{-2*D*A_{CNT}}{L*V}*t+C} = C * e^{\frac{-2*D*A_{CNT}}{L*V}*t} \tag{4.3.11}$$

The time constant of the system (equation 4.3.11) is a good way to estimate the behavior and compare the rate of diffusivity for varying systems. For the carbon nanotube arrays, the time constant is dependent on the diffusivity of the molecule (D), area of the open pores (A_{CNT}), volume of the reservoirs (V), and length of the carbon nanotubes (L).

$$\tau = \frac{L * V}{2 * A_{CNT} * D} \tag{4.3.12}$$

The initial conditions of the system are needed to resolve the coefficient C shown in equation 4.3.11. For a general concentration gradient, the initial concentration at both ends of the carbon nanotube arrays are known. These initial conditions resolve the coefficient to be the gradient between the reservoirs. For the experimental setup of this study, the initial concentration of one reservoir begins at 0 and the second reservoir has concentration φ_{Total}.

$$\varphi_L(0) = \varphi_{Total} \tag{4.3.13}$$

$$\varphi_0(0) = 0 \tag{4.3.14}$$

$$\varphi_L - \varphi_0 = C * e^0 = C = \varphi_{Total} \tag{4.3.15}$$

Two relationships exist to describe dependency of the concentration of reservoir one on reservoir two. The concentration is conserved throughout, meaning additional mass is not added. At any point in time the concentrations of the two reservoirs will add up to the total species concentration in both reservoirs (Equation 4.3.15). The difference in the concentration of the two reservoirs was shown in equation 4.3.11.

$$\varphi_L(t) + \varphi_0(t) = \varphi_{Total} \tag{4.3.16}$$

These relationships are used to produce two equations specifying the changing concentration of each reservoir with only a time dependency.

$$\varphi_0(t) = \varphi_{Total} - \varphi_0(t) + \varphi_{Total} * e^{\frac{-t}{\tau}} \tag{4.3.17}$$

$$\varphi_L(t) = \varphi_{Total} - \varphi_L(t) - \varphi_{Total} * e^{\frac{-t}{\tau}} \tag{4.3.18}$$

Solving for the concentration yields two exponential equations that predict a steady state of equal concentration in both reservoirs. Equations 4.3.19 and 4.3.20 are the culmination of analytical analysis and can be used to compare the experimental results to theoretical information found in the literature.

$$\varphi_0(t) = \frac{\varphi_{Total}}{2} * \left(1 + e^{\frac{-t}{\tau}}\right) \tag{4.3.19}$$

$$\varphi_L(t) = \frac{\varphi_{Total}}{2} * \left(1 - e^{\frac{-t}{\tau}}\right) \tag{4.3.20}$$

These equations were used to understand the effect of changing volume and active diffusion area on the time for the reservoirs to reach equilibrium. Figure 12A shows how increasing the volume of a reservoir from 0.45 mL to 5 mL will increase the time to equilibrium from 48 hours to 600 hours for a system with an active radius of 4 mm. In section 5, reservoirs of various volumes are used to validate this effect and understand the limitations of this model as volume is decreased. Figure 12B indicates that changing the active radius from 4 mm to 1 mm will increase time to equilibrium from 200 hours to 4000 hours. The study by Jensen et al. [28] measured the change in diffusion across nano-porous AAO as this active area was altered.

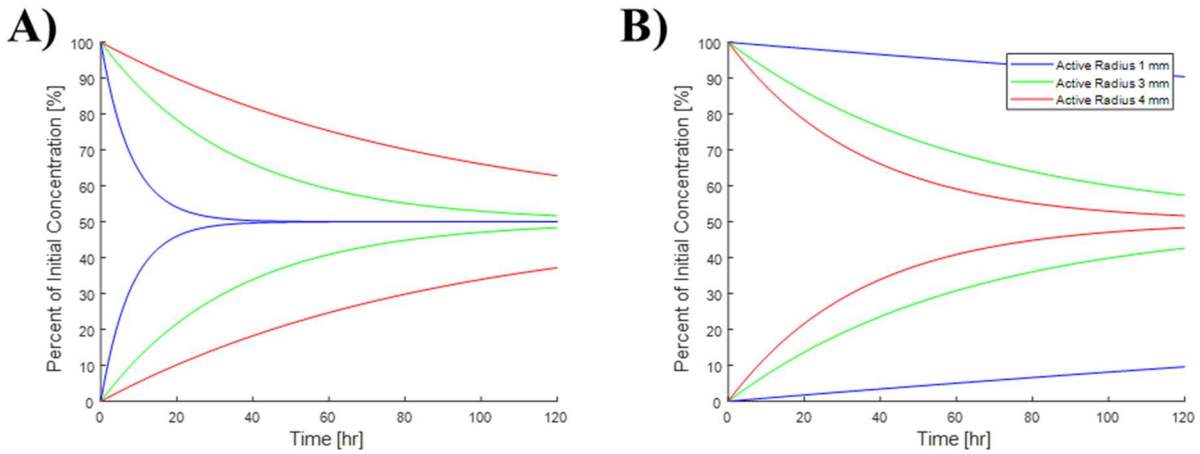

Figure 12: Analysis of system parameters on time to reach equilibrium. **A.)** Reservoir volumes of .45 mL, 2 mL, and 5 mL result in times to reach equilibrium ranging from 48 to 600 hours. **B.)** Active area of the carbon nanotube array of 1mm, 3 mm, and 4mm result in times to reach equilibrium ranging from 200 to 4000 hours.

Table 3 indicates values used in the calculation of equations 4.3.19 and 4.3.20 for a 5 mL volume with active area of 4 mm. These coefficients were used in MATLAB to simulate the changing concentrations of the reservoir system. The exponential curve shown in Figure 12A indicates that five-day experiments will not result in equilibrium within the reservoirs. In section 5, the results of this model are compared with experimental data collected with differing reservoir volume and concentration to test the robustness of the model.

This analytical model for diffusion in a two-reservoir system can be applied when designing drug delivery devices in cell work. The active radius has a drastic effect on the rate of diffusion. By designing reservoirs that fully interface with the CNT array, faster drug delivery can be achieved. Similarly, by decreasing the reservoir size the time to equilibrium will be reduced. However, as seen in section 5, achieving reservoir sizes smaller than 1 mL is difficult while also attempting to maintain active radius.

Table 3: Values for the plotting of changing concentration of a two-reservoir system of volume 5mL and active radius of 4mm.

Coefficient	Units	Value
φ_start	[M]	1.00E-05
L	[m]	6.00E-05
D_eff	[m^2/s]	5.10E-11
ρ_pores	[pores/m^2]	1.16E+13
d_pore	[m]	1.46E-07
d_Active	[m]	4.00E-03
A_CNT	[m^2]	9.13E-06
V	[m^3]	5.00E-06

The analytical models describing the change of concentration as a function of time and positions used in this study to predict the concentration change of fluorescein through a carbon nanotube array separating a two-reservoir system. These models can easily be modified for the development of devices and experiments relating to the molecular transport of any cargo in nano porous material.

5.0 Results and Discussion

Diffusion experiments were conducted using the two-reservoir system separated by a carbon nanotube array to compare the effective diffusivity of fluorescein salt measured experimentally with the diffusivity predicted by the analytical model of section 4. Early experimentation centered around creating a calibration curve and understanding the effect of pH on fluorescent intensity. A large portion of the diffusion experimentation was conducted utilizing 5 mL aluminum reservoirs with no measurement of pH. After redesigning the procedure, 2 mL reservoirs made from polypropylene showed less variability in data trends. Polypropylene reservoirs and pH adjusted solutions provided less variable estimations of diffusivity. Additionally, preliminary tests using 0.4 mL were conducted to test the limits of reducing the volume of the reservoirs. These 0.4 mL reservoirs did not show much diffusion which is attributed to the geometry of the design.

5.1 Dependence of Fluorescein Salt on pH

Fluorescein salt and many other organic molecules have chemical properties that are dependent on environmental factors. Fluorescein salt will change its fluorescent intensity in response to pH change. As a solution becomes more basic, the fluorescent intensity of the solution will increase for a given excitation wavelength [32]. There is a very strong dependency of fluorescence on pH in the range of pH 7. Since the solution used in this study was DI water, the experiments were conducted in the critical range that is sensitive to pH.

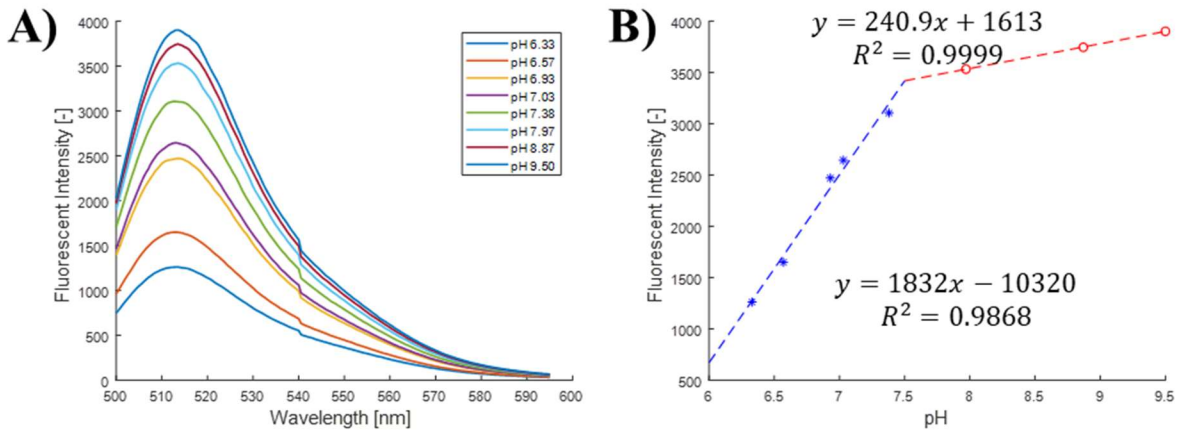

Figure 13: Effect of pH change on a fluorescein salt concentration of 10.01 µM. **A.)** Emission spectra of samples with pH ranging from pH 6.33 to 9.50. **B.)** Peaks of the emission spectra (513.5 nm) plotted against pH.

Using the pH adjustment procedure described in section 3.7, the relationship between pH and fluorescent intensity was characterized. Figure 13 shows the fluorescent spectrum of a solution of 10.01 μM at various pH levels.

The change in fluorescent intensity with respect to change in pH is larger for pH lower than 7.5 and decreases as the pH approaches 10. The decrease of intensity change per pH allows for the use of basic solutions in experimentation. Changes in solution chemistry due to unknown interactions will affect the diffusivity calculation substantially less if pH greater than ~7.5 is used. Drastic and unexpected increases in fluorescent intensity were not seen with larger pH.

For much of the early experimentation, pH was not monitored. The effects of pH change can be seen in the fluorescent intensity of measured fluorescein salt samples. For reservoirs made of aluminum and PLA, large jumps in fluorescent intensity were seen when no additional fluorescein salt was added to the system. The solution became more basic as the fluorescein interacted with the reservoir material. These early pH levels are thought to have started in the range of 6.8 to 7.3 pH where the solution was most sensitive to changes in solution chemistry. Certain trends in the early data are attributed to the use of solution in this pH range and attributes of the system that were unknown prior to experimentation.

An experiment was conducted where two reservoirs were connected without a CNT array separating them. In both reservoirs, a volume of 5 mL of known concentration of fluorescein salt was placed. The fluorescent intensity of the solution at time 0 hours, 24 hours, and 48 hours was measured and is shown in figure 14. By investigating the interaction between fluorescein salt and the aluminum reservoirs, an increase in pH was observed. The increase in fluorescent intensity for the diffusion experiments is attributed to the increase in pH when fluorescein salt interacts with aluminum.

In response to these findings, the switch to polypropylene reservoirs was made. Prior to the switch, many experiments were run with aluminum reservoirs with volumes of 5 mL and 0.4 mL. Though the variance in these experiments is higher than the polypropylene experiments, diffusivities were calculated and compared to expected values.

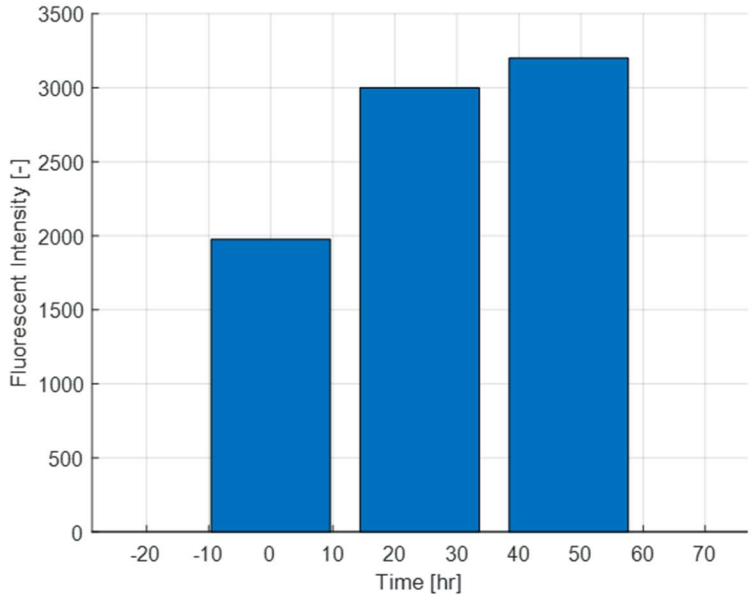

Figure 14: Increase in fluorescent intensity for 10 mL of fluorescein salt in aluminum reservoirs without CNT array for periods of 24 and 48 hours.

After the effects of pH were characterized in figure 13, the monitoring of pH and the chemical interactions of the solution with the system were taken into consideration. To combat pH change, the reservoir material was changed to polypropylene and the solution pH was started at ~7.5 pH instead of 6.8 ph. In section 5.4, experiments without pH control are discussed, such experiments had high variation in the reservoir with high fluorescein salt concentration. In section 5.5, variation in data was reduced by understanding the dependency of fluorescent intensity on pH level.

5.2 Calibration Curve

The fluorescent spectrometer is used to measure the emission spectrum of a solution filled with a fluorescent molecule. The fluorescent spectrum of many molecules predictably scales with an increase in molarity of the solution. Since the units of measure output by the fluorescent spectrometer are in units of fluorescent intensity, a method of relating fluorescent intensity to concentration is needed. Fluorescence has an analytical equation associated with calculating concentration from intensity. However, this relationship is nonlinear and dependent on the device used for measuring fluorescence. By creating a calibration curve experimentally, the concentration regime in which the relationship is linear can be found.

Solutions of known concentration were prepared ranging in molarity from 0.002 mM to 1.5 mM. This range provided solutions that through visual check had a distinct band of fluorescence when exposed to ambient light. These dilutions were inserted into the fluorescent spectrometer and the emission spectrum of each solution was recorded. By extracting the peak of the spectrum using MATLAB, the relationship between concentration and intensity was identified. Figure 15 shows the peak maximums for all dilutions made.

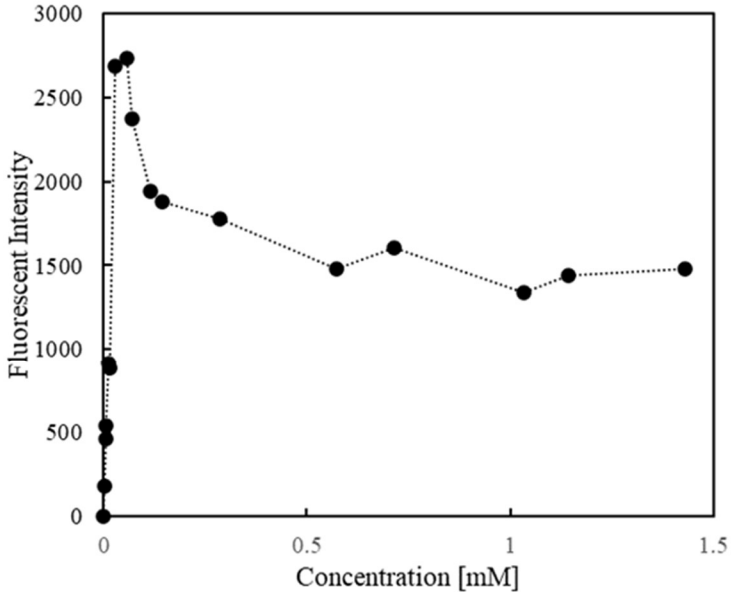

Figure 15: Calibration curve of concentration vs. fluorescent intensity for concentrations rangling from 0 mM to 1.43 mM. The linear relationship breaks down after a concentration of 0.072 mM.

The graph shows that for concentrations greater than 0.072 mM, the nonlinear relationship between intensity and concentration is apparent. The concentration of solutions with high molarity cannot be used without an adjustment in procedure, as the calibration cannot be applied. The full spectra for various points in Figure 15 are shown in Figure 16.

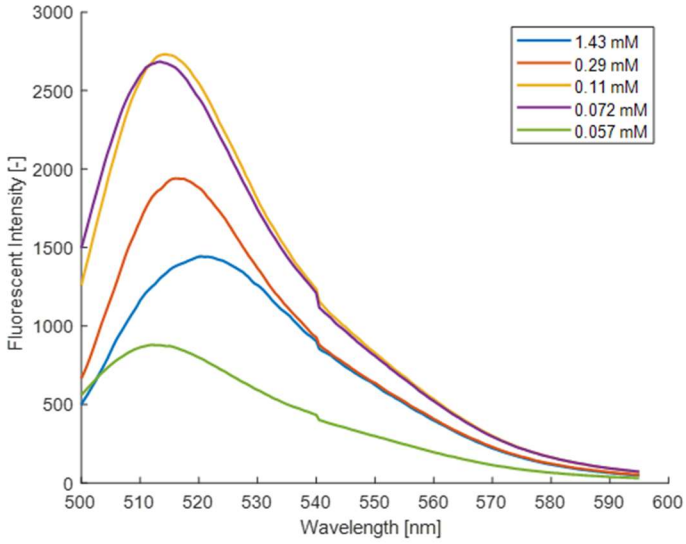

Figure 16: Internal Filtering effect shown in the shifting and decreasing peaks of emission spectra for solutions of increasing concentration.

As concentration increases from 0 M to 0.072 mM, the peaks predictably increase. After 0.072mM, the peak of the spectra begins to shift from 513.5 nm wavelength to a higher wavelength. In addition, the peak begins to decrease with increasing molarity. From the emission spectra the "internal filtering effect" can be seen by the shift in spectrum peak as well as decreasing area under the curve for concentrations greater than 0.072 mM. The "internal filtering effect" occurs when the concentration of fluorescent molecules causes the reabsorption and re-emission of photons decreasing the collection of higher energy light at specific wavelengths. This nonlinear relationship between fluorescent intensity peak and concentration limits the usable range of fluorescein salt concentration to less than 0.072 mM.

For the linear range of 0M to 0.014 mM, the calibration curve for concentration and fluorescent intensity was recreated with greater control and accuracy. A solution of 7 pH was created and predetermined amounts of fluorescein salt were added. Multiple samples were taken from the prepared solutions and measured on the fluorescent spectrometer.

The data taken from five trails was averaged and error bars were added using the standard error calculation in equation 5.2.1.

$$SE = \frac{1}{\sqrt{n}} * \sqrt{\frac{\sum(y - \bar{y})^2}{n - 1}} \tag{5.2.1}$$

A trendline was fit to the data using the Microsoft Excel trendline tool. An R^2 value was calculated using equation 5.2.2 to show goodness of fit for the trendline. For this calculation $Y(t)$ represents a value of the trendline, y_{exp} signifies the experimental data, and $\bar{y}$ is the average of all the experimental data points.

$$R^2 = 1 - \frac{\sum\left(y_{exp} - Y(t)\right)^2}{\sum\left(y_{exp} - \bar{y}\right)^2} \tag{5.2.2}$$

Figure 17 shows the calibration curve with error bars and fitted trendline. This calibration curve was used to convert the fluorescent intensity of samples to concentration values.

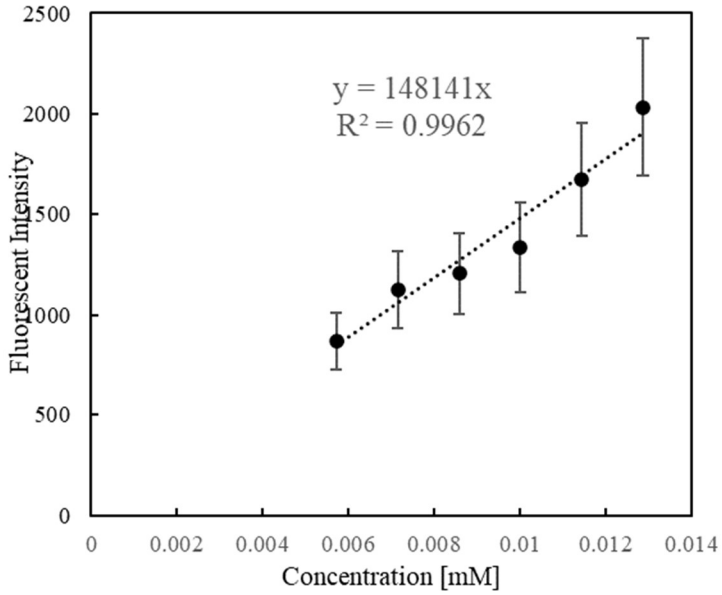

Figure 17: Calibration curve of fluorescent intensity vs. concentration for the linear range of the relationship. The trendline equation is used to find the concentration at timepoints of a diffusion experiment.

5.3 Calculation of Effective Diffusivity

After experimental data was collected, the data from each trial was separated into groups by reservoir size, concentration, and pH. To calculate the effective diffusivity from the experimental data, equations 5.3.1 and 5.3.2 were used. This equation comes from the theoretical

model produced in section 4. The equation provides a relationship between concentration of a reservoir and time.

$$Y(t) = \frac{\varphi_{Start}}{2} * \left(1 - e^{\frac{-t}{\tau}}\right) \tag{5.3.1}$$

$$Y(t) = \frac{\varphi_{Start}}{2} * \left(1 + e^{\frac{-t}{\tau}}\right) \tag{5.3.2}$$

This equation has two variables for which the experimental data must be fit to. Since the starting concentration of the solution is known in most cases, the variable φ_{Start} can be prescribed to the fitting operation. The time constant τ is shown in equation 5.3.3, this value is used to calculate how fast a system will resolve to steady state equilibrium. The time constant relies on the length of the carbon nanotubes (L), volume of the reservoir (V), and area of open tubes (A_{CNT}). The diffusivity of fluorescein salt in the CNT array system is the variable of interest.

$$\tau = \frac{L * V}{2 * A_{CNT} * D} \tag{5.3.3}$$

To find the effective diffusivity of fluorescein salt through the carbon nanotube arrays, a MATLAB script was written. This MATLAB script uses an R^2 calculation shown in equation 5.2.2. In this equation $Y(t)$ represents the value calculated from equation 5.3.1 or 5.3.2 for a given diffusivity based on the reservoir the sample was taken from. Additionally, y_{exp} is the experimental data at a specific time point, and $\bar{y}$ gives the mean of the experimental data. This calculation requires the residual between the experimental data and the fitted line as well as the difference between the experimental value and the mean of the data.

The MATLAB script identifies the diffusivity with the highest R^2 value as the model that represents the experimental data. Diffusivity can be calculated from both the dye filled reservoir and the DI water filled reservoir. The time constant can simultaneously be calculated using this diffusivity value as all other variables of equation 5.3.3 are assumed constant. Experimental values are compared to analytically estimated diffusivities and time constants.

The MATLAB script calculates the R^2 value for diffusivities ranging from 10^{-12} to 10^{-10}. A graph of the R^2 values calculated for data from reservoirs of 5 mL volume, 10 µM concentration, and pH ~7 is shown in Figure 18.

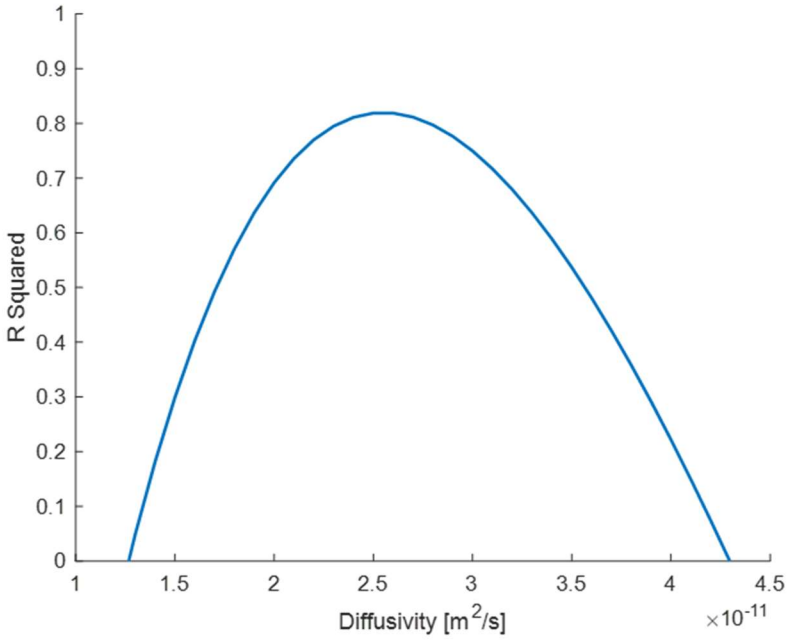

Figure 18: R^2 values for diffusivities fitted to data for seven experiments with 5 mL reservoirs and concentration 10.01 µM.

5.4 Sampling of Aluminum 5 mL reservoirs

Much of the experimentation was conducted using 5 mL aluminum reservoirs manufactured with Designs 2 and 3 of Appendix D. These experiments were used to identify issues with the experimental procedure and understand how concentration gradient impacts the change in concentration across the reservoir system.

Figure 19 shows the data collected from one such experiment where samples were collected from both reservoirs over the course of 5 days. The samples collected at time point 24 hours and 72 hours has a larger fluorescent intensity than the intensity at time 0 hours. After many experiments were run using the aluminum reservoirs, it was thought that evaporation or sampling of the reservoirs was creating an increase in fluorescent intensity. This was caused by an increase of fluorescent intensity at time points taken after the start of the experiment. Since

the concentration of fluorescein salt solution was known prior to experimentation, an increase was not expected.

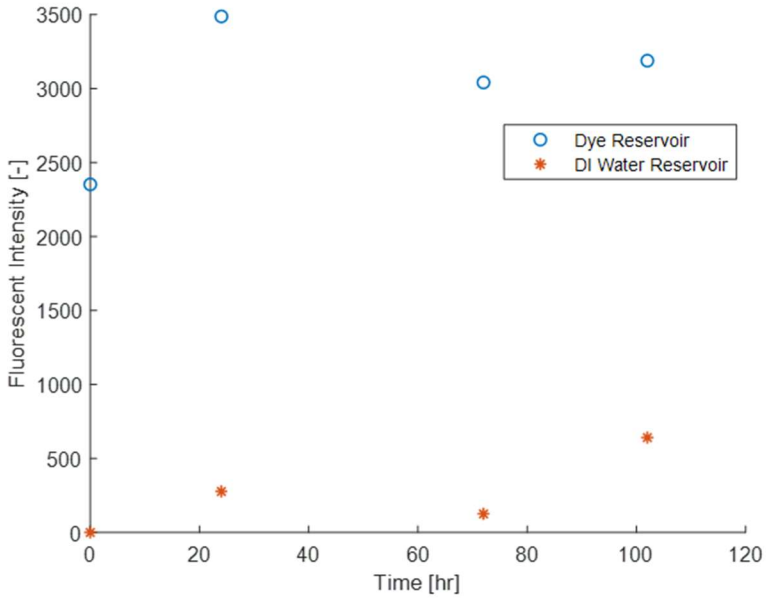

Figure 19: Experimental data collected from 5 mL reservoirs at a concentration of 10.01 µM. The increase in fluorescent intensity due to increasing pH is shown in the jump from 0 hours to 24 hours.

After conducting a review of the literature on fluorescein salt, the pH dependency of fluorescent intensity was discovered [32]. The pH characterization of section 5.1 was developed, and procedural changes were implemented. The chemical interaction between fluorescein salt and the aluminum reservoirs was found to have the biggest contribution to the increase in pH.

Data collected from the reservoir starting with DI water is less variable than the data collected from the reservoir with a high concentration of fluorescein salt. This trend is due to the lower concentration producing less interactions with the reservoir material and having a smaller effect on the pH of that reservoir.

The experiments were grouped by starting concentrations. The data set with concentration of 10.01 µM was the largest as this concentration was used to debug the increasing fluorescent intensity. Experiments were conducted attempting to minimize evaporation and alter sampling rates to mitigate the increasing intensity to no avail. Table 4 details the experiments conducted on the 5 mL reservoirs with different concentrations.

Table 4: Experiments conducted with reservoir volume of 5 mL.

Experiment Name	Volume [mL]	Concentration [uM]	Time [Days]	Active Radius [mm]	PH of DI [pH]	PH of Dye [pH]	Notes
5 mL Al #6	5	7.60	2	7.94			
5 mL Al #7	5	11.44	5	9.53			Accumulation of dye
5 mL Al #9	5	11.44	5	7.94			
5 mL Al #10	5	11.44	5	7.94			Accumulation of Dye
5 mL Al #11	5	100.10	5	7.94			Diluted down to measure samples
5 mL Al #12	5	11.44	5	7.94			Filtered Fluorescein
5 mL Al #13	5	10.01	5	7.94			
5 mL Al #14	5	10.01	5	7.94			Filtered Fluorescein

For experiment 7 and 10 accumulation of fluorescein salt on the aluminum reservoir surface was observed when the systems were deconstructed. In addition to the pH change, these occurrences are thought to cause the high variability in data collected in time points greater than 48 hours. For experiments 12 and 14, a 200 nm syringe filter from Whatman (0992726A) was used to filter out any large particles that could contaminate the experiments. This filtering did not lead to any changes in experimental data.

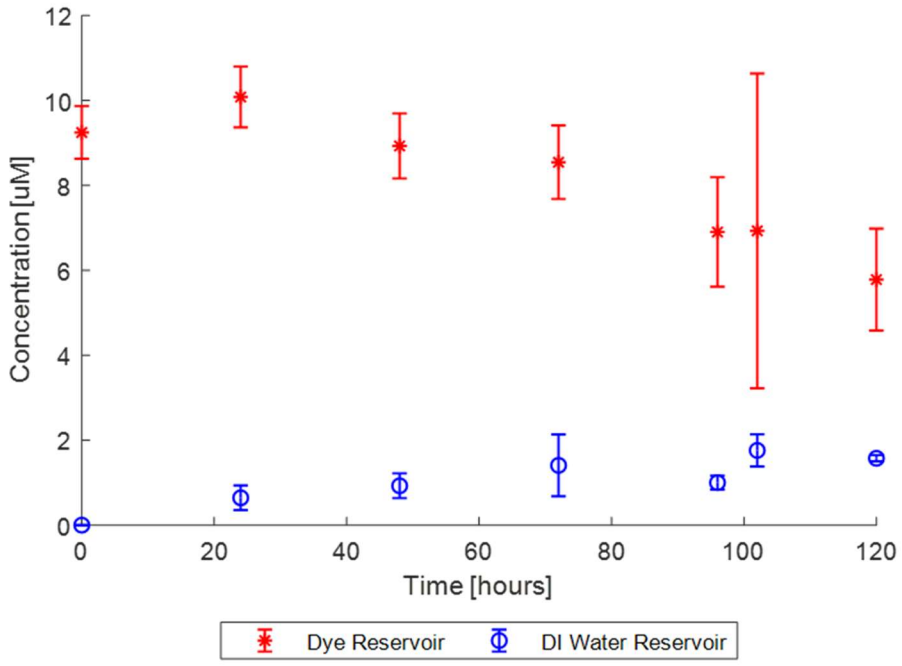

Figure 20: Averaged data for 6 experiments run with 10.01 µM solution in 5 mL reservoirs. Error bars are calculated with standard error equation.

For a concentration of 11.44 and 10.01 µM, the data was averaged, and error bars were added using the standard error equation 5.2.1. Figure 20 shows that for concentration of 11.44 and 10.01 µM, the reservoir starting at high concentration has significantly more variation compared to the reservoir starting with DI water. The dye filled reservoir has high variability in time points after 48 hours due to the collection of fluorescein salt on the reservoir surface.

All data for 5 mL, 2 mL, and 0.4 mL is provided in Appendix F and is organized by reservoir size and starting concentration used.

The diffusivities calculated from experimental data using the MATLAB script of section 5.3 were plotted against the analytical model diffusivity and the sampled data points. Figure 21 shows the data collected for aluminum reservoirs of 5 mL with concentration of 10.01 µM. The trends in the dye reservoir can be seen and are attributed to a lack of pH control. However, for the reservoir that started with an initial concentration of zero, the variance in the data leads to a calculated diffusivity that is very similar to the analytical model.

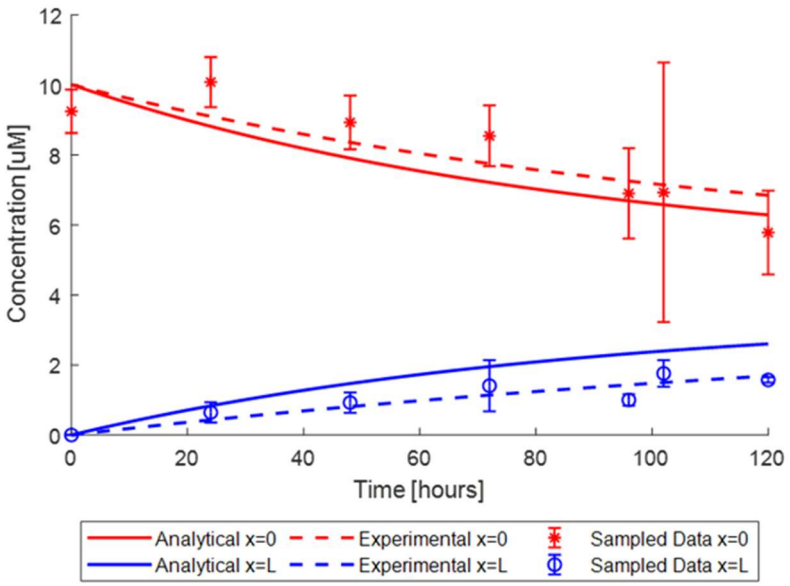

Figure 21: Fitted line, analytical model, and averaged data for experiments of 10.01 µM and 5 mL volume. Error bars are calculated with standard error.

Figure 22 shows the analytical and experimental models for the 5 mL reservoirs at a concentration of 100.1 µM. As the model predicts, a change in concentration does not affect the diffusivity of the system. The diffusivity calculated was faster by a factor of 1.5. Since these numbers were measured with aluminum reservoirs, this increase in diffusivity can only be compared qualitatively as the pH of the system was unknown.

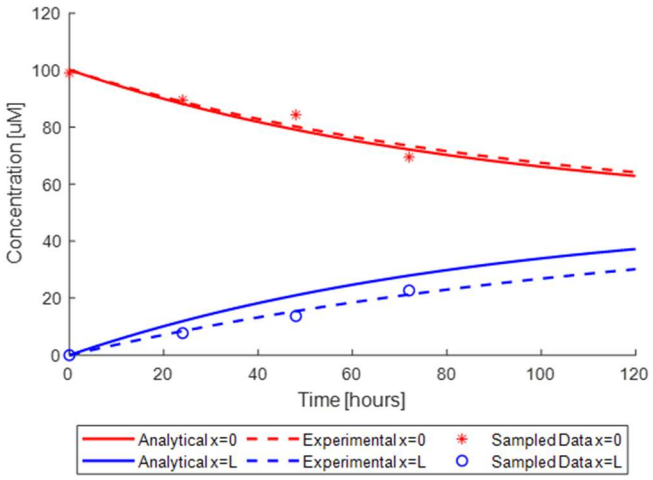

Figure 22: Fitted line, analytical model, and sampled data for experiments of 100.1 µM and 5 mL volume.

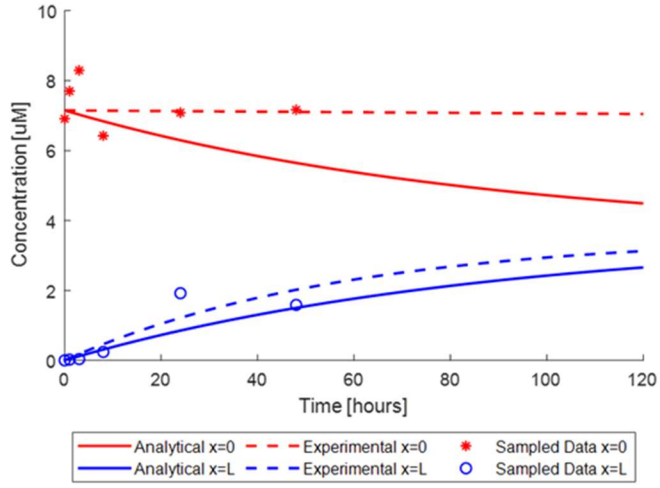

Figure 23: Fitted line, analytical model, and sampled data for experiments of 7.60 µM and 5 mL volume.

Since the fluorescence of samples with concentration greater than 72 µM could not be measured on the fluorometer, the samples were diluted to a concentration of 10% and fluorescent intensities were correlated to concentrations 10 times greater than the concentration given by the calibration curve.

Figure 23 shows data collected from a starting concentration of 7.6 µM. This was an early experiment where many samples were taken before the time point of 24 hours. Sampling rates of less than 24 hours contributed to high levels of interaction with the aluminum reservoirs as seen in the figure.

Table 5 provides the time constants and diffusivities measured from experimental datasets. The diffusivity from concentration of 7.60 µM in the dye reservoir was much smaller than the analytical model due to drastic pH change. All other diffusivities are between a factor of 0.72 and 2.28 times off from the analytically estimated diffusivity.

Table 5: Experimental diffusivities and time constants calculated for 5 mL datasets. Diffusivity is calculated for both the dye and DI water reservoirs.

Reservoir Size [mL]	Reservoir Type [-]	pH Value [pH]	Concentration [µM]	Time Constant [s]	Calculated Diffusivity [m^2/s]	Ratio of Analytical to Experimental [-]
5	DI	~7	10.01	6.57E+05	2.50E-11	2.28
5	Dye	~7	10.01	4.32E+05	3.80E-11	1.50
5	DI	~7	100.10	4.68E+05	3.51E-11	1.63
5	Dye	~7	100.10	3.42E+05	4.81E-11	1.19
5	DI	~7	7.60	2.08E+05	7.91E-11	0.72
5	Dye	~7	7.60	1.49E+07	1.10E-12	51.91

*Analytical diffusivity assumed $5.17 * 10^{-11}\ \frac{m^2}{s}$

5.5 Sampling of Polypropylene 2 mL reservoirs

Experiments with polypropylene were initiated due to the chemical inertness of this plastic compared with that of aluminum and 3D printed PLA. The design considerations of polypropylene are further discussed in section 3.8. Experiments with polypropylene saw a reduction in chemical interaction between the fluorescein salt solution and reservoir system. Specifically, fluorescein salt surface build-up and pH increase were mitigated by the switch away from aluminum reservoirs.

Two sets of reservoirs were made with volume of 2 mL. The volume of 2 mL was chosen to compare to the results of the 5 mL aluminum reservoirs and examine the impact of a smaller volume. Experiments with the 2 mL reservoir consisted of taking two samples at time points

separated by 24 hours increments. Table 6 lists all experiments ran with parameters including concentration and reservoir size.

Table 6: Experiments conducted with reservoir volume of 2 mL.

Experiment Name	Volume [mL]	Concentration [uM]	Time [Days]	Active Radius [mm]	PH of DI [pH]	PH of Dye [pH]
2 mL Poly #1	2	10.01	2	7.94	7.0	7.0
2 mL Poly #2	2	4.29	3	7.94	7.6	7.6
2 mL Poly #3	2	4.29	2	7.94	7.4	7.4
2 mL Poly #4	2	4.29	3	7.94	7.4	7.4

Figure 24 shows the data collected from an experiment using this reservoir at a starting concentration of 10.01 µM. Figure 24C shows the fluorescein salt concentration reading did not exceed initial concentration due to increasing pH. Figure 24A and 24B display the typical spectra collected for each experiment. Due to the smaller reservoir size of 2 mL, less samples could be extracted from each experiment resulting in a lower throughput of data points.

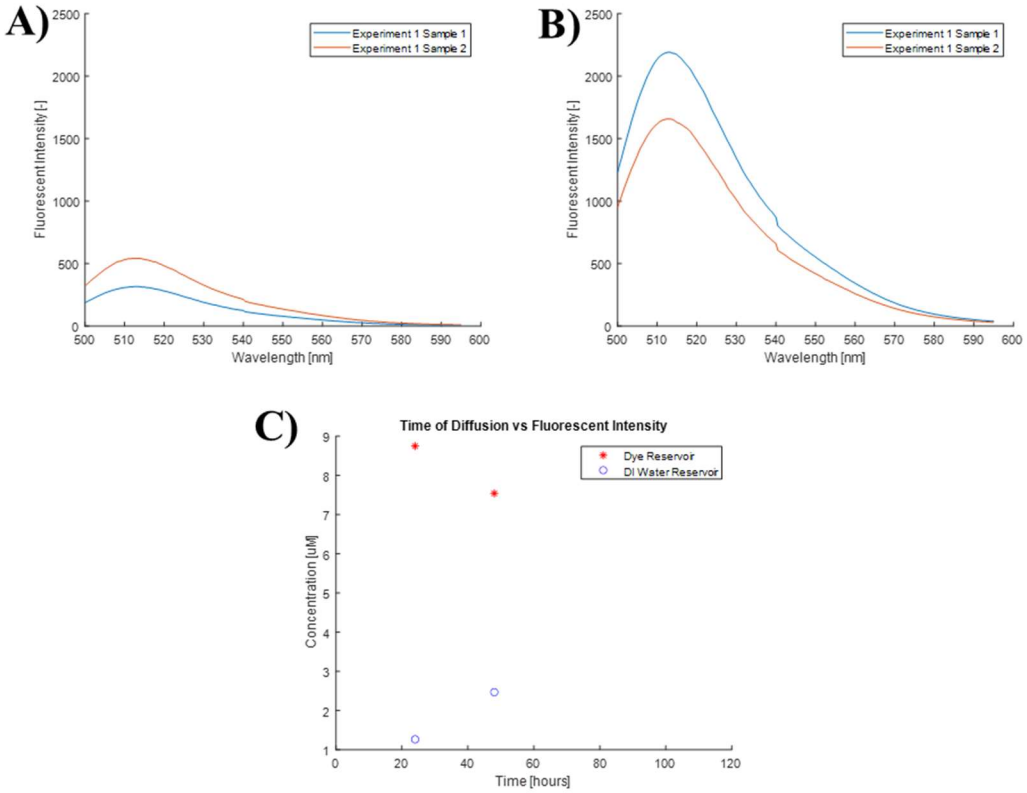

Figure 24: Example experiment for 2 mL reservoirs. **A.)** Peaks of emission spectra for both reservoirs at 24-hour intervals. **B.)** Emission spectra for fluorescein salt filled reservoir. **C.)** Emission spectra for DI water filled reservoirs.

The polypropylene reservoirs offered a much more consistent measurement of diffusivity. The exponential shape of the 2 mL datasets matched the trends predicted by the analytical model. Figures 25 and 26 provide plots of experiments ran with concentrations of 10.01 µM and 4.29 µM concentrations, respectively.

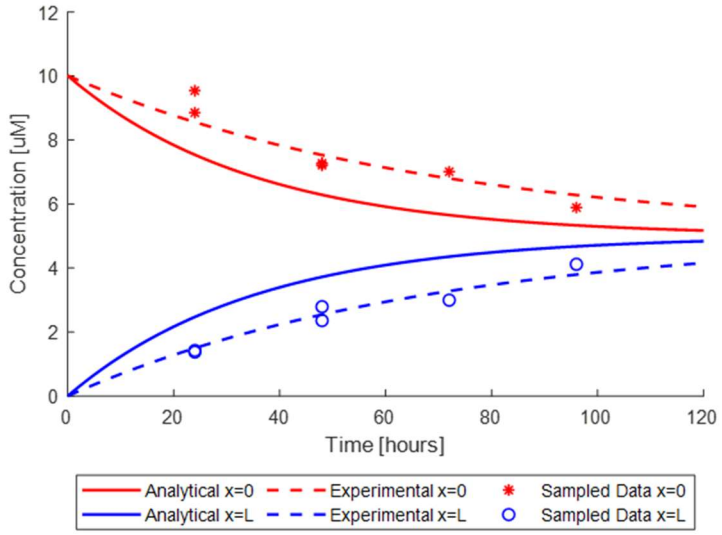

Figure 25: Fitted line, analytical model, and sampled data for experiments of 10.01 µM and 2 mL volume.

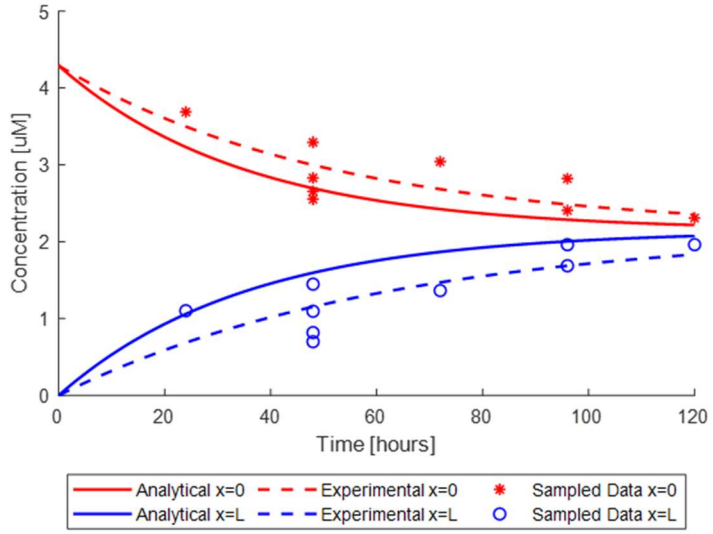

Figure 26: Fitted line, analytical model, and sampled data for experiments of 4.29 µM and 2 mL volume.

Table 7 summarizes the diffusivities and time constants calculated from all datasets. The rate of diffusion in the 2 mL reservoirs is in the same regime as that predicted by the analytical model with all diffusivities roughly 2 times smaller than the analytical model diffusivity. This signifies a larger time to reach equilibrium. The switch to polypropylene reservoirs improved the consistency of data collected.

Table 7: Experimental diffusivities and time constants calculated for 2 mL datasets. Diffusivity is calculated for both the dye and DI water reservoirs.

Reservoir Size [mL]	Reservoir Type [-]	pH Value [pH]	Concentration [μM]	Time Constant [s]	Calculated Diffusivity [m^2/s]	Ratio of Analytical to Experimental [-]
2	DI	7	10.01	2.45E+05	2.68E-11	2.13
2	Dye	7	10.01	2.57E+05	2.56E-11	2.23
2	DI	7.5	4.29	2.24E+05	2.93E-11	1.95
2	Dye	7.5	4.29	1.87E+05	3.51E-11	1.63

*Analytical diffusivity assumed $5.17 * 10^{-11}\ \frac{m^2}{s}$

5.6 Sampling of Aluminum and Polypropylene 0.4 mL reservoirs

In tandem with the experiments ran with the 5 mL aluminum reservoirs and the 2 mL polypropylene reservoirs, experiments were conducted using reservoirs of 0.4 mL. Sets of both aluminum and polypropylene reservoirs were manufactured.

Like the 5 mL and 2 mL reservoirs, many trials at varying concentrations were conducted. The experiments ran with 0.4 mL reservoirs are detailed in Table 8.

Table 8: Experiments conducted with reservoir volume of 0.4 mL.

Experiment Name	Volume [mL]	Concentration [uM]	Time [Days]	Active Radius [mm]	PH of DI [pH]	PH of Dye [pH]	Notes
0.4 mL Al #1	0.4	10.01	1	7.94			Filtered Fluorescein
0.4 mL Al #2	0.4	10.01	1	7.94			Filtered Fluorescein
0.4 mL Al #3	0.4	10.01	2	7.94			
0.4 mL Al #4	0.4	10.01	2	7.94			
0.4 mL Al #5	0.4	4.29	1	7.94	7.4	7.4	
0.4 mL Al #6	0.4	4.29	2	7.94	7.4	7.4	
0.4 mL Poly #1	0.4	4.29	2	7.94	7.6	7.6	
0.4 mL Poly #2	0.4	4.29	3	7.94	7.6	7.6	
0.4 mL Poly #3	0.4	4.29	1	7.94	7.4	7.4	
0.4 mL Poly #4	0.4	4.29	2	7.94	7.4	7.4	

The experiments were split into two datasets of 10.01 μM and 4.29 μM. Similar data was collected for the aluminum and polypropylene reservoirs, so experiments were not separated by reservoir material unlike the reservoirs of 5 mL and 2 mL.

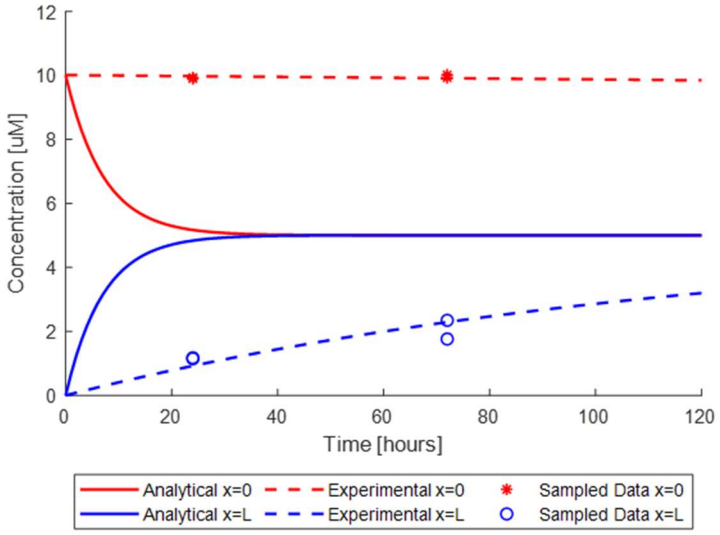

Figure 27: Fitted line, analytical model, and sampled data for experiments of 10.01 µM and 0.4 mL volume.

Figure 27 shows data collected with only aluminum reservoirs at a concentration of 10.01 µM. It is thought that the smaller reservoir volume greatly impacts the increase of pH leading to the very high concentrations measured at all data points.

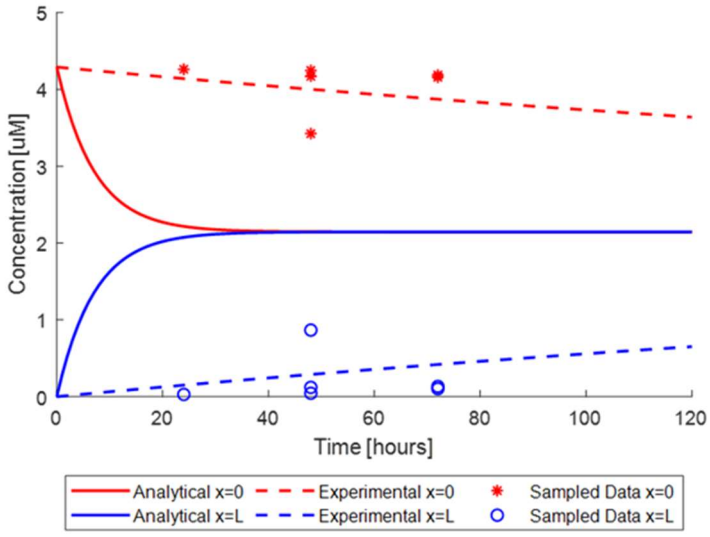

Figure 28: Fitted line, analytical model, and sampled data for experiments of 4.29 µM and 0.4 mL volume.

Figure 28 shows data collected with polypropylene and aluminum reservoirs with a concentration of 4.29 µM. The pH of solution was measured to be ~7.5 for all experiments. This pH reduced how the chemical interaction between fluorescein and the reservoir material affected the fluorescent intensity of the samples.

Both figures show the unexpectedly slow diffusion for all experiments conducted with 0.4 mL reservoirs. Table 9 summarizes the diffusivities and time constants calculated from each dataset. The diffusivities are greater than 18 times smaller than the diffusivity estimated by the analytical model.

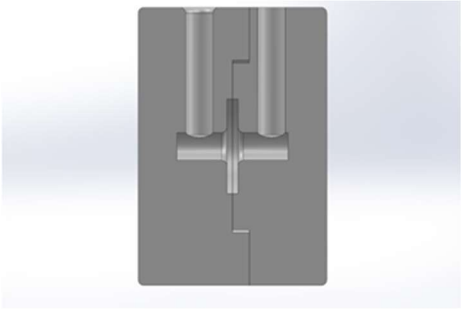

Figure 29: Small geometric features of the 0.4 mL device shown. Features are thought to contribute to the slow diffusion of fluorescein salt.

The cause of this slow diffusion is thought to be caused by geometric limitations imposed by the smaller reservoirs. Figure 29 shows the small 5 mm diameter cylindrical reservoir attached to a 17 mm diameter hole meant to provide clearance to the CNT array. The combination of these two different sized holes may be creating air pockets that will not allow for fluorescein solution to properly interact with the CNT array.

Table 9: Experimental diffusivities and time constants calculated for 0.4 mL datasets. Diffusivity is calculated for both the dye and DI water reservoirs.

Reservoir Size [mL]	Reservoir Type [-]	pH Value [pH]	Concentration [µM]	Time Constant [s]	Calculated Diffusivity [m^2/s]	Ratio of Analytical to Experimental [-]
0.4	DI	~7	10.01	4.24E+05	3.10E-12	18.42
0.4	Dye	~7	10.01	1.31E+07	1.00E-13	571.00
0.4	DI	7.5	4.29	1.19E+06	1.10E-12	51.91
0.4	Dye	7.5	4.29	1.19E+06	1.10E-12	51.91

*Analytical diffusivity assumed $5.17 * 10^{-11}\ \frac{m^2}{s}$

5.7 Discussion

Using the diffusivities calculated from the experimental data, the validity of the analytical model can be analyzed. Tables 5, 7, and 9 detail the experimental diffusivities calculated from each dataset in section 5.4, 5.5, and 5.6. A ratio of diffusivity estimated from the analytical model to the diffusivity calculated from the experimental data provides a metric for how well the analytical model matched. Time constants were additionally calculated to analyze how changing the reservoir size impacted the time for the system to reach equilibrium.

For reservoir volumes of 5 mL, the diffusivity measured experimentally agrees well with the diffusivity estimated from theory. The analytically estimated diffusivity ranges between a factor of 0.72 to 2.28 times larger than the experimental diffusivity. The only exception being the dye reservoir of concentration 7.60 μM where excessive pH change was noted in Figure 22.

The data collected with the 5 mL aluminum reservoirs informed many of the design alterations of the two-reservoir device detailed in Appendix D. The interaction between fluorescein salt and the aluminum reservoirs is apparent in the increase of fluorescent intensity in experiments where no additional fluorescein salt was added.

For reservoir volumes of 2 mL, all data sets contained diffusivities that were within a reasonable range of the analytical model. The ratio of analytical to experimental diffusivity ranged from 1.63 to 2.23. The measurements of both the dye and DI reservoirs provided very good consistency. This is attributed to the control of pH and the switch from aluminum to polypropylene.

When altering the initial concentration of the solution from 7.6 to 100.1 μM for 5 mL and 4.29 to 10.01 μM for 2 mL, the change in diffusivity and time constants were not significantly impacted. For 5 mL the time constants ranged from $2.08 * 10^5\ s$ to $6.57 * 10^5 s$, this range can be attributed to the lack of control on pH rather than the changing concentration gradient. Time constants were measured between $2.56 * 10^5 s$ and $3.51 * 10^5 s$ for reservoirs of 2 mL volume. The consistency in time constant for 2 mL demonstrates the lack of effect the initial concentration gradient has on the time to reach system equilibrium. This result agrees with the analytical model showing that the time constant is not affected by changing the starting concentration gradient in equation 4.3.12.

The diffusivity of the 0.4 mL reservoirs is slower than predicted by the analytical model. Such a reservoir size should have faster diffusion than the 2 mL reservoirs based on the analytical model. One potential cause for the slower diffusion is the design and fabrication of the 0.4 mL reservoirs. When running experiments with the 0.4 mL reservoirs, adding the solution to the reservoir resulted in pockets of air that had to be removed to add the full 0.4 mL. The narrow cylindrical design could limit the interaction between the CNT array and the fluorescein solution. The design includes a recessed hole thought to resolve this design feature. However, by redesigning the 0.4 mL reservoir to have a larger radius and shorter depth, insight into the slow diffusion could be gained. The diffusivity calculated from these reservoirs must be further studied with newly manufactured reservoirs.

It was expected that the experimentally measured diffusivities for all volumes would match the analytically calculated diffusivities. This is based on the model developed in section 4.1 where diffusivity is not subject to any of the system parameters. Rather, the diffusivity is dependent on the properties of the carbon nanotube array and the molecule used. Diffusivities measured with both 5 mL and 2 mL reservoirs are roughly 2 times smaller than the analytical model. Procedural error and validity of the values used for the analytical model are potential sources of error leading to this discrepancy. Further experiments for the measurement of system dimensions and the use of tools with higher accuracy would provide confidence in experimentation and theory.

Specifically, confidence in the diffusivities measured from experiment would be improved with stricter control of dimensions and more accurate measurement of system parameters. These parameters include active radius, reservoir volume, AAO pore density, and CNT diameter. Active radius (see Figure 8) is affected by variation in hole alignment and hole size which would alter the diffusion between experiments. For an active radius of 3 mm caused by potential misalignment of the vinyl contact paper, the time constant estimated by the analytical model for a 2 mL reservoir is $2.05 * 10^5 s$. This value agrees with the time constants of $2.04 * 10^5 s$ and $2.63 * 10^5 s$ calculated experimentally.

Similarly, pore diameter has an accuracy of ±42 nm taken from publications by the NBIL [27]. This uncertainty results in a porosity ranging from 0.09 to 0.30 with a nominal value of 0.18 that was used for the analytical model. This range results in an analytical diffusivity

between $2.65 * 10^{-11}\ \frac{m^2}{s}$ and $8.59 * 10^{-11}\ \frac{m^2}{s}$ with the nominal value of $5.17 * 10^{-11}\ \frac{m^2}{s}$ used in analysis. Such a range results in an analytical diffusivity 1.33 to 4.31 times greater than the smallest experimental diffusivity measured from data of 2 mL reservoirs. A verification and study of the CNT array properties would inform the validity of the analytical model.

Additionally, the analytical model can be further developed to incorporate properties of the CNT array such as tortuosity that were assumed to have a negligible effect on the system. The assumption that the reservoirs are well mixed is dependent on the sampling rate and mixing procedure. This assumption would alter the boundary conditions described in section 4.3. Lack of mixing in the reservoirs would lead to a slower time to equilibrium as a concentration gradient would exist in each large reservoir.

The experimental procedure and analytical model developed provide reasonable agreement for the calculation of diffusivity and time constant for volumes of 2 mL and 5 mL. Study into the parameters of the two-reservoir system is needed to mitigate the variance in experimentally measured values and provide confidence in the analytical model.

6.0 Conclusions

6.1 Utility of Measured Diffusion of Fluorescein Salt

The result of this work is an experimental study that informs an analytical model. This analytical model provides a reasonable estimation of the diffusivity of small molecules that are passively transported through an array of nanotubes. The analytical model leverages the Stokes-Einstein equation and a simplified derivation of Fick's laws to model the change in concentration through a two-reservoir system with volume significantly larger than the carbon nanotube volume through which molecules are traveling.

Experiments were conducted with fluorescein salt due to the ability to relate fluorescent intensity of a solution to the concentration of that solution. An FP-8500 fluorescent spectroscopy tool was used to measure the fluorescent intensity of samples collected at various time points from both reservoirs separated by an array of carbon nanotubes. Fluorescein salt showed high sensitivity to concentration and pH level resulting in unexpected trends found in experiments with minimal control on such parameters. Polypropylene reservoir devices with solutions of ~7.5 pH and ~10 μM provided the optimal conditions for measuring the diffusivity. Diffusivities ranged from $2.56 * 10^{-11}\ \frac{m^2}{s}$ to $3.51 * 10^{-11}\ \frac{m^2}{s}$ and $2.5 * 10^{-11}\ \frac{m^2}{s}$ to $7.91 * 10^{-11}\ \frac{m^2}{s}$ for reservoirs of 2 mL and 5 mL volumes respectively.

6.2 Application of Results

The carbon nanotube arrays are designed for use in cell culture applications. In biology and chemistry research, the passive transfection of drugs into cells is currently an inefficient process with high cytotoxicity. Carbon nanotubes offer an inexpensive alternative to standard transfection technologies with improved efficiency and less toxicity [1]. The transfection of small organic molecules like that of fluorescein salt is commonplace in pharmaceutical research. The analytical model developed in this work can be applied to small molecules the size magnitude of fluorescein salt. The analytical model was confirmed by experimental data for solution sizes of 2-5 mL and concentrations ranging from 4-100 μM.

In addition, a procedure was developed for the monitoring of concentration change in a two-reservoir system with a fluorescent solution. Specifically, a method of handling planar arrays of vertically aligned nanostructures was developed using vinyl contact paper. The vinyl contact

paper created a surface for a water-tight seal that mitigated occurrences of micro cracking. An experimental device sealed this nanostructure in a two-reservoir system designed to interact with various configurations of a fluorescent spectroscopy tool. The study of other nanostructures and porous media can be implemented into the reservoir design to understand diffusivity.

6.3 Considerations for Future Work

To expand the applicability of the analytical model, the type and size of the molecules studied should be diverse. Understanding the role of charge and chemical properties is important to elucidate the interactions between solutions and the transfection device. The Jasco FP-8500 tool used provided a robust measurement of concentration from fluorescent intensity. However, sampling of reservoirs created a cumbersome procedure that limited the throughput of experiments. In initial experimentation, an optical table was used to take measurements without sampling. A tool like the optical table would speed up the experimental procedure. Additionally, A switch from measuring fluorescence to measuring absorbance would provide flexibility in choosing molecules to study. Tools like a microplate reader spectrophotometer or a nanodrop spectrophotometer would be suitable for the procedure developed. Such a change would broaden the applications of the method and increase understanding of cellular transfection.

By studying proteins and plasmid DNA diffusing across the CNT arrays, the application of CNTs in biological research can be understood. The ability to predict the time of diffusion of biologically relevant cargo across this device would qualify this transfection technology for use in research. The analytical model could be expanded to include larger cargo and the limits of the theory can be tested. Once diffusion through aligned carbon nanotubes is understood, cells can be cultured on one side of the CNT array while samples are collected from a reservoir. Such a study would be aimed at comparing the transport mechanisms of transfection to diffusion. Cellular transfection could introduce additional transport mechanisms that speed up or slow down the diffusion of molecules.

References

[1] Golshadi, M., Wright, L. K., Dickerson, I. M., and Schrlau, M. G., 2016, "High-Efficiency Gene Transfection of Cells through Carbon Nanotube Arrays," Small, **12**(22), pp. 3014–3020.

[2] Iijima, S., 1991, "Helical Microtubules of Graphitic Carbon," Nature, **354**(6348), pp. 56–58.

[3] Iijima, S., and Ichihashi, T., 1993, "Single-Shell Carbon Nanotubes of 1-Nm Diameter," Nature, **363**(6430), pp. 603–605.

[4] Lee, C., Wei, X., Kysar, J. W., and Hone, J., 2008, "Measurement of the Elastic Properties and Intrinsic Strength of Monolayer Graphene," Science (1979), **321**(5887), pp. 385–388.

[5] Dalton, A. B., Collins, S., Muñoz, E., Razal, J. M., Ebron, V. H., Ferraris, J. P., Coleman, J. N., Kim, B. G., and Baughman, R. H., 2003, "Super-Tough Carbon-Nanotube Fibres," Nature, **423**(6941), p. 703.

[6] Cao, Q., Han, S. J., Tulevski, G. S., Zhu, Y., Lu, D. D., and Haensch, W., 2013, "Arrays of Single-Walled Carbon Nanotubes with Full Surface Coverage for High-Performance Electronics," Nat Nanotechnol, **8**(3), pp. 180–186.

[7] Smart, S. K., Cassady, A. I., Lu, G. Q., and Martin, D. J., 2006, "The Biocompatibility of Carbon Nanotubes," Carbon N Y, **44**(6), pp. 1034–1047.

[8] Journet, C., Maser, W. K., Bernier, P., Loiseau, A., de la Chapelle, M. L., Lefrant, S., Deniard, P., Lee, R., and Fischer, J. E., 1997, "Large-Scale Production of Single-Walled Carbon Nanotubes by the Electric-Arc Technique," Nature, **388**(6644), pp. 756–758.

[9] Guo, T., Nikolaev, P., Thess, A., Colbert, D. T., and Smalley, R. E., 1995, "Catalytic Growth of Single-Walled Manotubes by Laser Vaporization," Chem Phys Lett, **243**(1), pp. 49–54.

[10] Bronikowski, M. J., Willis, P. A., Colbert, D. T., Smith, K. A., and Smalley, R. E., 2001, "Gas-Phase Production of Carbon Single-Walled Nanotubes from Carbon Monoxide via

the HiPco Process: A Parametric Study," Journal of Vacuum Science & Technology A: Vacuum, Surfaces, and Films, **19**(4), pp. 1800–1805.

[11] Golshadi, M., Maita, J., Lanza, D., Zeiger, M., Presser, V., and Schrlau, M. G., 2014, "Effects of Synthesis Parameters on Carbon Nanotubes Manufactured by Template-Based Chemical Vapor Deposition," Carbon N Y, **80**(1), pp. 28–39.

[12] Chen, J., Wang, W., and Zhang, S., 2020, "Tribological Properties of Vertically Aligned Carbon Nanotube Arrays and Carbon Nanotube Sponge," AIP Adv, **10**(12), p. 125209.

[13] Scheibel, O. V, Lanza, D., and Schrlau, M. G., 2017, *Template-Based Synthesis of Integrated Carbon Micro- and Nanostructures*.

[14] Vahedein, Y. S., and Schrlau, M. G., 2015, *Numerical Model of Template-Based Chemical Vapor Deposition Processes to Manufacture Carbon Nanotubes for Biological Devices*.

[15] Vahedein, Y. S., and Schrlau, M. G., 2016, "Numerical Investigation of Thermofluid Flow in a Chemical Vapor Deposition Furnace Utilized to Manufacture Template-Synthesized Carbon Nanotubes," J Heat Transfer, **138**(10).

[16] Schrlau, M. G., Falls, E. M., Ziober, B. L., and Bau, H. H., 2008, "Carbon Nanopipettes for Cell Probes and Intracellular Injection," Nanotechnology, **19**(1), p. 015101.

[17] Arowosola, A., Fujimoto, A., Scheibel, O., and Schrlau, M. G., 2015, *Fabrication of Theta Carbon Nanopipettes Using a Template-Based Chemical Vapor Deposition Nanomanufacturing Process*.

[18] Anzar, N., Hasan, R., Tyagi, M., Yadav, N., and Narang, J., 2020, "Carbon Nanotube - A Review on Synthesis, Properties and Plethora of Applications in the Field of Biomedical Science," Sensors International, **1**.

[19] Scheibel, O. V., and Schrlau, M. G., 2020, "A Self-Contained Two-Electrode Nanosensor for Electrochemical Analysis in Aqueous Microenvironments," Electroanalysis, **32**(9), pp. 1914–1921.

[20] Golshadi, M., and Schrlau, M. G., 2013, “Template-Based Synthesis of Aligned Carbon Nanotube Arrays for Microfluidic and Nanofluidic Applications,” ECS Trans, **50**(33), pp. 1–14.

[21] Bau, H. H., Sinha, S., Kim, B., and Riegelman, M., 2005, “Fabrication of Nanofluidic Devices and the Study of Fluid Transport through Them,” *Nanofabrication: Technologies, Devices, and Applications*, SPIE, p. 201.

[22] Majumder, M., Chopra, N., Andrews, R., and Hinds, B. J., 2005, “Nanoscale Hydrodynamics: Enhanced Flow in Carbon Nanotubes,” Nature, **438**(7064), p. 44.

[23] Whitby, M., Cagnon, L., Thanou, M., and Quirke, N., 2008, “Enhanced Fluid Flow through Nanoscale Carbon Pipes,” Nano Lett, **8**(9), pp. 2632–2637.

[24] Thomas, J. A., and McGaughey, A. J. H., 2008, “Reassessing Fast Water Transport through Carbon Nanotubes.,” Nano Lett, **8**(9), pp. 2788–2793.

[25] Thomas, J. A., McGaughey, A. J. H., and Kuter-Arnebeck, O., 2010, “Pressure-Driven Water Flow through Carbon Nanotubes: Insights from Molecular Dynamics Simulation,” International Journal of Thermal Sciences, **49**(2), pp. 281–289.

[26] Xu, X., Zhao, Y., Wang, J., Zhang, N., Wang, C., Zhang, J., and Wei, N., 2020, “Water Flow inside Various Geometric Nano-Confinement Channels,” Physical Chemistry Chemical Physics, **22**(42), pp. 24633–24639.

[27] Golshadi, M., and Schrlau, M. G., 2013, “Template-Based Synthesis of Aligned Carbon Nanotube Arrays for Microfluidic and Nanofluidic Applications,” ECS Trans, **50**(33), pp. 1–14.

[28] Jensen, A., and Schrlau, M. G., 2017, *Observing Fluid Flow Through Carbon Nanotube Arrays and Nanoporous Membranes*.

[29] Emery, T., Jensen, A., Kubrin, K., and Schrlau, M., 2017, *Facilitating Fluid Flow Through Carbon Nanotube Arrays Using 3D Printing*.

[30] National Center for Biotechnology Information, 2023, “PubChem Compound Summary for CID 10608, Fluorescein Sodium.”

[31] ThermoFisher Scientific, “ThermoFisher Scientific SpectraViewer” [Online]. Available: https://www.thermofisher.com/order/fluorescence-spectraviewer#!/. [Accessed: 13-Mar-2023].

[32] Sjöback, R., Nygren, J., and Kubista, M., 1995, “Absorption and Fluorescence Properties of Fluorescein,” Spectrochim Acta A Mol Biomol Spectrosc, **51**(6), pp. L7–L21.

[33] Kumar Panigrahi, S., and Kumar Mishra, A., 2019, “Inner Filter Effect in Fluorescence Spectroscopy: As a Problem and as a Solution,” Journal of Photochemistry and Photobiology C: Photochemistry Reviews, **41**, p. 100318.

[34] AAT Bioquest, “Fluorescein, Disodium Salt *CAS 518-47-8*” [Online]. Available: https://www.aatbio.com/products/fluorescein-disodium-salt-cas-518-47-8. [Accessed: 14-Mar-2023].

[35] University of California Santa Barbara, “Table of Acids with Ka and PKa Values” [Online]. Available: https://clas.sa.ucsb.edu/staff/Resource%20Folder/Chem109ABC/Acid,%20Base%20Strength/Table%20of%20Acids%20w%20Kas%20and%20pKas.pdf. [Accessed: 14-Mar-2023].

[36] ThermoFisher Scientific, “Plastic Materials Selection” [Online]. Available: https://www.thermofisher.com/us/en/home/life-science/lab-plasticware-supplies/plastic-material-selection.html. [Accessed: 14-Mar-2023].

[37] Edward, J. T., 1970, “Molecular Volumes and the Stokes-Einstein Equation,” J Chem Educ, **47**(4), p. 261.

[38] Pitre, L., Plimmer, M. D., Sparasci, F., and Himbert, M. E., 2019, “Determinations of the Boltzmann Constant,” C R Phys, **20**(1), pp. 129–139.

[39] Berstad, D. A., Knapstad, B., Lamvik, M., Skjølsvik, P. A., Tørklep, K., and Øye, H. A., 1988, “Accurate Measurements of the Viscosity of Water in the Temperature Range 19.5–25.5°C,” Physica A: Statistical Mechanics and its Applications, **151**(2), pp. 246–280.

[40] Du Plessis, E., and Woudberg, S., 2009, “Modelling of Diffusion in Porous Structures,” *WIT Transactions on Engineering Sciences*, pp. 399–408.

[41] (2023)., N. C. for B. I., “PubChem Compound Summary for CID 10608, Fluorescein Sodium” [Online]. Available: https://pubchem.ncbi.nlm.nih.gov/compound/Fluorescein-sodium. [Accessed: 07-Feb-2023].

[42] Reddy, K. A., and Doraiswamy, L. K., 1961, *) Timmermans, "Physico-Chemical Constants of Binary Systems in Concentrated Solutions*, McGraw-Hill.

[43] Poirier D. R. and Geiger, G. H., 2016, “Fick’s Law and Diffusivity of Materials,” *Transport Phenomena in Materials Processing*, Springer International Publishing, Cham, pp. 419–461.

[44] Golshadi, M., 2016, *Carbon Nanotube Arrays for Intracellular Delivery and Biological Carbon Nanotube Arrays for Intracellular Delivery and Biological Applications Applications*.

Appendix A- Fluorescent Intensity Measurement

1. Turn on Computer and Fluorometer
    a. On the left side of fluorometer unit there is an on/off switch.
    b. The start button will turn green.
2. Start “SpectraManager” Software
3. User interface offers various tools to open and indicate connected devices.
    a. Select “Spectra Measurement”
4. A new window will open for the tuning of parameters and spectrum collection.
5. Set Parameters
    a. Set excitation wavelength depending on the chemical that is observed. Information on excitation spectra of various chemicals can be found online.
    b. Set emission boundaries to encompass full expected spectrum and exclude excitation wavelength range.
    c. Sensitivity on tool can be adjusted if fluorescent intensity is saturated or signal is too weak.
6. Take measurement of Empty Holder
    a. A baseline of holder without solution should be taken before every measurement to ensure trivial contamination of fluorescent dye.
    b. Some contamination may be acceptable depending on accuracy needed.
7. Pipette solution into the cuvette and insert the cuvette into the holder of the fluorometer.
    a. There is an arrow on the front of the cuvette indicating this side should face the user when inserted.
8. Press the Start Button to initiate the measurement.
    a. The spectra will begin to appear on the “Spectra Measurement” Window.
9. Name Spectrum and Save
    a. A “Spectra Analysis” window will appear with the new spectra.
    b. Data analysis can be conducted with this application.
    c. The data can be saved as a file specific to this program.
10. Take out the cuvette and displace solution.
    a. Pipette Solution into a vial for storage.
11. Export spectra as .csv or .txt
    a. These file types allow for use on programs like excel or MATLAB.
12. Repeat Until all Samples are run
13. Turn off Fluorometer and Computer

Appendix B- Calibration Curve Procedure

1. Personal protective equipment applied.
    a. Gloves
    b. Safety Glasses
2. Measuring Equipment Needed
    a. Digital Analytical Balance
    b. Powder Boat
    c. Powder Spoon
    d. 2 mL microtubes
    e. 100-1000 µL Pipette and Tip
    f. Jasco FP-8500 Spectrofluorometer
3. Target mass of powder dye calculated.
    a. $m_{powder} = \varphi_{target} * MW * V_{DI}$
        i. $m_{powder} = Mass\ of\ Powderized\ Fluorescent\ Particle$
        ii. $\varphi_{target} = Target\ Concentration\ of\ Solution$
        iii. $MW = Molecular\ Weight\ of\ Fluorescent\ Particle$
        iv. $V_{DI} = Volume\ of\ Deionized\ Water$
4. Use Balance to Measure the mass of the powder boat.
5. Add 3 mL of DI water to the vial.
6. With the Powder Spoon incrementally add small amounts of Powder
7. Once mass is within range of acceptable value add powder to vial.
8. Measure mass of the powder boat and residual fluorescent powder.
9. Add an additional 12 mL DI water to the vial.
10. Calculate Exact concentration of solution made.
    a. $\varphi_{Solution} = \frac{m_{actual}}{MW * V_{DI}}$
        i. $m_{actual} = m_{boat+powder} - m_{boat+residu}$
11. Calculate the concentrations to be used in dilution series.
    a. $\varphi_{Diluted} = D * \varphi_{Solution}$
    b. $D = Dilution\ Constant$ with values of 0.8, 0.5, 0.4, 0.2, 0.1, 0.08, 0.05, 0.04, 0.02, 0.01, 0.008, 0.005, 0.004, 0.002.
12. Calculate amount of fluorescent solution and DI water needed for each 2 mL microtube.
    a. $V_{Dye} = \frac{\varphi_{Diluted}}{\varphi_{Solution}} * V_{New}$
        i. $V_{Dye} = Volume\ of\ Dye\ Solution\ to\ add$
        ii. $V_{New} = Volume\ of\ New\ Solution\ in\ microtube$
    b. $V_{DI} = V_{New} - V_{Dye}$
        i. $V_{DI} = Volume\ of\ DI\ Water\ to\ Add$
13. Use Procedure for Fluorometer usage found in Appendix A.

Appendix C- Preliminary Work with Optical Table

Two fluorescent spectroscopy tools were used during this study. The first spectrofluorometer was provided by the lab of Dr. Ke Du. This fluorometer is set up to beam a laser at a specified wavelength of 488 nm. The data acquisition system records changes in the reflected light that is collected by the system of mirrors. A 3D printed device interfaced with the support beams shown in Figure E1. This device included glass port holes through which the 488 nm laser interacted with the solution. This tool allowed for the continuous measurement of concentration without the need for sampling. By altering the position of the device on the support beams, solutions in both reservoirs could be monitored easily.

This spectroscopy tool was only used for initial experimentation and proof of concept experiments. Access to this tool was prohibited, creating the need for an alternative method of monitoring concentration. In addition to change in access, this tool was limited by a set wavelength of 488 nm meaning only specific molecules could be chosen. The open format of the optical table created a need for a procedure to limit contamination of ambient light. The cost to reproduce this tool for continued use proved unfeasible.

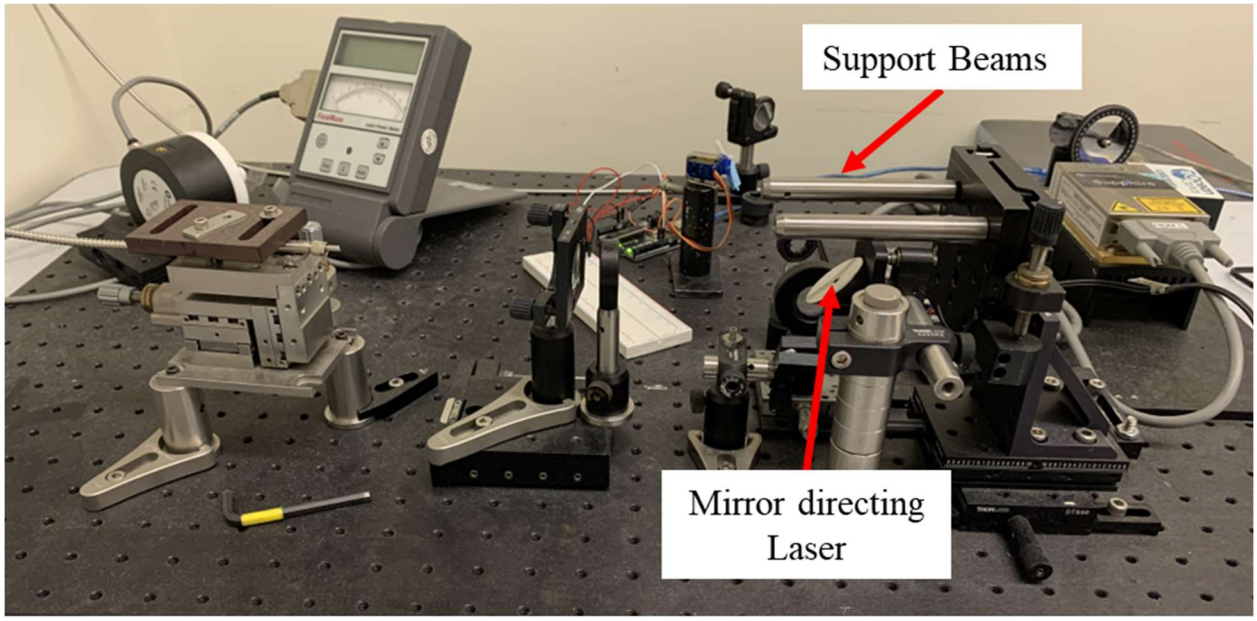

Figure E1: Spectrofluorometer in Dr. Ke Du's lab. The proposed device will rest on the support beams. The laser points vertically when it hits the indicated mirror.

The shape of the design was inspired by the need for easily switching the fluorometer laser between reservoirs. A hole through the bottom of the reservoir provides a place for a translucent coverslip that the laser can pass through. Figure E2 depicts the interaction between the solutions in the reservoirs and the optical table fluorescent spectrometer.

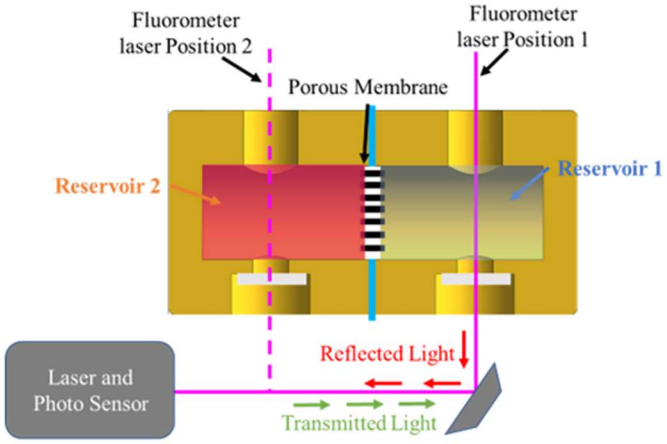

Figure E2: Method of collecting measurements of fluorescent intensity using the optical table fluorescent spectroscopy device.

Appendix D- Reservoir Design Process

The first devices designed are shown in Figure D1. These reservoirs were used in tandem with the fluorescent spectroscopy device. The system is composed of two reservoirs each with a volume of 5 mL. The system is separated by the vinyl sheets enclosing the CNT array. A hole in the bottom of each reservoir is closed using a glass cover slip. This coverslip allows for the interaction of the spectroscopy laser with the solution for measurement of fluorescent intensity. This reservoir system was clamped together using a C-clamp with a width of three inches.

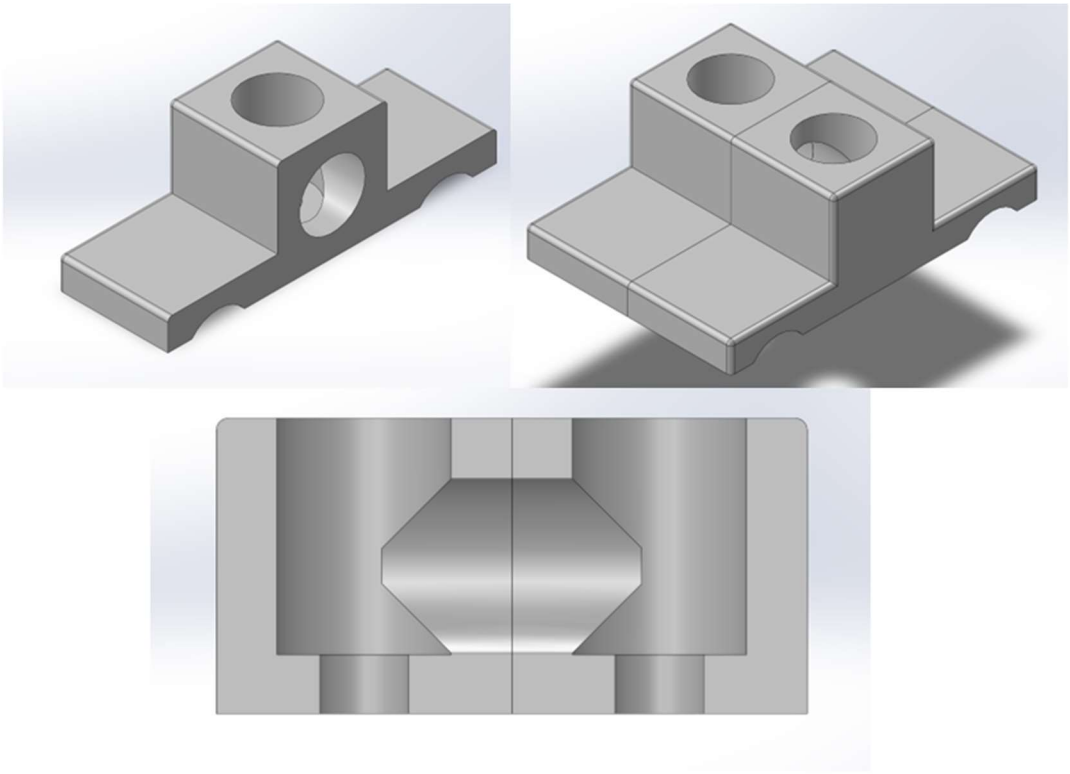

Figure D1: A.) Version 1 of the reservoirs used to measure diffusion. This reservoir is meant to interface with the support beams of the optical table fluorescent spectroscopy machine. **B.)** Two reservoirs are clamped together once they are separate by a vinyl cover slip with a CNT array. One reservoir will have a higher fluorescent molecule concentration to stimulate diffusion. **C.)** The cross section shows the middle point where the CNT array is placed. A hole through the bottom provides access for the laser of the optical table to excite the fluorescent molecule. The total volume of the two-reservoir system is 10 mL.

The rough surface of the 3D printed parts created challenges for gluing glass coverslips and sealing contact paper. However, the chief concern proved to be evidence of micro cracks.

These micro cracks were linked to the crudeness of the clamping mechanism that held the two reservoirs together.

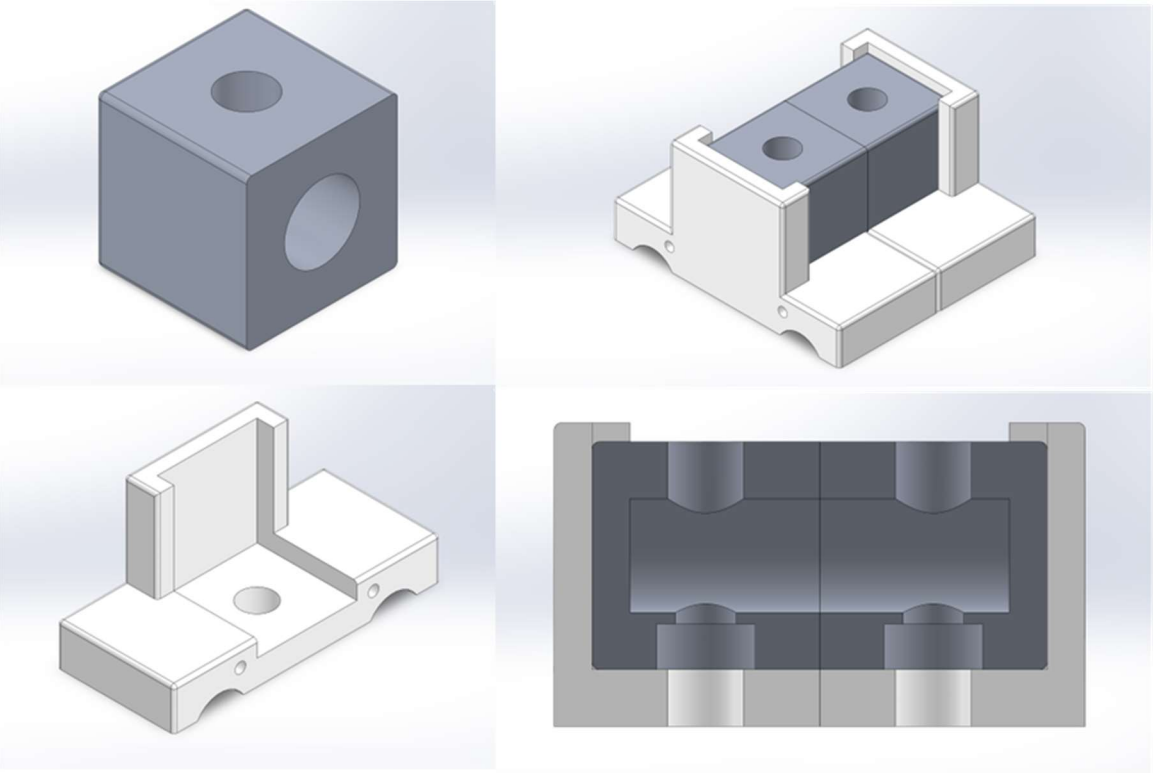

Figure D2: A.) Version 2 of the reservoirs used to measure diffusion. The reservoir was separated from the clamping mechanism to make the machining process easier. **B.)** The full assembly shows the interaction between the clamping apparatus and the aluminum reservoirs. These two reservoirs are separated by a vinyl cover slip with a CNT array. **C.)** The clamping apparatus was 3D printed and uses bolts to clamp the reservoirs together. **D.)** The cross section shows the middle point where the CNT array is placed. A hole through the bottom provides access for the laser of the optical table to excite the fluorescent molecule. The total volume of the two-reservoir system is 10 mL.

To overcome the rough surface, a mixture of additive manufacturing and aluminum machining allowed for both complex shapes and smooth finishes. The reservoirs are cubes of aluminum with holes machined for the solution and glass coverslip interface. The base of the device is 3D printed to retain the supports for the beams shown in Figure D1. The clamping mechanism is replaced with bolts and nuts that can press on the contact paper while being incorporated into the design. Figure D2 shows version 2 of the reservoir system. This system retained the ability to interface with the fluorescent spectroscopy device. A glass coverslip allows

the laser of 488 nm to pass through the solution and measure the fluorescent intensity of the reservoir without sampling.

Due to the switch from an optical table fluorescent spectroscopy device to the Jasco FP-8500 fluorescent spectroscopy device, the reservoirs were redesigned to better fit the revised procedure. Version three of the reservoir system is shown in Figure D3. This system integrates the clamping apparatus with the reservoirs. The system is manufactured out of aluminum to ensure low surface roughness.

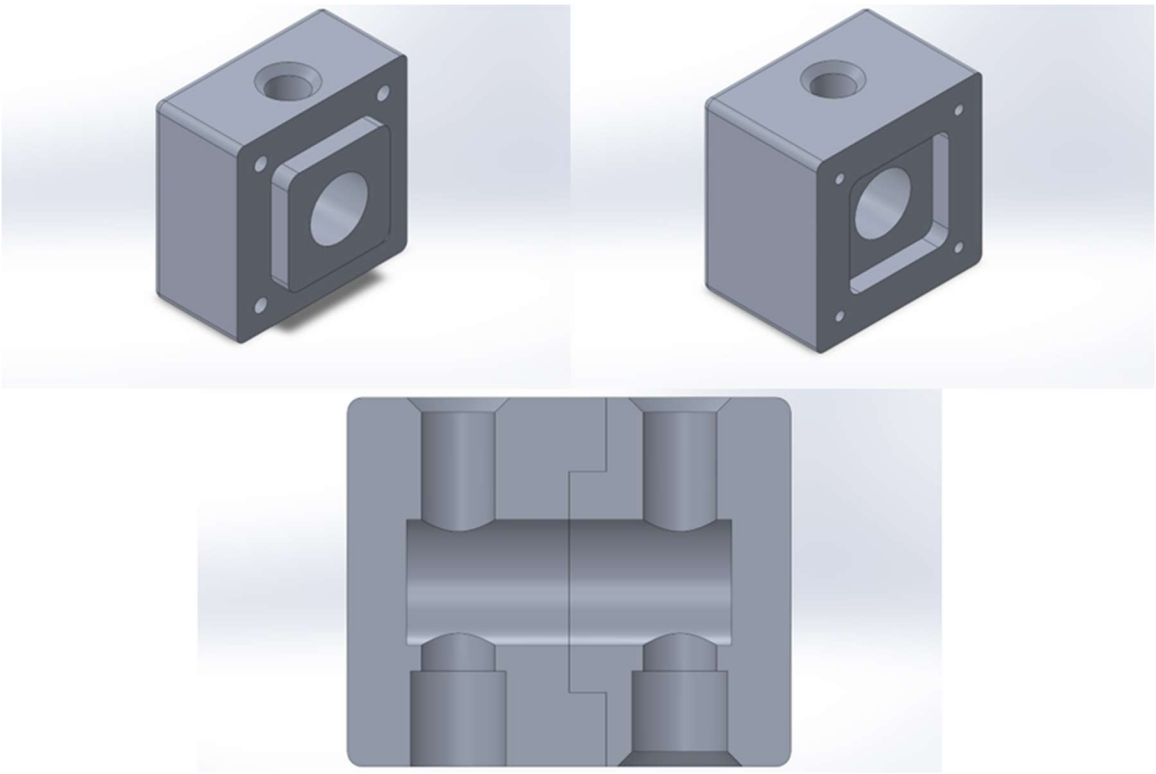

Figure D3: A.) Version 3 of the reservoirs used to measure diffusion. The two reservoirs are interlocking pieces preventing twisting from occurring. **B.)** The second interlocking piece has threaded holes to use bolts as a clamping apparatus. **C.)** The cross section shows that a hole for the glass cover slip allows the laser from a spectroluorometer to interreact with the solution. The total volume of this reservoir is 10 mL.

The aluminum material used was seen to interact with the solution and increase the pH of the system. As pH increased, the fluorescent intensity could not be correlated to concentration of the solution without knowing the pH of the system. Creating smaller reservoir volumes sped up diffusion creating a higher throughput of experiments.

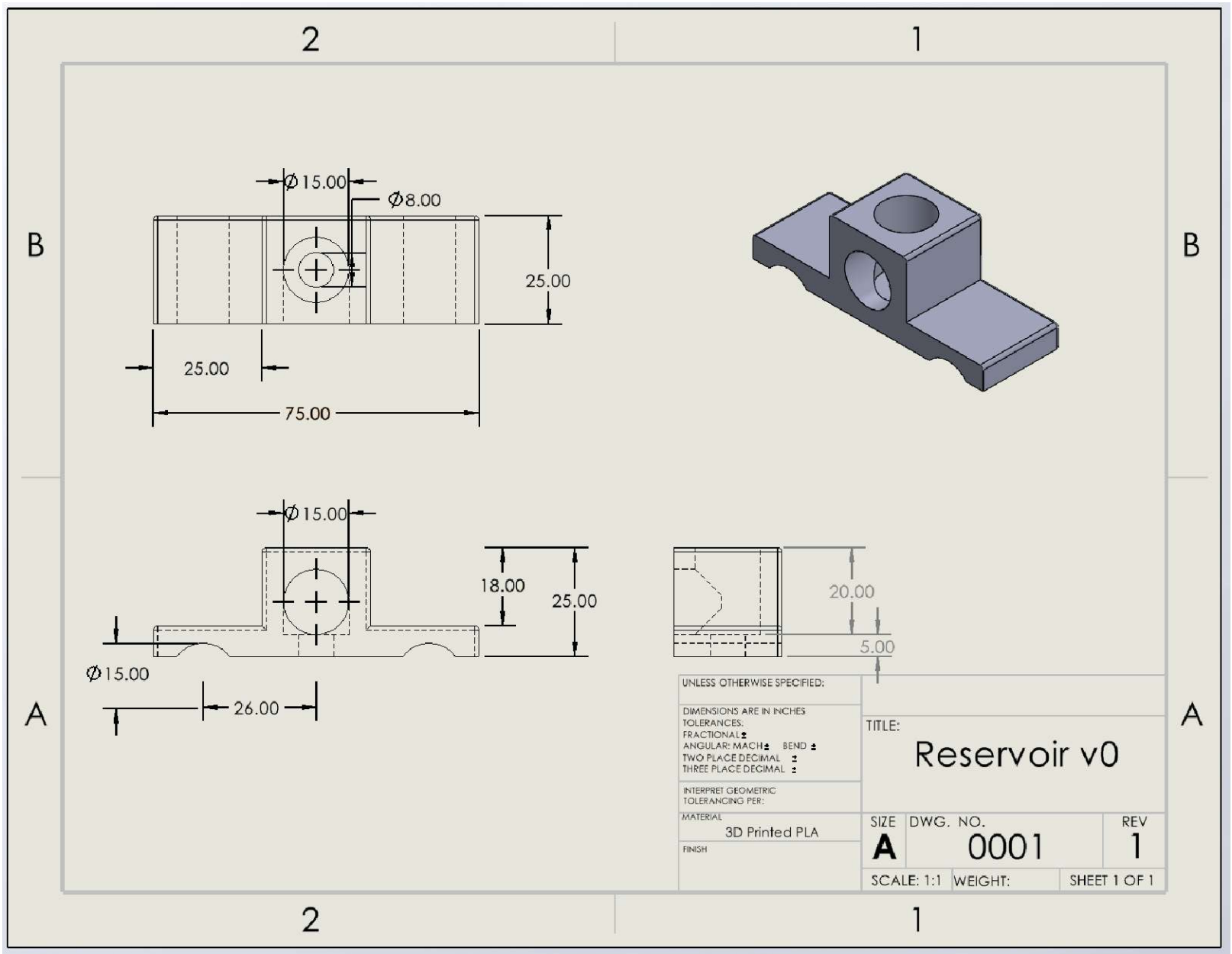
2
1
B
A
Ø15.00
Ø8.00
25.00
25.00
75.00
Ø15.00
18.00
25.00
Ø15.00
26.00
20.00
5.00
UNLESS OTHERWISE SPECIFIED:
DIMENSIONS ARE IN INCHES
TOLERANCES:
FRACTIONAL ±
ANGULAR: MACH ± BEND ±
TWO PLACE DECIMAL ±
THREE PLACE DECIMAL ±
INTERPRET GEOMETRIC TOLERANCING PER:
MATERIAL
3D Printed PLA
FINISH
TITLE:
Reservoir v0
SIZE
A
DWG. NO.
0001
REV
1
SCALE: 1:1
WEIGHT:
SHEET 1 OF 1

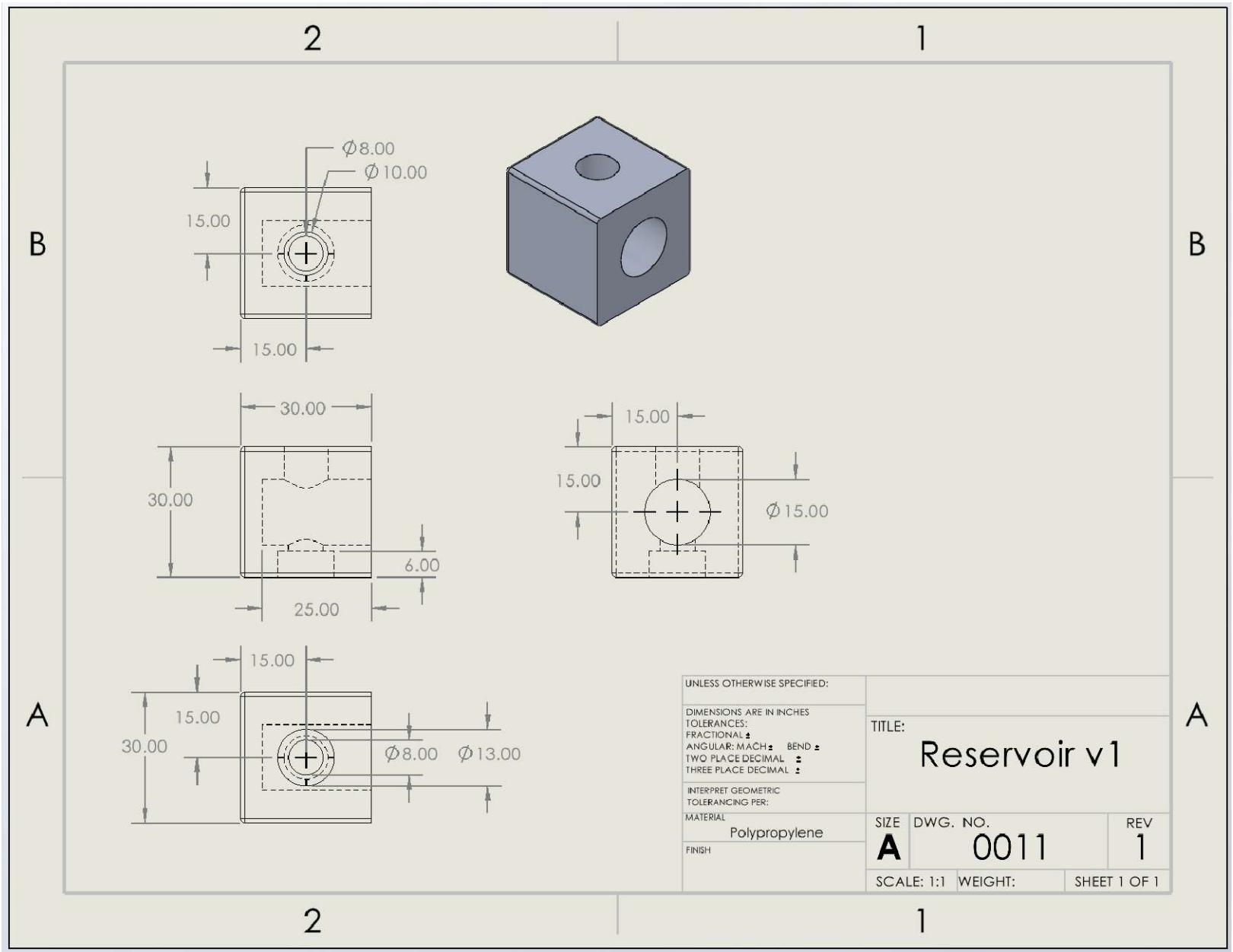
2
1
B
A
Ø8.00
Ø10.00
15.00
15.00
30.00
30.00
6.00
25.00
15.00
15.00
Ø15.00
15.00
15.00
30.00
Ø8.00
Ø13.00
UNLESS OTHERWISE SPECIFIED:
DIMENSIONS ARE IN INCHES
TOLERANCES:
FRACTIONAL ±
ANGULAR: MACH ± BEND ±
TWO PLACE DECIMAL ±
THREE PLACE DECIMAL ±
INTERPRET GEOMETRIC TOLERANCING PER:
MATERIAL
Polypropylene
FINISH
TITLE:
Reservoir v1
SIZE
A
DWG. NO.
0011
REV
1
SCALE: 1:1
WEIGHT:
SHEET 1 OF 1

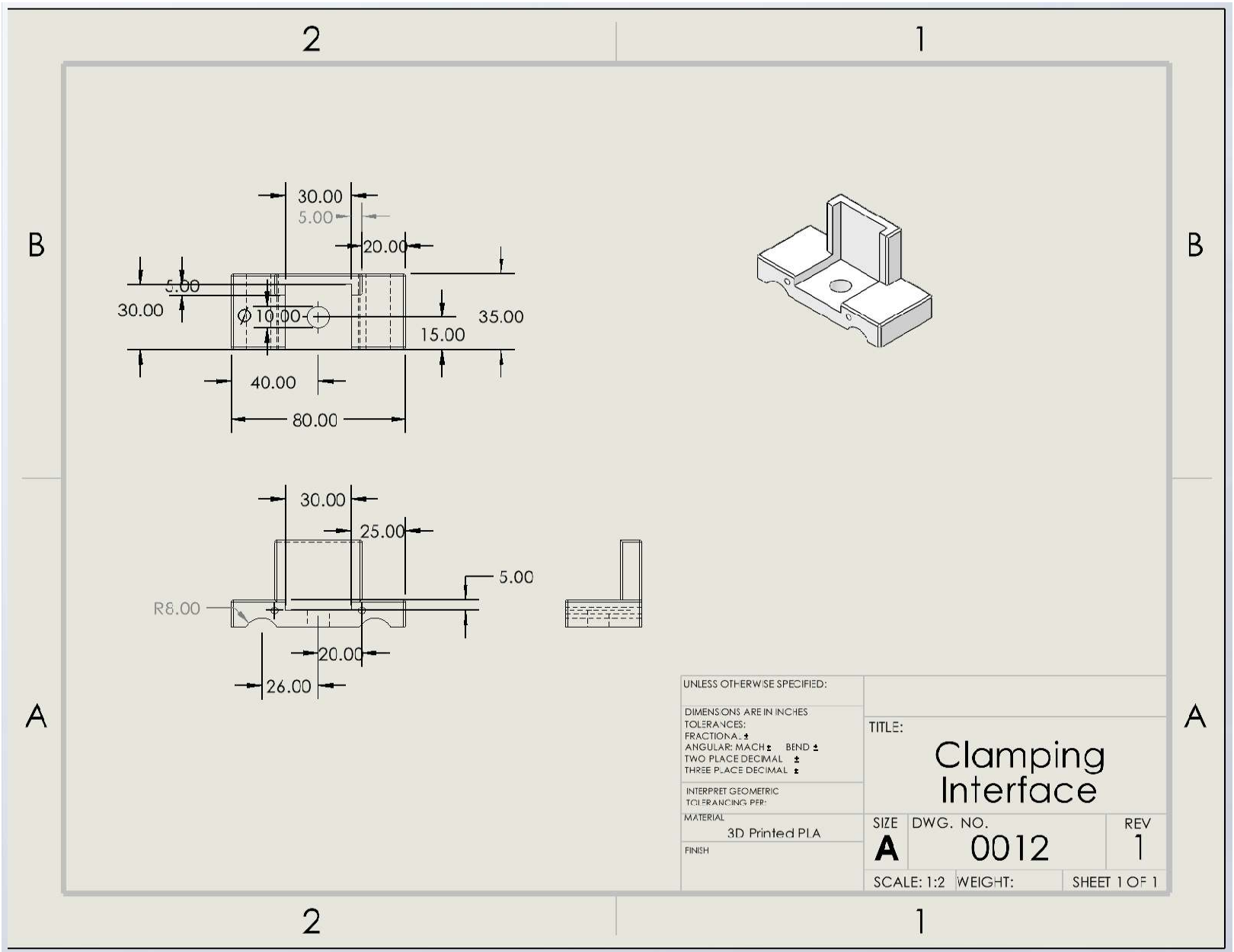
2
1
B
A
30.00
5.00
20.00
5.00
30.00
Ø10.00
35.00
15.00
40.00
80.00
30.00
25.00
5.00
R8.00
20.00
26.00
UNLESS OTHERWISE SPECIFIED:
DIMENSIONS ARE IN INCHES
TOLERANCES:
FRACTIONAL ±
ANGULAR: MACH ± BEND ±
TWO PLACE DECIMAL ±
THREE PLACE DECIMAL ±
INTERPRET GEOMETRIC TOLERANCING PER:
MATERIAL
3D Printed PLA
FINISH
TITLE:
Clamping Interface
SIZE
A
DWG. NO.
0012
REV
1
SCALE: 1:2
WEIGHT:
SHEET 1 OF 1

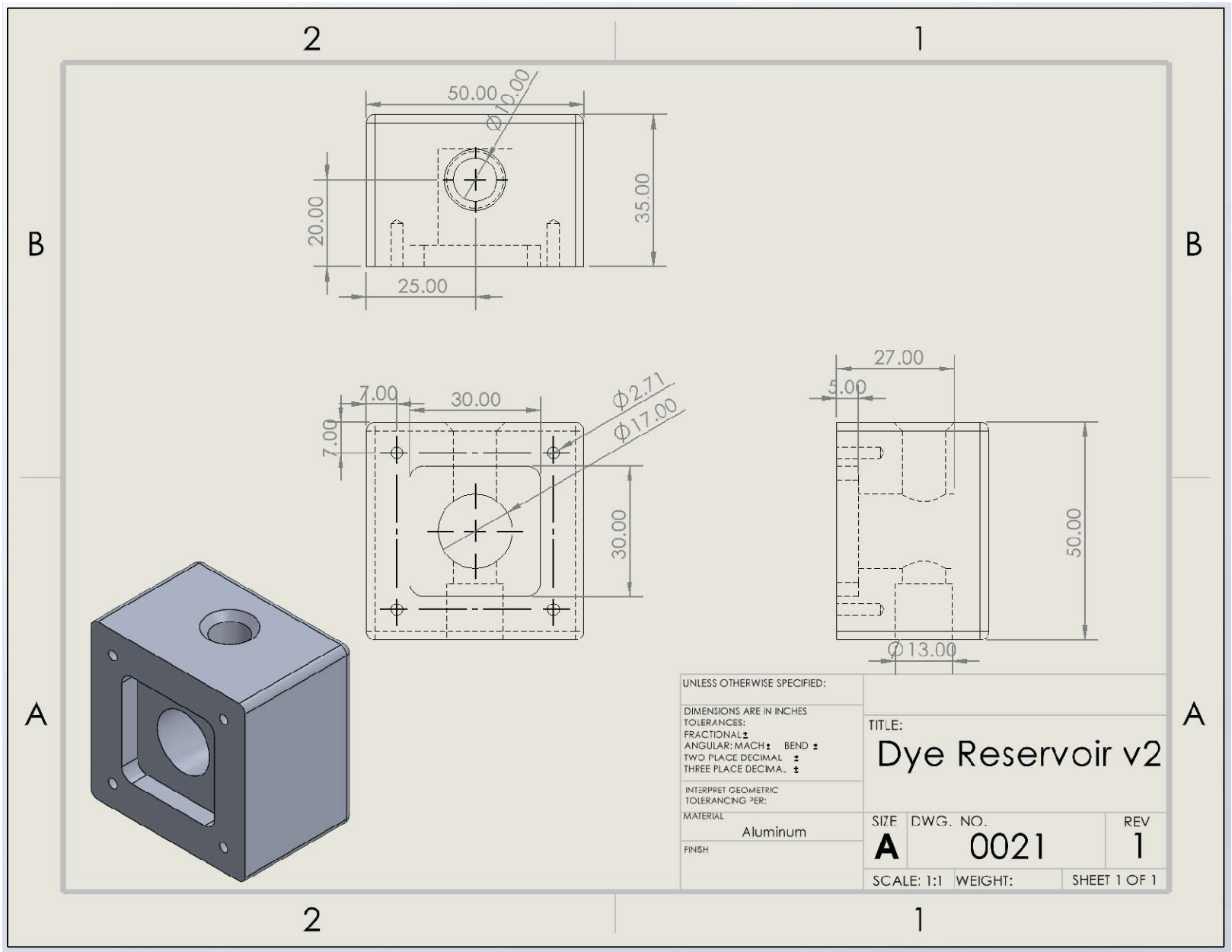
2
1
B
A
50.00
Ø10.00
20.00
35.00
25.00
7.00
30.00
Ø2.71
Ø17.00
7.00
30.00
27.00
5.00
50.00
Ø13.00
UNLESS OTHERWISE SPECIFIED:
DIMENSIONS ARE IN INCHES
TOLERANCES:
FRACTIONAL ±
ANGULAR: MACH ± BEND ±
TWO PLACE DECIMAL ±
THREE PLACE DECIMA ±
INTERPRET GEOMETRIC TOLERANCING PER:
MATERIAL
Aluminum
FINISH
TITLE:
Dye Reservoir v2
SIZE
A
DWG. NO.
0021
REV
1
SCALE: 1:1
WEIGHT:
SHEET 1 OF 1

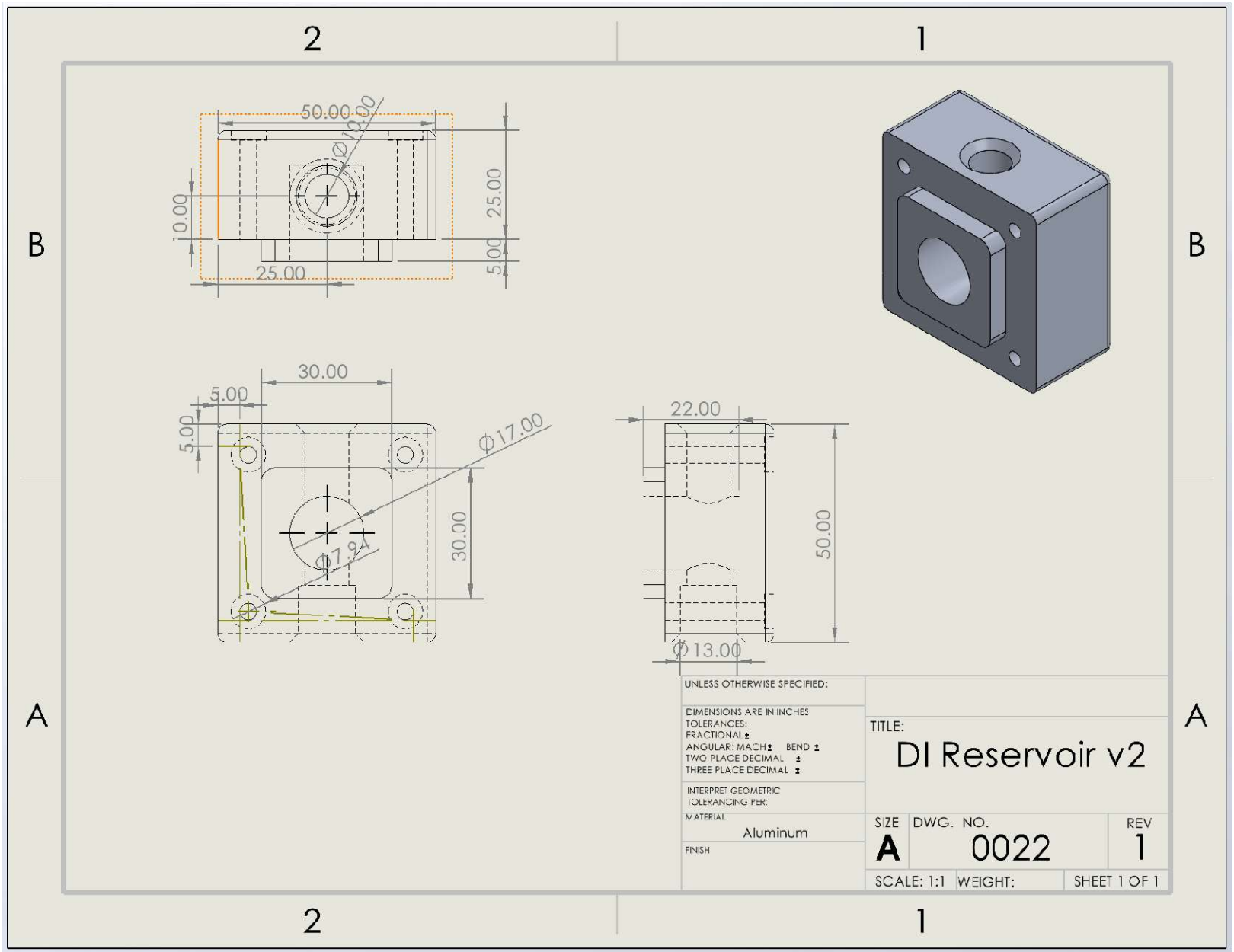
2
1
B
A
50.00
Ø12.00
10.00
25.00
5.00
25.00
30.00
5.00
5.00
Ø17.00
30.00
Ø7.94
22.00
50.00
Ø13.00
UNLESS OTHERWISE SPECIFIED:
DIMENSIONS ARE IN INCHES
TOLERANCES:
FRACTIONAL ±
ANGULAR: MACH ± BEND ±
TWO PLACE DECIMAL ±
THREE PLACE DECIMAL ±
INTERPRET GEOMETRIC TOLERANCING PER:
MATERIAL
Aluminum
FINISH
TITLE:
DI Reservoir v2
SIZE
A
DWG. NO.
0022
REV
1
SCALE: 1:1
WEIGHT:
SHEET 1 OF 1

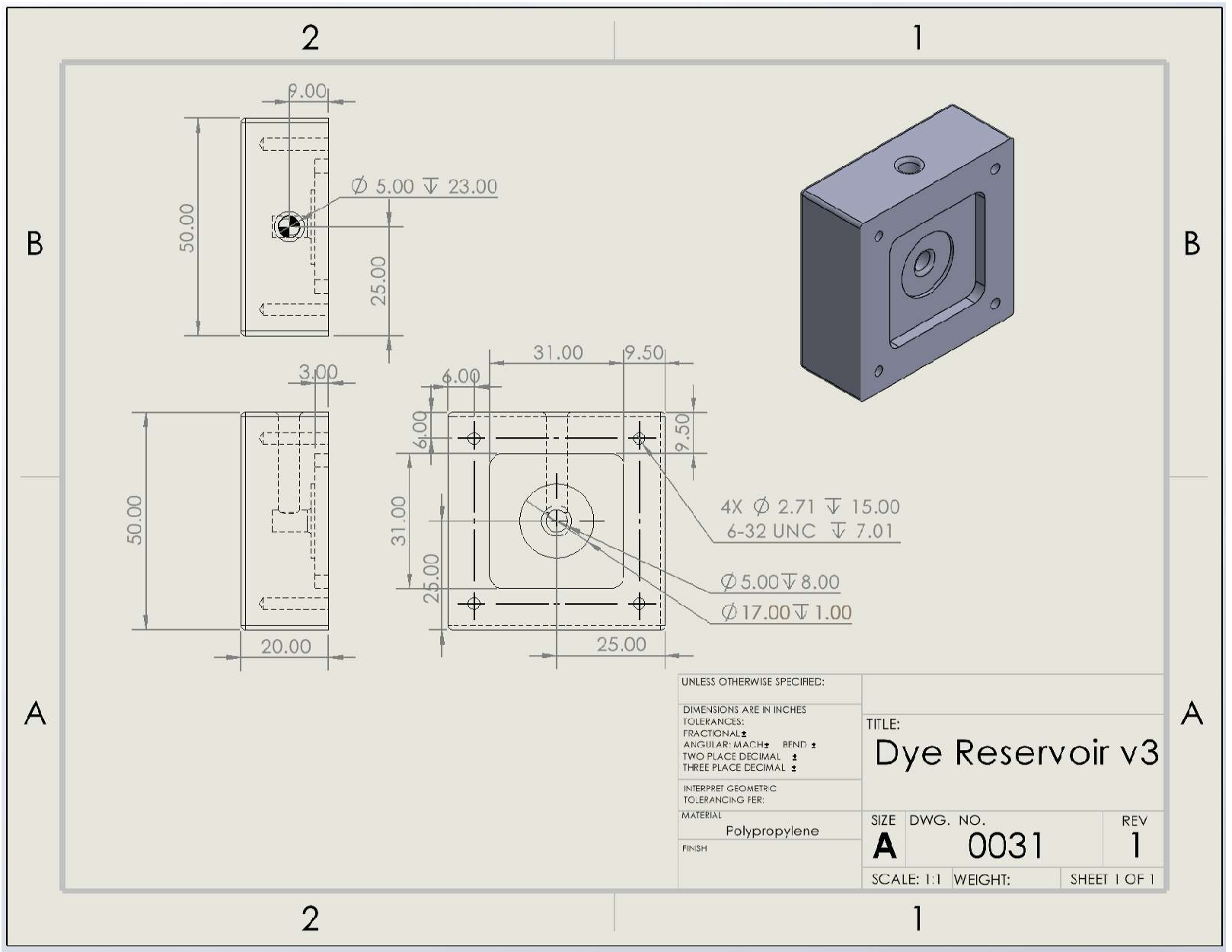
2
1
B
A
9.00
50.00
Ø 5.00 ↧ 23.00
25.00
3.00
50.00
20.00
31.00
9.50
6.00
6.00
9.50
31.00
25.00
4X Ø 2.71 ↧ 15.00
6-32 UNC ↧ 7.01
Ø 5.00 ↧ 8.00
Ø 17.00 ↧ 1.00
25.00
UNLESS OTHERWISE SPECIFIED:
DIMENSIONS ARE IN INCHES
TOLERANCES:
FRACTIONAL ±
ANGULAR: MACH ± BEND ±
TWO PLACE DECIMAL ±
THREE PLACE DECIMAL ±
INTERPRET GEOMETRIC TOLERANCING PER:
MATERIAL
Polypropylene
FINISH
TITLE:
Dye Reservoir v3
SIZE
A
DWG. NO.
0031
REV
1
SCALE: 1:1
WEIGHT:
SHEET 1 OF 1

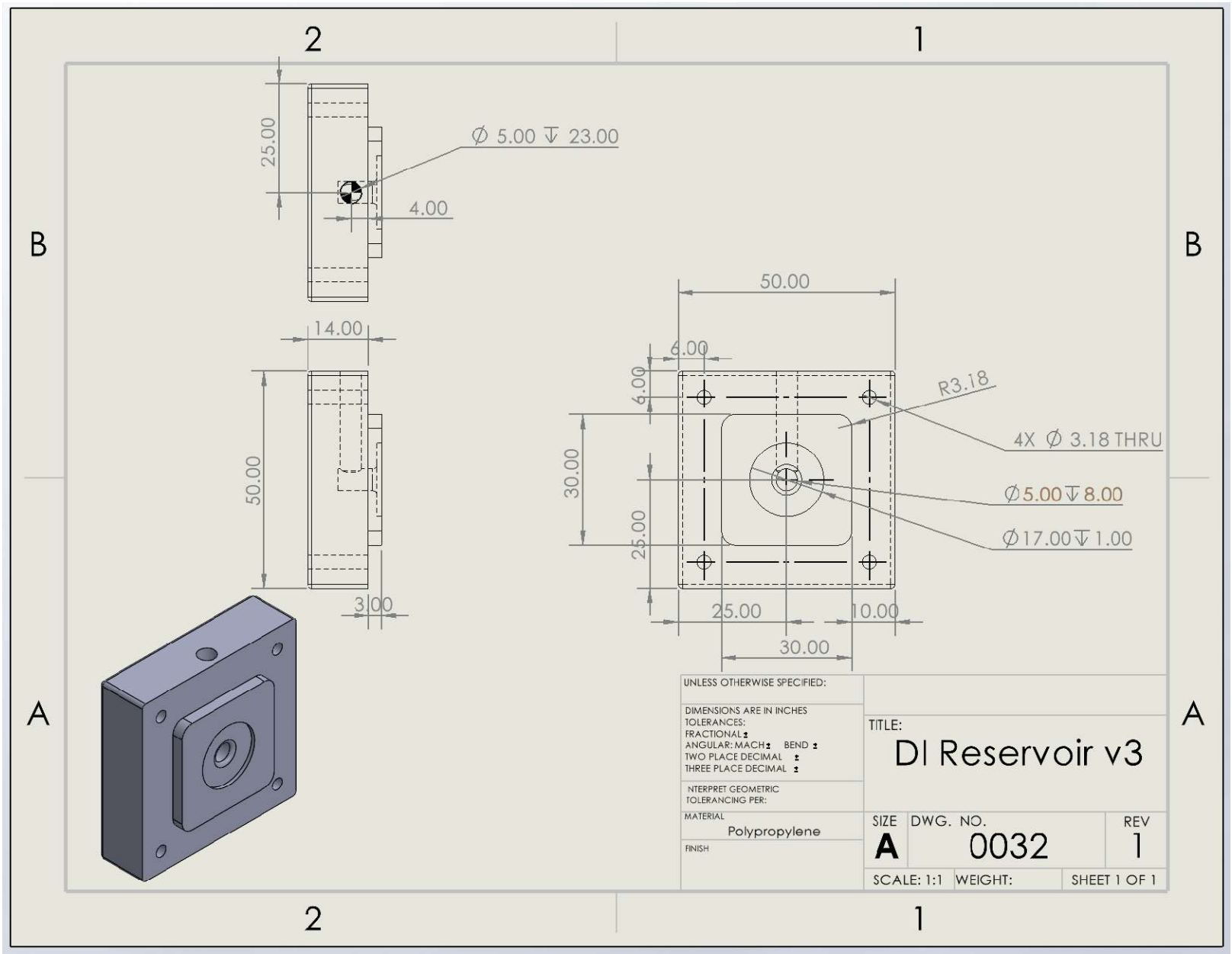
2
1
B
A
25.00
Ø 5.00 ↧ 23.00
4.00
14.00
50.00
3.00
50.00
6.00
6.00
R3.18
4X Ø 3.18 THRU
30.00
Ø5.00↧8.00
25.00
Ø17.00↧1.00
25.00
10.00
30.00
UNLESS OTHERWISE SPECIFIED:
DIMENSIONS ARE IN INCHES
TOLERANCES:
FRACTIONAL ±
ANGULAR: MACH ± BEND ±
TWO PLACE DECIMAL ±
THREE PLACE DECIMAL ±
NTERPRET GEOMETRIC
TOLERANCING PER:
MATERIAL
Polypropylene
FINISH
TITLE:
DI Reservoir v3
SIZE
A
DWG. NO.
0032
REV
1
SCALE: 1:1
WEIGHT:
SHEET 1 OF 1

Appendix E- MATLAB Script

```
clc
clear
close all

%% Data Processing

%Read in Spectra from Samples Collected
%File correspond to Reservoir #, Sample #, and Experiment Respectively
%DI Reservoir is Read First
A1 = readmatrix("5B_01.csv","Range","A20:B210");
B1 = readmatrix("5B_02.csv","Range","A20:B210");
D1 = readmatrix("7B_02.csv","Range","A20:B210");
F1 = readmatrix("7C_02.csv","Range","A20:B210");
G1 = readmatrix("5B_03.csv","Range","A20:B210");
H1 = readmatrix("5C_03.csv","Range","A20:B210");
I1 = readmatrix("7B_03.csv","Range","A20:B210");
J1 = readmatrix("7C_03.csv","Range","A20:B210");
K1 = readmatrix("7C_03.csv","Range","A20:B210");

%Dye Reservoir Read in Second
A2 = readmatrix("6B_01.csv","Range","A20:B210");
B2 = readmatrix("6B_02.csv","Range","A20:B210");
D2 = readmatrix("8B_02.csv","Range","A20:B210");
F2 = readmatrix("8C_02.csv","Range","A20:B210");
G2 = readmatrix("6B_03.csv","Range","A20:B210");
H2 = readmatrix("6C_03.csv","Range","A20:B210");
I2 = readmatrix("8B_03.csv","Range","A20:B210");
J2 = readmatrix("8C_03.csv","Range","A20:B210");
K2 = readmatrix("6D_03.csv","Range","A20:B210");

%Time in Hours is recorded manually
x1=[48 48 24 48 48 72 96 120 96];

%Maximum of each spectra is found and adjusted using the calibration curve
y1=1.43*.003*1000/1500*[max(A2(:,2)) max(B2(:,2))
    max(D2(:,2)) max(F2(:,2))
    max(G2(:,2)) max(H2(:,2)) max(I2(:,2))/1100*1500
    max(J2(:,2)) max(K2(:,2))];

y2=1.43*.003*1000/1500*[ max(A1(:,2)) max(B1(:,2))
    max(D1(:,2)) max(F1(:,2))
    max(G1(:,2)) max(H1(:,2)) max(I1(:,2))/1100*1500
    max(J1(:,2)) max(K1(:,2))];

%% Fitting of Experimental Effective Diffusivity

%Input Data to be fitted
A = [x1' y2'];
B = [x1' y1'];

%Initialize constants of the system
phi_start=1.43*.003*1000; %Starting Concentration
L=0.00006; %Length of CNT
r_pore=70*10^(-9); %Radius of CNT
r_active=.004; %Radius of open Array area
ro_pore=11.8*10^12; %Density of CNTs in AAO
area=pi()*r_pore^2*ro_pore*pi()*(r_active)^2; %Pore Area
V=0.000002; %Reservoir Volume
```

```
%Create Arrays for R squared calculation
f=10^(-12):.01*10^(-12):5*10^(-10); %all diffusivities to test
R_square_A=NaN(length(f),1); %R squared values
Y_A=NaN(length(A),1); %concentrations at different time points

R_square_B=NaN(length(f),1); %R squared values
Y_B=NaN(length(A),1); %concentrations at different time points

y_bar_A=mean(A(:,2)); %mean of data values for R squared calculation
y_bar_B=mean(B(:,2)); %mean of data values for R squared calculation

residual_A=0;
residual_mean_A=0;
residual_B=0;
residual_mean_B=0;

%For loop through all diffusivities
for j=1:1:length(f)

    %For loop through all data points
    for k=1:1:length(A)

        %Calculate time constant for given diffusivity
        tau=L*V/(2*area*f(j));
        tau_B=L*V/(2*area*f(j));
        %Calculate concentration at given time
        Y_A(k,1)=phi_start/2*(1-exp(-A(k,1)*60*60/tau));
        Y_B(k,1)=phi_start/2*(1+exp(-B(k,1)*60*60/tau_B));

        %Residuals for R squared
        residual_A=residual_A+(A(k,2)-Y_A(k,1))^2;
        residual_mean_A=residual_mean_A+(A(k,2)-y_bar_A)^2;

        residual_B=residual_B+(B(k,2)-Y_B(k,1))^2;
        residual_mean_B=residual_mean_B+(B(k,2)-y_bar_B)^2;
    end

    %R_sqaure Calculation
    R_square_A(j,1)=1-residual_A/residual_mean_A;
    residual_A=0;
    residual_mean_A=0;

    R_square_B(j,1)=1-residual_B/residual_mean_B;
    residual_B=0;
    residual_mean_B=0;
end

%Identify Diffusivity of best fit
[R_A,I_A]=max(R_square_A);
D_best_A=f(I_A);

[R_B,I_B]=max(R_square_B);
D_best_B=f(I_B);

%% Simulate the Analytical and experimental Model

%Calculate the effective diffusivity with porosity factor
D=2.85*10^(-10);
porosity=pi()*r_pore^2*ro_pore;
D_eff=D*porosity;
```

```
%Create time constants from each effective diffusivity
tau=L*V/(2*area*D_eff);
tau2=L*V/(2*area*D_best_A);
tau3=L*V/(2*area*D_best_B);

%Initialize arrays
t=0:1:120;

phi_0=NaN(1,length(t));
phi_l=NaN(1,length(t));
phi_0_fit=NaN(1,length(t));
phi_l_fit=NaN(1,length(t));
i=1;

%Use Ficks laws to estimate concentrations in each reservoir vs. time
for t=0:1:120

    phi_0(i)=phi_start/2*(1+exp(-t*60*60/tau));
    phi_l(i)=phi_start/2*(1-exp(-t*60*60/tau));
    phi_0_fit(i)=phi_start/2*(1+exp(-t*60*60/tau3));
    phi_l_fit(i)=phi_start/2*(1-exp(-t*60*60/tau2));

    i=i+1;
end

t=0:1:120;

%% Plotting

%Plot Raw Data
figure(1)
hold on
plot(x1,y1,'*r',x1,y2,'ob')
xlabel('Time [hours]')
ylabel('Concentration [uM]')
title('Time of Diffusion vs Fluorescent Intensity')
legend('Dye Reservoir','DI Water Reservoir')
xlim([0 120])
hold off

%Show R squared calculations
figure(2)
hold on
plot(f',R_square_A(:,1),f',R_square_B(:,1))
xlabel('Diffusivity')
ylabel('R Squared')
hold off

%Plot All spectra for data
figure(3)
hold on
plot(A1(:,1),A1(:,2),B1(:,1),B1(:,2),C1(:,1),C1(:,2),D1(:,1),D1(:,2))
xlabel('Wavelength [nm]')
ylabel('Fluorescent Intensity [-]')
title('Changing Spectra in Reservoir 1')
legend( 'Experiment 1 Sample 1','Experiment 1 Sample 2',...
    'Experiment 2 Sample 1', 'Experiment 2 Sample 2')
hold off

figure(4)
```

```
hold on
plot(A2(:,1),A2(:,2),B2(:,1),B2(:,2),C2(:,1),C2(:,2),D2(:,1),D2(:,2))
xlabel('Wavelength [nm]')
ylabel('Fluorescent Intensity [-]')
title('Changing Spectra in Reservoir 2')
legend('Experiment 1 Sample 1','Experiment 1 Sample 2',...
    'Experiment 2 Sample 1', 'Experiment 2 Sample 2')
hold off

%Plot Experimantal vs. analytical
figure(5)
hold on
plot(t,phi_0,'r-',t,phi_l,'b-',t,phi_0_fit,'r--',t,phi_l_fit,'b--','LineWidth',1.5)
plot(x1,y1,'*r',x1,y2,'ob','LineWidth',1.0)
xlabel('Time [hours]')
ylabel('Concentration [uM]')
legend('Analytical x=0','Analytical x=L', 'Experimental x=0', 'Experimental x=L',...
    'Sampled Data x=0', 'Sampled Data x=L','Location','southoutside','NumColumns',3)
hold off
```

Appendix F- Experimental Data

Table F1: Data collected for 5 mL reservoir with concentration gradient of 10.01 µM.

Experiment	Time [hr]	Dye Reservoir [-]	DI Reservoir [-]
7	0	2311.38	0
	24	2317.27	82.9955
	48	1901.98	276.98
	120	1014.82	427.487
9	0	2746.82	0
	24	2873.12	23.4877
	48	2860.05	98.6985
	72	2663.52	217.241
	96	2536.08	298.897
10	0	2803.77	0
	24	3729.27	23.8933
	48	2828.37	89.706
	72	2951.41	188.753
	96	2301.77	337.707
12	0	3692.94	0
	24	3564.25	173.64
	48	3284.24	368.25
	72	2068.88	859.061
	96	803.027	429.458
13	0	2352.09	0
	24	3487.12	276.695
	72	3040.95	125.334
	102	3187.9	640.832
14	0	3074.04	0
	24	2704.21	97.5868
	72	1661.74	307.329
	102	966.197	413.499

Table F2: Averaged data from table E1 with standard error bars displayed on Figure 20 and 21.

Time	Dye Reservoir		DI Reservoir	
	Averaged Data	Standard Error	Averaged Data	Standard Error
[hr]	[-]	[-]	[-]	[-]
0	2771.094286	0	186.1762097	0
24	3021.828571	192.8676143	214.1882433	86.62194888
48	2676.212	277.7061	229.6639969	87.29854643
72	2561.27	421.685	259.8436049	218.8425732
96	2068.7134	299.745	386.3664281	49.36801034
102	2077.0485	527.1655	1110.8515	113.6665
120	1732.87	471.5303333	359.6728803	22.12002328

Table F3: Data collected for 5 mL reservoir with concentration gradient of 7.60 and 100.1 µM displayed on Figure 22 and 23.

5 mL Reservoir at 7.6 µM			5 mL Reservoir at 100.1 µM		
Time [hr]	Dye Reservoir [-]	DI Reservoir [-]	Time [hr]	Dye Reservoir [-]	DI Reservoir [-]
0	2416.62	0	0	1483.21	0
1	2693.11	7.74895	24	1341.7	116.175
3	2900.78	13.3357	48	1264.13	205.314
8	2246.41	84.2988	72	1041.4	340.303
24	2477.56	671.775			
48	2506.42	554.896			

Table F4: Data collected for 0.4 mL reservoir with concentration gradient of 4.29 and 10.01 µM displayed on Figure 27 and 28.

0.4 mL Reservoir at 4.29 µM			0.4 mL Reservoir at 10.01 µM		
Time [hr]	Dye Reservoir [-]	DI Reservoir [-]	Time [hr]	Dye Reservoir [-]	DI Reservoir [-]
48	1184.32	12.1965	24	3460.75	401.401
48	1319.09	333.73	72	3471.49	616.421
72	1595.78	50.8818	24	3472.49	411.391
48	1476.78	42.5809	72	3503.12	820.224
24	1714.9	11.5641			
72	682.447	16.7104			

Table F5: Data collected for 2 mL reservoir with concentration gradient of 4.29 and 10.01 µM displayed on Figure 25 and 26.

2 mL Reservoir at 4.29 µM			2 mL Reservoir at 10.01 µM		
Time [hr]	Dye Reservoir [-]	DI Reservoir [-]	Time [hr]	Dye Reservoir [-]	DI Reservoir [-]
48	1151.58	244.344	24	2192.01	315.965
48	989.229	382.655	48	1657.56	542.138
24	1289.52	384.995	72	1414.78	604.725
48	892.47	506.022	96	1606.18	1123.19
48	928.055	285.6	24	2034.61	327.243
72	1063.36	476.761	48	1671.44	641.248
96	616.99	432.503			
120	806.924	685.745			
96	986.155	685.745			